

NEW MATERIALS SYSTEMS FOR AQUEOUS BATTERIES

A DISSERTATION

SUBMITTED TO

THE DEPARTMENT OF MATERIALS SCIENCE AND ENGINEERING

AND THE COMMITTEE ON GRADUATE STUDIES

OF STANFORD UNIVERSITY

IN PARTIAL FULFILLMENT OF THE REQUIREMENTS

FOR THE DEGREE OF

DOCTOR OF PHILOSOPHY

Colin Deane Wessells

May 2012

© 2012 by Colin Deane Wessells. All Rights Reserved.
Re-distributed by Stanford University under license with the author.

This dissertation is online at: <http://purl.stanford.edu/jb154ng2653>

I certify that I have read this dissertation and that, in my opinion, it is fully adequate in scope and quality as a dissertation for the degree of Doctor of Philosophy.

Yi Cui, Primary Adviser

I certify that I have read this dissertation and that, in my opinion, it is fully adequate in scope and quality as a dissertation for the degree of Doctor of Philosophy.

Jennifer Dionne

I certify that I have read this dissertation and that, in my opinion, it is fully adequate in scope and quality as a dissertation for the degree of Doctor of Philosophy.

Robert Huggins

Approved for the Stanford University Committee on Graduate Studies.

Patricia J. Gumport, Vice Provost Graduate Education

This signature page was generated electronically upon submission of this dissertation in electronic format. An original signed hard copy of the signature page is on file in University Archives.

NEW MATERIALS SYSTEMS FOR AQUEOUS BATTERIES

Colin Wessells, Ph.D.

Stanford University, 2012

Abstract:

In the past few decades, a variety of battery technologies have been developed for portable electronics and vehicles. Another major energy storage application is stationary storage on the electric grid. Existing battery technologies do not offer the cycle life, power, energy efficiency, or low cost needed for widespread adoption on the grid. With the accelerated deployment of volatile renewable energy sources such as solar and wind, the need for energy storage to smooth and balance generation and load on the grid will only increase.

Batteries that use aqueous electrolytes have several advantages when compared to the commercial lithium ion batteries that contain organic electrolytes. Water is much less expensive than the organic solvents used in commercial cells. It is also nonflammable, so aqueous cells do not have the safety hazards associated with batteries that contain organic electrolytes. Furthermore, aqueous electrolytes have much higher ionic conductivities than organic ones, so aqueous cells can achieve higher energy efficiency.

In the first part of this thesis, the development of aqueous lithium ion batteries is discussed. The well-known LiCoO_2 cathode was adopted from its common use in organic cells and shown to have long cycle life in aqueous LiNO_3 . Next, a new synthesis method was developed to produce carbon-coated nanoparticulate $\text{LiTi}_2(\text{PO}_4)_3$ for use as an anode in aqueous cells. This anode had long cycle life in aqueous Li_2SO_4 , retaining 89% of its initial capacity after 100 cycles at a C/5 rate. Its low reaction potential of -0.5 V vs. H^+/H_2 resulted in 1.5 V cells when combined with common lithium ion cathode materials.

In the second part of this thesis, the use of Prussian Blue analogues as battery electrodes in aqueous potassium ion and sodium ion cells is presented. These materials have a face centered cubic open framework structure that allows for rapid electrochemical cycling of alkali ions. A new co-precipitation synthesis method was developed to produce highly crystalline, nanoparticulate Prussian Blue analogues. These materials have extremely fast kinetics and long cycle life when operated as battery electrodes in aqueous electrolytes. For instance, the copper hexacyanoferrate cathode retains 67% of its maximum discharge capacity when cycled at a 83C rate. It also retains 83% of its initial capacity after 40,000 deep discharge cycles at a 17C rate. Similar performance was observed for a related cathode material, nickel hexacyanoferrate. The fast kinetics and long cycle life of Prussian Blue analogues are due to the stable open framework structure, which has low strain during electrochemical cycling.

The open framework structure of Prussian Blue analogues allows them to intercalate many species. Both copper hexacyanoferrate and nickel hexacyanoferrate were found to cycle reversibly in electrolytes that contained Li^+ , Na^+ , K^+ , or NH_4^+ . For both cathode materials, higher reaction potentials were observed during the insertion of heavier alkali ions that have larger hydrated radii.

The effect of chemical composition on the physical and electrochemical properties of the copper/nickel hexacyanoferrate system was also examined. Scanning transmission electron microscopy energy dispersive X-ray spectroscopy found chemical homogeneity in individual nanoparticles of copper/nickel hexacyanoferrate. The lattice parameter and electrochemical reaction potentials were found to vary almost linearly with composition. Together, these results show that copper and nickel form a solid solution on particular lattice sites in the framework structure. In addition, the reaction potential of copper/nickel hexacyanoferrate can be tuned to a desired value to maximize battery performance.

Full cells were built using a copper hexacyanoferrate cathode, an activated carbon/conductive polymer anode, and an aqueous potassium ion electrolyte. These batteries had a 1.1 V average voltage, 92% energy efficiency during cycling at a 10C rate, zero capacity loss after 1,000 cycles, and a specific energy of nearly 10 Wh/kg. Because of their high performance, these batteries show promise for stationary storage applications including those on the electric grid.

Table of Contents:

Abstract	iv
Table of Contents	vi
List of Tables	xi
List of Illustrations	x
<u>Part 1:</u>	
Chapter 1: Introduction and Motivation	1
1.1 Introduction to This Thesis	1
1.2 Thesis Structure and Summary	2
1.3 Copyright Notices	4
1.4 The Case for Energy Storage on the Electrical Power Grid	5
1.5 Types of Energy Storage Technology for the Grid	9
1.6 Motivation for Aqueous Batteries	13
1.7 Types of Aqueous Batteries	14
<u>Part 2:</u>	
Chapter 2: Introduction to Aqueous Alkali-Ion Batteries	16
2.1 Choosing Electrodes for Aqueous Batteries	16
2.2 History of Aqueous Lithium-Ion Batteries	17
2.3 History of Aqueous Sodium-Ion Batteries	19
2.4 Prior Studies of Potassium-Ion and Ammonium-Ion Electrodes	19
Chapter 3: Extending The Limited Electrochemical Stability Range of Aqueous Electrolytes	21
3.1 Introduction to Aqueous Electrolytes	21
3.2 The Thermodynamic Stability of Water	21
3.3 The Kinetic Stability Range of Aqueous Electrolytes	22
3.4 Experimental Methods for Evaluating Electrolyte Stability	23
3.5 Electrochemical Stability of Aqueous LiNO_3 and Li_2SO_4 .	23
Chapter 4: The Lithium Cobalt Oxide Cathode	26
4.1 Previous Studies of Lithium Cobalt Oxide	26
4.2 Performance of Lithium Cobalt Oxide In Aqueous Cells	26
Chapter 5: Experimental Methods for Three Electrode Cells	28
5.1 The Lithium Iron Phosphate Reference Electrode	28

5.2 Three Electrode Pouch Cells	30
Chapter 6: The Lithium Titanium Phosphate Anode	31
6.1 Introduction and History of Lithium Titanium Phosphate	31
6.2 Synthesis of Carbon-Coated Lithium Titanium Phosphate Nanoparticles	33
6.3 Physical Characterization of Lithium Titanium Phosphate	34
6.4 Electrochemical Characterization of Lithium Titanium Phosphate	35
6.5 Final Comments on Aqueous Lithium Ion Batteries	37
<u>Part 3:</u>	
Chapter 7: Introduction To Prussian Blue	39
7.1 The Impetus For Developing Prussian Blue Batteries	39
7.2 The History of Prussian Blue	39
7.3 General Synthesis Methods For Prussian Blue and its Analogues	41
7.4 The Crystal Structure of Prussian Blue and its Analogues	43
7.5 Electrochemical Cycling of Prussian Blue	46
7.6 Other Applications for Prussian Blue Analogues	49
Chapter 8: Bulk Co-Precipitation Synthesis of Prussian Blue Analogue Nanoparticles	51
8.1 Motivation for Bulk Synthesis Methods	51
8.2 The Co-Precipitation Synthesis Method	51
8.3 Methods for Physical and Electrochemical Characterization	55
Chapter 9: The Copper Hexacyanoferrate Cathode	57
9.1 Physical Properties of Copper Hexacyanoferrate	57
9.2 Electrochemical Properties of Copper Hexacyanoferrate	58
9.3 Ex-situ X-ray Characterization of Copper Hexacyanoferrate Electrodes	61
Chapter 10: The Nickel Hexacyanoferrate Cathode	63
10.1 Motivation for Work on Nickel Hexacyanoferrate	63
10.2 Physical Properties of Nickel Hexacyanoferrate	63
10.3 Electrochemical Properties of Nickel Hexacyanoferrate	64
10.4 Ex-situ X-ray Characterization of Nickel Hexacyanoferrate Electrodes	65
Chapter 11: The Effects of the Identity of the Insertion Ion Species	68
11.1 Historical Background	68

11.2 The Effect of Insertion Species on Copper Hexacyanoferrate and Nickel Hexacyanoferrate	68
11.3 Final Comments on Insertion Ion Radii	73
Chapter 12: Tuning the Reaction Potential of Prussian Blue Analogues	75
12.1 Synthesis of Copper-Nickel Hexacyanoferrate Solid Solutions	75
12.2 Physical Characterization of Copper-Nickel Hexacyanoferrate Solid Solutions	76
12.3 Electrochemical Characterization of Copper-Nickel Hexacyanoferrate Solid Solutions	78
12.4 Synthesis and Physical Characterization of Metal-Iron Hexacyanoferrate Solid Solutions	80
12.5 Electrochemical Characterization of Metal-Iron Hexacyanoferrate Solid Solutions	83
Chapter 13: Prussian Blue Analogue Anodes for Aqueous Batteries	86
13.1 The Need for Prussian Blue Analogue Anode	86
13.2 Synthesis and Characterization of Titanium Hexacyanoferrate	86
13.3 Other Hexacyanometalates	88
13.4 Synthesis and Characterization of Iron Hexacyanomanganate	89
13.5 Synthesis and Characterization of Chromium Hexacyanochromate	90
13.6 Conclusions About Prussian Blue Analogue Anodes	92
Chapter 14: Full Cell Devices Using Prussian Blue Analogues	93
14.1 Introduction to the Activated Carbon/Conducting Polymer Hybrid Anode	93
14.2 Controlling the Initial Charge State of Copper Hexacyanoferrate	94
14.3 Electrochemical Performance of Full Cells	96
Chapter 15: High Voltage Full Cells Using Prussian Blue Analogues	98
14.4 Introduction and History	98
14.5 Electrochemical Performance of Copper Hexacyanoferrate in Organic Electrolytes	98
Chapter 16: Summary and Final Comments on Prussian Blue Analogues	101
References	103

List of Tables:

Table 1	Effective Stabilities of Aqueous Electrolytes vs. Current Density	24
Table 2	Compositions of Copper-Nickel Hexacyanoferrates	75

List of Illustrations:

Figure 1	Schematic of Solar Farm Power Output	6
Figure 2	Present Values of Energy Storage Applications	8
Figure 3	Worldwide Energy Storage Deployment on Electric Grids	9
Figure 4	Costs of Energy Storage Technologies	12
Figure 5	Reaction Potentials of Lithium-Ion Electrodes	17
Figure 6	Tafel Plots of LiNO_3 and Li_2SO_4	24
Figure 7	Performance of LiCoO_2 in Aqueous Cells	27
Figure 8	Three Electrode Cells and the $\text{LiFePO}_4/\text{FePO}_4$ Reference Electrode	29
Figure 9	Schematic of the NASICON Crystal Structure	31
Figure 10	Physical Characterization of $\text{LiTi}_2(\text{PO}_4)_3$	34
Figure 11	Physical and Electrochemical Characterization of Carbon-Coated $\text{LiTi}_2(\text{PO}_4)_3$	35
Figure 12	Electrochemical Characterization of $\text{LiTi}_2(\text{PO}_4)_3$	36
Figure 13	The Unit Cell of Prussian Blue	43
Figure 14	Channel and Interstice Sizes in the Prussian Blue Structure	44
Figure 15	Cyclic Voltammetry of Prussian Blue	46
Figure 16	Potential Profile of Copper Hexacyanoferrate	47
Figure 17	Physical Characterization of Nickel Hexacyanoferrate	52
Figure 18	Effects of Synthesis Conditions on Prussian Blue Analogue Crystallinity	53
Figure 19	Crystallinity and Morphology of Prussian Blue Analogues	54
Figure 20	TEM Characterization of Copper Hexacyanoferrate	57
Figure 21	Cyclic Voltammetry of Copper Hexacyanoferrate	58
Figure 22	Electrochemical Characterization of Copper Hexacyanoferrate	59
Figure 23	Ex-situ X-ray Diffraction of Copper Hexacyanoferrate Electrodes	62
Figure 24	TEM Characterization of Nickel Hexacyanoferrate	63
Figure 25	Electrochemical Characterization of Nickel Hexacyanoferrate	65
Figure 26	Ex-situ X-ray Diffraction of Nickel Hexacyanoferrate Electrodes	66
Figure 27	Effect of Insertion Ion Species on Copper Hexacyanoferrate Electrodes	69
Figure 28	Effect of Insertion Ion Species on Nickel Hexacyanoferrate Electrodes	70
Figure 29	Effect of insertion Ion Species on Electrode Cycle Life and Potential	72
Figure 30	TEM EDS of Copper-Nickel Hexacyanoferrate Solid Solutions	76
Figure 31	X-ray Diffraction of Copper-Nickel Hexacyanoferrate Solid Solutions	77
Figure 32	STEM-EDS of Copper-Nickel Hexacyanoferrate Solid Solutions	78
Figure 33	Electrochemical Characterization of Copper-Nickel Hexacyanoferrate Solid Solutions	79
Figure 34	X-ray Diffraction of Metal-Iron Hexacyanoferrate Solid Solutions	81

Figure 35	SEM of Manganese-Iron Hexacyanoferrate and Copper-Iron Hexacyanoferrate Solid Solutions	82
Figure 36	SEM of Nickel-Iron Hexacyanoferrate Solid Solutions	83
Figure 37	Electrochemical Characterization of Metal-Iron Hexacyanoferrate Solid Solutions	84
Figure 38	Reaction Potentials of Metal-Iron Hexacyanoferrate Solid Solutions	85
Figure 39	X-ray Diffraction and Cyclic Voltammetry of Titanium Hexacyanoferrate	88
Figure 40	Cyclic Voltammetry of Iron Hexacyanomanganate	89
Figure 41	X-ray Diffraction and Cyclic Voltammetry of Chromium Hexacyanochromate	91
Figure 42	Chemical Reduction of Copper Hexacyanoferrate	95
Figure 43	Performance of Copper Hexacyanoferrate/Carbon-Polypyrrole Full Cells	96
Figure 44	Electrochemical Testing of Copper Hexacyanoferrate in Organic Electrolytes	99

Chapter 1: Introduction and Motivation For This Work

1.1: Introduction to This Thesis

This thesis discusses two approaches to the development of new materials for aqueous alkali ion batteries. Batteries that use aqueous electrolytes are of interest because water is nonflammable, a good ionic conductor, and inexpensive. With the proper choice of electrode materials and electrolyte, aqueous batteries provide a safe, efficient, durable method for energy storage. Therefore, aqueous batteries are among many technologies now under consideration for stationary energy storage, although they are not currently competitive for portable applications in which weight and size are important. Many electrode materials are capable of reversibly reacting with alkali ions such as Li^+ , Na^+ , and K^+ , which makes these ions an intuitive basis for the chemistry of new aqueous batteries.

Two strategies were pursued for the development of new aqueous electrolyte batteries:

1. Aqueous lithium-ion batteries were developed by adapting two previously known electrode materials, LiCoO_2 and $\text{LiTi}_2(\text{PO}_4)_3$, for use as cathode and anode, respectively, in aqueous lithium salt electrolytes.
2. Prussian Blue analogue materials, which had previously received attention for their electrochromic properties, were developed for use as electrodes in aqueous sodium-ion and potassium-ion electrolytes.

The purpose of the first strategy was to explore the possibility of replacing the flammable, expensive organic electrolytes used in commercial lithium-ion batteries with aqueous ones. To do this, three different components of full aqueous lithium-ion batteries were studied: the electrolyte, the cathode, and the anode. Upon establishing some of the benefits and limitations for these aqueous lithium-ion batteries, attention was then turned to other alkali ion battery chemistries.

The second project in this thesis sought to develop a new family of battery electrode materials: the Prussian Blue analogues. These materials have open framework structures that allow them to rapidly react with aqueous alkali ions by an insertion mechanism. Work on these materials commenced with the hope that this open framework structure would result in electrodes with longer cycle life and higher rate capability than those in the previously examined aqueous lithium-ion batteries.

Together, the projects in this thesis illustrate two strategies for the development of novel battery chemistries. During the first, most of the work was devoted to adapting known battery electrode materials to a new electrolyte. Though intuitive, this strategy was limited by the properties of known lithium-ion electrode materials, and the use of lithium is not critical for achieving the final goal of a viable battery for stationary storage. During the second project, materials that had been studied in other contexts were adapted for use as battery electrodes. The electrochemical Prussian Blue and its analogues had long been

studied in electrochromic devices, but little attention was paid to their potential use in batteries. Adapting a known material to a new application allowed the rapid development of a new class of batteries with properties tailored for stationary storage.

1.2 Thesis Structure and Summary

The contents of this thesis are divided into four parts. The first part consists of this introductory chapter. This thesis discusses work performed on the development of new aqueous batteries. These aqueous batteries are durable, inexpensive, and safe, but have relatively low specific energy, making them best suited for stationary storage. By far the largest application of stationary storage is support for the electrical power grid, so in the remainder of this introductory chapter, a broad overview of stationary storage on the electrical power grid is presented. The limitations of existing technology and the opportunities for new aqueous battery chemistries are assessed in this context. This first part of the thesis concludes with a section motivating the choice of aqueous alkali ion batteries in particular.

In the second part of this thesis (Chapters 2-6), aqueous lithium-ion batteries are explored. After reviewing prior work (Chapter 2), the work performed for this thesis is described (Chapters 3-6).

Chapter 2 recounts the brief history of aqueous lithium-ion batteries. This literature review highlights the challenges in electrode material for these devices.

Chapter 3 describes the limited electrochemical stability window of aqueous salt electrolytes, which place constraints on the electrode materials that may be used in aqueous devices. The data in this chapter place limits on which electrode materials can be used in aqueous electrolytes.

Chapter 4 discusses the adoption of the industry standard cathode material, LiCoO_2 , to aqueous electrolytes. It includes a brief discussion of this history of this material, but focuses on work done for this thesis in which its electrochemical performance in aqueous LiNO_3 was evaluated.

Chapter 5 describes the development of the $\text{LiFePO}_4/\text{FePO}_4$ reference electrode, which allows three-electrode pressed cells to be constructed. These cells allow independent characterization of the anode and cathode, while maintaining a pressed geometry that improves cell performance.

Finally, Chapter 6 discusses the $\text{LiTi}_2(\text{PO}_4)_3$ anode: its crystal structure, its historical use as a solid electrolyte and electrode, the Pechini synthesis method developed during this thesis, and its subsequent use as an anode in aqueous lithium-ion cells.

In the third part of this thesis (Chapter 7-15), aqueous sodium-ion and potassium-ion batteries that use Prussian Blue analogue electrodes are present. After presenting a detailed review of previous work (Chapter 7), the work performed for this thesis is described (Chapters 8-17).

Chapter 7 provides a general background to Prussian Blue and its analogues, including its history, general synthesis methods, its crystal structure, and electrochemical properties.

Chapter 8 describes the co-precipitation synthesis method developed during this thesis that results in

highly crystalline Prussian Blue analogues.

Chapters 9 and 10 describe the physical and electrochemical properties of two new battery cathode materials, copper hexacyanoferrate, and nickel hexacyanoferrate, respectively. These measurements include X-ray diffraction analysis, electron microscopy, and several electrochemical techniques.

Chapter 11 examines the effect of the insertion ion species (Na^+ , K^+ , etc.) on the behavior of the electrode materials. It is shown that Prussian Blue analogues have higher reaction potentials for insertion ions with larger hydrated radii.

In Chapter 12, the inclusion of multiple species in nitrogen-coordinated lattice sites, as in copper/nickel hexacyanoferrate, is shown to affect the crystal structure, morphology, and electrochemical behavior of Prussian Blue analogues in predictable ways. Scanning transmission electron microscopy confirms the single-phase nature of the copper/nickel hexacyanoferrate system, while electrochemical measurements confirm that copper and nickel exist in a solid solution on particular lattice sites. This chapter also discusses other mixed-species hexacyanoferrate materials.

Chapter 13 describes a variety of Prussian Blue analogue anode materials, and discusses the limitations to their practical use. This chapter includes low potential hexacyanoferrate materials and broader classes of hexacyanomanganate and hexacyanochromate Prussian Blue analogues.

In Chapter 14, the electrochemical properties of full cell devices using the copper hexacyanoferrate cathode and several different anode materials are discussed.

Though the bulk of this thesis is about aqueous batteries, Chapter 15 makes a brief diversion to describe the properties of Prussian Blue analogues in organic electrolytes.

Finally, Chapter 16 concludes Part 3 with final comments summarizing the work done on Prussian Blue analogues for this thesis, as well as some proposed areas of their future study.

1.3 Copyright Notices

Some of the text and figures presented in this thesis are adapted from their forms in prior publications. In all cases, the author has retained the right to future noncommercial publishing, including for the purposes of this thesis. Some required copyright notices are now presented:

Text and figures in Chapter 3.4 are presented with the following required notice:

© The Electrochemical Society, Inc. [2010]. All rights reserved. Except as provided under U.S. copyright law, this work may not be reproduced, resold, distributed, or modified without the express permission of The Electrochemical Society (ECS). The archival version of this work was published in *Electrochemical and Solid-State Letters*, **13** (5) A59-A16 (2010).”

Figures in Chapter 6 are presented with the following required notice:

© The Electrochemical Society, Inc. [2011]. All rights reserved. Except as provided under U.S. copyright law, this work may not be reproduced, resold, distributed, or modified without the express permission of The Electrochemical Society (ECS). The archival version of this work was published in *Journal of the Electrochemical Society*, **158** (3) A352-A355 (2011).”

Figures in Chapter 11 are presented with the following required notice:

© The Electrochemical Society, Inc. [2012]. All rights reserved. Except as provided under U.S. copyright law, this work may not be reproduced, resold, distributed, or modified without the express permission of The Electrochemical Society (ECS). The archival version of this work was published in *Journal of the Electrochemical Society*, **159** (2) A98-A103 (2012).”

1.4: The Case for Energy Storage on the Electrical Power Grid

The electricity infrastructure of the United States is comprised of an electrical power grid linking energy generation sources to consumers through a transmission and distribution network. Rechargeable energy storage devices including batteries offer benefits to utilities, grid system operators, and electricity customers for a broad spectrum of applications.¹⁻¹⁴ These include the integration of intermittent renewable energy sources such as solar and wind, the mitigation of expensive short-term transient outages, and the deferral of investment in new infrastructure. As a result, energy storage capable of providing 130 GW of power is already installed on electric grids worldwide.⁶ Market analyses by the United States Department of Energy (DOE) and trade groups such as the Electric Power Research Institute (EPRI) have consistently found that integrating energy storage with the grid allows better synchronization of energy generation and demand, benefiting both the utilities and customers.^{2-4, 6-10} The DOE, EPRI, the California Energy Commission, and other observers of the grid have also reached a general consensus that new energy storage technologies must be developed and deployed on the grid in support of renewable energy.⁶⁻¹⁰ This is due in large part to the immense capital cost and limited site availability of traditional pumped hydroelectric energy storage, and the limited power, efficiency, and operational lifetime of existing battery technology. New battery technologies that may usurp existing storage methods are rapidly emerging, and it is not yet apparent which technologies will ultimately receive widespread adoption. In 2010, researchers at the DOE estimated that the market for energy storage on the grid in the United States is between \$190 billion and \$260 billion.⁷ For this reason, regulators, the utilities, battery manufacturers, and the battery research community have turned their attention to energy storage on the grid.

In the next 10-20 years, the use of renewable energy sources such as solar and wind will require as much as 50 GW and 200 GWh support from energy storage in the United States alone.⁶⁻⁷ This need for energy storage in support of renewable energy generation will emerge even sooner in California. In 2011, the California state government passed Senate Bill X1-2, which codified a previous executive order that 33% of the energy produced in California shall come from renewable sources by the year 2020.¹⁰ This bill was passed in spite of the fact that solar and wind, two of the most promising renewable generation methods, provide highly variable power and cannot reliably support the grid on their own. Their power is unreliable on timescales of seconds to hours, and from one day to the next. A solar farm, for instance, produces power only while illuminated by the sun, and its output is limited by both diurnal cycles and weather (Fig. 1).¹⁴ Load balancing strategies which pair other generative capacity and traditional energy storage technology such as pumped hydroelectric power must be employed to counter the diurnal output of solar farms. It is more challenging to smooth the abrupt changes in power that occur in the presence of clouds (Fig. 1a).⁶ Similarly, the power output of wind farms varies unpredictably throughout the day, and from one day to the next.^{2, 6} Rapid charging and discharging of energy storage capacity can be used to smoothly match the power of intermittent sources with demand (Fig. 1b).⁶⁻⁷ No commercialized energy storage technology can provide the short response time, power, energy efficiency, and cycle life needed to support the transient changes in the power of solar and wind farms.^{1, 6-7, 14-15} The rapid deployment of clean

energy generation requires either an enormous decrease in the installed costs of existing technology or disruptive new technology with both lower cost and higher power, efficiency, and cycle life.

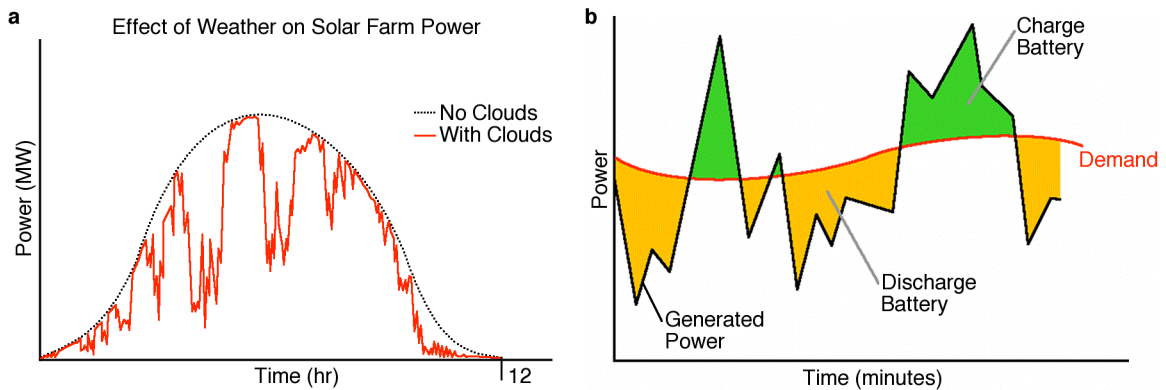


Figure 1: **a)** A solar farm provides power in the presence of sunlight, and its power varies over a diurnal cycle. However, the presence of clouds may abruptly decrease the actual power of the farm on timescales of seconds to minutes. **b)** Energy storage can be charged or discharged as needed to smoothly match the variable power output of the solar farm to demand. Area regulation uses storage in an analogous way to match constant power generation to rapid fluctuations in demand.

Energy storage can immediately improve the performance and reliability of the electrical grid in other ways that are unrelated to renewable energy generation. A first example is its ability to prevent or limit transient outages. Many of the power outages in the United States last for no more than a few minutes, shorter than the time needed to increase the output of most power plants.^{6, 13} Even momentary outages may cause extended interruptions in activity for industrial electricity customers. Outages are responsible for an estimated \$100 billion annual reduction in economic activity.¹³ Distributed energy storage that provides local grid support could alleviate the toll of transient outages.^{3, 6, 7-9} In particular, batteries are attractive for this application, as they may be installed in desired quantities at many locations. With the exception of a few remote communities that have relied on batteries for backup power, the use of energy storage to avoid transient outages remains unrealized.^{6, 14-15}

Another application for short-duration energy storage on the grid is area regulation.⁷ Energy generation by conventional power plants that burn coal or natural gas can be readily adjusted to match customer demand. This occurs throughout the grid on daily, weekly, and seasonal cycles, and general trends for the times and durations of peak energy use are well known. However, it is inefficient to rapidly ramp the output of power plants to match the fluctuations in demand that occur on shorter timescales of a few seconds to a few minutes. To avoid the costs of excess generation or frequent brownouts due to inadequate generation, regional utilities and system operators engage in area regulation, during which excess power from one area of the grid is transferred to another area in which demand has temporarily exceeded generation.⁷ For example, in the case of a momentary local shortage in generation, power from outside sources provides up regulation to meet the demand. Conversely, a local excess in generation results in

down regulation, during which power is supplied to another part of the grid. Energy storage could make area regulation more efficient by allowing power plants to operate at nearly constant outputs, with a supplemental discharge or charge of the storage device adjusted in real time to match demand.⁷

Annual peak electricity demand and generation occurs for only about 400 hours, or for 5% of the year.⁶ However, both the generation capacity and transmission infrastructure must be able to meet peak demand. This means that the full output of power plants and the full bandwidth of the transmission and distribution grids are rarely used. Meeting peak demand with distributed energy storage would defer investment by utilities and system operators in new generation plants and infrastructure.⁶⁻⁷ Batteries are especially attractive for transmission and distribution upgrade deferrals because they can be deployed throughout the grid. Transportable batteries could be used to delay infrastructure investments at one location for some time before being moved to another location for the same application.^{3, 6-9}

These are just a few of the numerous applications for energy storage on the electrical grid. In some cases, such as support for renewable energy generation, the need for energy storage is relatively small, but growing rapidly. Other applications that are related to the reliability and performance of the grid already demand large storage capacities. In the next ten years, a market for storage capable of providing up to 350 GW is expected to develop. For some applications, such as providing support for a solar farm, large storage facilities capable of ~100 MW and 500 MWh may be installed.¹⁰ Yet for other applications, such as distributed storage at substations or deferral of infrastructure investment, smaller storage facilities providing less than 1 MW and 10 MWh may also become common.⁶⁻⁹

Depending on the application, different participants in the grid benefit from energy storage. For example, a public utility or an independent power producer might save money by using energy storage, rather than a natural gas power plant to smooth the output of a solar farm.⁶⁻⁷ Smaller municipal utilities may derive benefits from distributed storage for area regulation and infrastructure deferrals.⁹ Electricity customers with their own storage capacity will benefit if it allows them to avoid the purchase of electricity during times of peak demand (and higher rates).⁶⁻⁷ Most of the analyses of the value of energy storage focus on the direct benefit of the use of energy storage for an application to the owner of the storage. The DOE has estimated the total market for storage on the grid to be between \$190 billion and \$260 billion in the next 10-20 years.⁷ In addition, the DOE has found that the total economic loss due to power outages is in excess of \$100 billion annually.¹³ Though the benefit of energy storage will be monetized primarily by the utilities and independent power producers, its benefits will be felt throughout the economy.

The DOE has publicized two major cost targets for new energy storage technology: \$100/kWh and \$0.025/kWh-cycle, where the latter target is equal to the installed cost of the energy, divided by an operational lifetime of 5,000 charge/discharge cycles and an expected energy efficiency of 80%.¹⁶ The \$100/kWh DOE target was originally calculated at EPRI.³ The model used to derive this target assumed that utilities would store energy during times of low demand, and then use it to supplement generation from power plants to meet peak demand. This is a relatively low-value application. Exhaustive analyses by researchers at Sandia National Laboratory and EPRI have since concluded that the values of many storage

applications are actually higher, and especially so for niche markets (Fig. 2).⁶⁻⁷ An extreme case is that of short-duration frequency regulation, which is the maintenance of the 60 Hz alternating voltage and current of the grid signal, and which has an estimated present value of \$4000-7000/kWh (Not shown in Fig. 2).⁶

In summary, there is a vast array of applications for energy storage on the grid. In coming years, the widespread use of solar and wind for generation will demand supportive energy storage capacity. Utilities and independent power producers already can use storage to limit the effects of outages, to balance generation with demand, and to avoid some investments in new infrastructure. The DOE has placed a target cost for new energy storage technology to reach broad market penetration at \$100/kWh, while other analyses have found higher values for certain storage applications. The amount of storage on the grid is expected to grow rapidly if it can be procured at a reasonable cost.

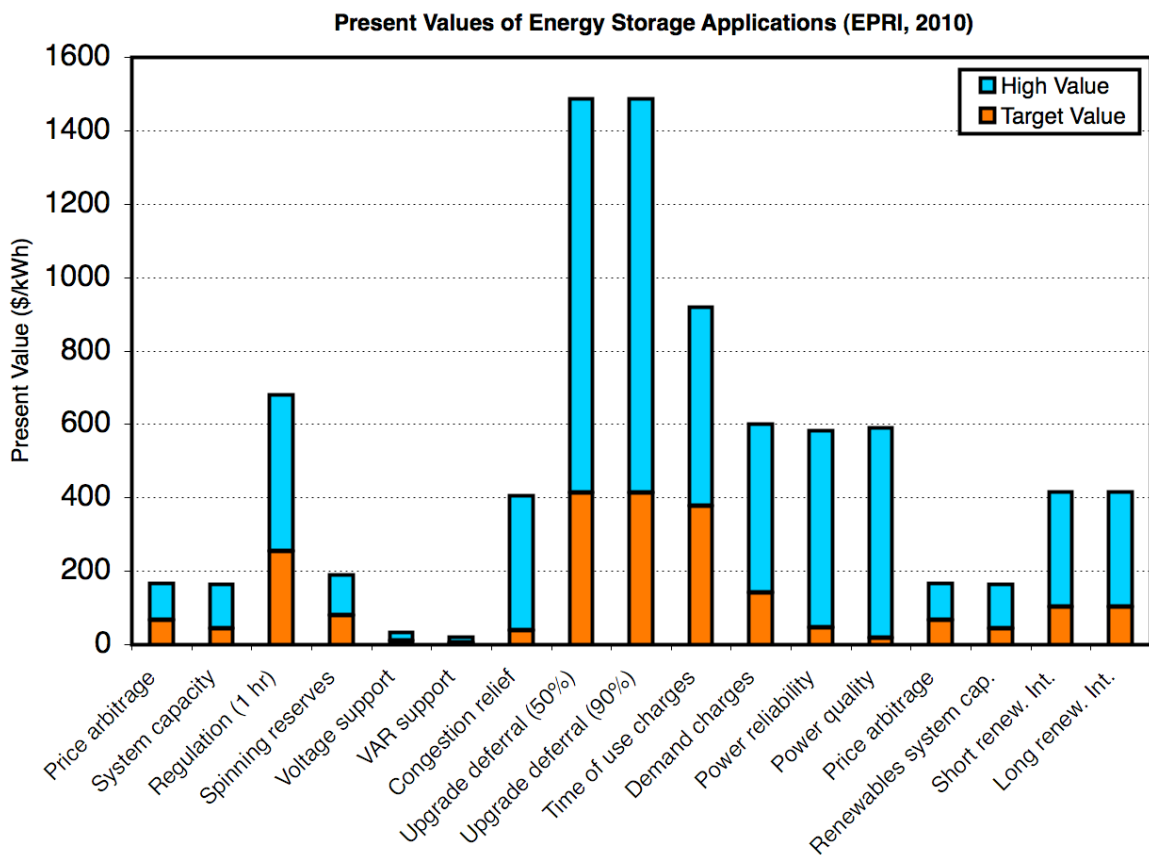


Figure 2: The present values of many applications for energy storage on the electrical grid. Present value roughly estimates the price of the storage at which the use of storage results in savings for the owner. The details of its calculation are discussed by EPRI in Ref. 6. Target values represent the price needed for broad market penetration for storage for a particular application, while the high values represent the price needed to justify the use of storage in niche markets. All data are adapted from Ref. 6 and 7.

1.5: Types of Energy Storage Technology for the Grid

The most common methods for energy storage on the electrical grid may be categorized as mechanical storage or electrochemical storage. Mechanical energy storage technologies include pumped hydroelectric power, compressed air energy storage, and flywheels, while the electrochemical energy storage devices in consideration for the grid are batteries and electrochemical double layer capacitors (hereafter, capacitors). The total energy storage installed worldwide on electrical grids produces about 130 GW of power. As of 2010, pumped hydroelectric power accounted for over 99% of this, and fewer than 370 MW of batteries were installed on electric grids worldwide (Fig. 3).^{6, 14}

Worldwide Energy Storage Deployment on Electric Grids (2010)

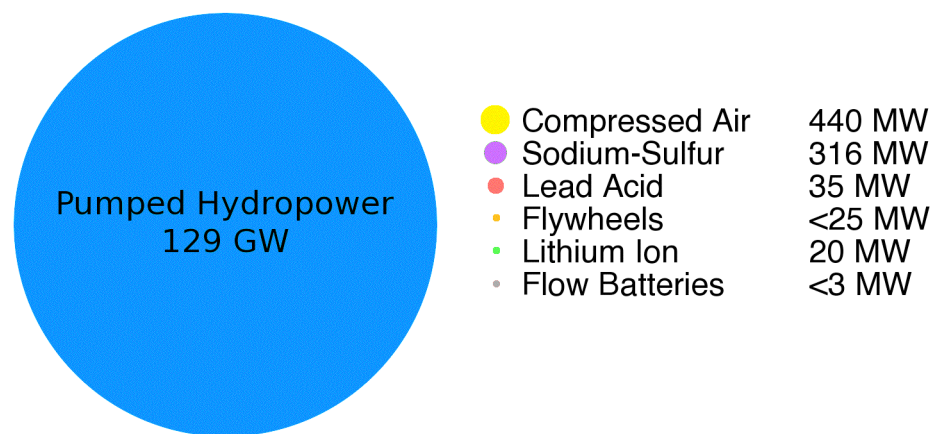


Figure 3: Worldwide power provided to electrical grids by various energy storage technologies, as of 2010. Pumped hydropower provides over 99% of power. All data from Ref. 6.

Pumped hydropower has long been used for large-scale energy storage. During temporary declines in demand, excess power may be used to pump water above a dam and into a reservoir. At later times of increased demand, water can be discharged through the dam's turbines to create electrical power. Pumped hydropower provides 40 GW in the United States, and 129 GW worldwide.^{6, 11} Integration of pumping systems with existing dams historically made pumped hydropower a simple, cost effective method for creating new energy storage capacity. Today, pumped hydropower provides energy storage capacity at a cost of less than \$100/kWh, which is cheaper than any other large-scale storage technology.¹⁶ Other advantages of pumped hydropower include their rapid response, long operational lifetime (at least 50 years), and large absolute capacity (10 GWh or more). However, pumped hydropower is plagued by low round trip energy efficiencies of 60-70%.^{6, 14, 17} Energy loss occurs primarily by evaporation: not all of the water pumped uphill is available later for discharge. Though pumped hydropower is currently ubiquitous, the construction of new pumped hydropower facilities will be limited in the United States because of their extraordinary capital cost, strict requirements on local topography, and regulatory challenges.

A second method for large-scale mechanical energy storage is compressed air.^{6, 10, 14} During times of

off-peak demand, inexpensive excess electricity is used to power a compressor that pumps air into a large storage facility. The storage facility is typically an underground cavern or mine, but in recent years, aboveground compressed air energy storage using large tanks has also been studied.^{10, 14} Construction of underground compressed air energy storage facilities is limited by local geology. Underground facilities provide capacities of several GWh. When additional power is demanded, pressurized air is released from the storage chamber, heated using fossil fuel combustion to further raise its pressure, and passed through the drive train of a generator to provide power to the grid. The heating step performed as the air is released from the reservoir results in an energy output greater than the energy needed to initially compress the air.³ Nevertheless, compressed air energy storage suffers from terrible round trip energy efficiency of 45-55%.^{6, 10, 14} Despite a large capital investment needed for construction, this technology provides storage capacity at a cost of about \$100/kWh. Though only one compressed air energy storage plant is currently operated in the United States, its low cost may soon lead to its wider use.

Mechanical flywheels may provide another form of mechanical energy storage for the grid. In them, rotational energy is stored in magnetically levitated disks that rotate at rates between 10^4 and 10^5 rpm.¹⁰ Unfortunately, recent efforts to commercialize flywheels have failed, in large part due to their dreadfully high cost per energy stored of \$8000/kWh.¹⁰ This high cost per energy results from their low energy density, which is derived from the relatively small amount of energy stored by rotational motion. However, flywheels' ability to charge and discharge extremely rapidly results in high power at a relatively low cost per power of \$150-350/kW.¹⁰ They also offer high round trip energy efficiencies of over 90%. Flywheels have been demonstrated to operate for tens of thousands of cycles when properly serviced, and with a large decrease in cost, may someday prove desirable for short-duration applications such as area regulation.

The electrochemical energy storage devices in consideration for use on the electrical grid may be divided between capacitors and batteries.¹⁰ Capacitors typically contain two electrochemically inert activated charcoal (AC) electrodes with high surface areas. During capacitor charging, a double-layer of electrolyte ions builds up on the polarized surfaces of the two electrodes, and it dissipates during discharge.¹⁸ The specific capacities of capacitors are much lower than those of batteries because the only charge mechanism is this non-Faradaic formation of the electrical double layer on the electrode surfaces. The voltage of a capacitor varies linearly with charge state. As power scales with the square of the voltage of an electrochemical cell, only a small fraction of the total charge capacity of a capacitor provides useful power. This results in very low specific energies of about 5 Wh/kg, about one order of magnitude lower than some battery technologies.¹⁸ But, as capacitors are charged and discharged by physical formation and dissipation of the electrical double layer on the electrode surfaces, they are capable of extremely high power and long cycle life. Some commercial capacitors may be fully discharged in seconds to provide specific power of up to 10^4 W/kg, while lasting 10^5 cycles or more.^{1, 10} Though capacitors offer energy efficiencies of over 90% during constant charge/discharge cycling, they are prone to self-discharge, which limits their utility for long-term storage. Due to their monstrously high cost of \$10⁴/kWh, no major capacitor systems have been installed for storage on an electrical grid as of 2011.

Several battery technologies have been adapted from other applications for use on the grid. Lead acid cells, best known for their use as starter batteries in vehicles, were the first to be deployed on the grid. As early as the 1870s, the original Planté cells were used in some of the first electric plants for load leveling and peak demand management.¹ More recently, a large 10 MW/40 MWh lead acid battery facility using cells produced by General Electric was operated by Southern California Edison between 1988 and 1997. The round trip energy efficiency of the entire system was about 70%, typical of large lead acid batteries.¹ Lead acid batteries are attractive for stationary storage applications because of their relatively low cost: only \$200-300/kWh for the cells, and \$400-1000/kWh for the facilities that use them.^{6-7, 10} Commercial lead acid cells can last 2,000 cycles or more if only shallow discharge (20-50%) occurs.¹⁴ Unfortunately, the cycle life of lead acid batteries decreases severely during deep discharge. This results in a useful specific energy of 5-15 Wh/kg, even though the full specific capacities of most commercial lead acid cells are 20-30 Wh/kg.¹ Lead acid cells cannot be charged or discharged in much less than an hour, so they also have low specific powers of 20-40 W/kg. As they have low cycle life, specific energy, and specific power, the principle attraction of lead acid batteries is their low cost.

Sodium-sulfur (NaS) batteries have also been commercialized for large-scale stationary storage. The largest current manufacturer is NGK Insulators in Japan, which produces 50 kW/300 kWh modules, and which has sold about systems capable of a cumulative 300 MW.⁶ NaS batteries operate at about 300° C, and maintaining this high temperature requires thermal energy.¹⁵ Using the electrochemical energy of the cell to heat itself results in an effective self-discharge and low energy efficiency of 75-90%. NaS cells offer a specific energy of 100 Wh/kg, much higher than that of lead acid batteries. But, as NaS cells are operated only at low rates (typically a six hour charge or discharge),¹⁰ they have a low power density of 15-20 W/kg. About 5000 deep discharge cycles have been demonstrated. The installed cost of commercially available cells is about \$550/kWh, low enough to justify their use for some energy storage applications on the grid that do not require extremely high power.¹⁰ In late 2011, a large fire occurred at NGK, and in its aftermath the company has both suspended production and asked its customers to halt use of installed systems pending completion of an investigation into the cause of the fire.¹⁹

Flow batteries have recently garnered substantial attention as an alternative technology for energy storage on the grid. Unlike conventional batteries that rely on the voltage difference between the electrochemical redox couples in two solid electrodes to store energy, flow batteries use two different liquid solutions in the electrodes that contain soluble species capable of undergoing changes in their oxidation states. For example, the most common flow battery relies on the voltage difference between a $\text{VO}_2^+ / \text{VO}^{2+}$ cathode and a $\text{V}^{3+} / \text{V}^{2+}$ anode.¹⁴ Each electrode solution contains concentrated sulfuric acid. During charging, VO^{2+} is oxidized to VO_2^+ at the cathode, V^{3+} is reduced to V^{2+} at the anode, and protons flow across an electrolyte membrane between the electrode solutions.¹⁴ During discharge, the reverse reactions occur at each electrode. These cells have a variable voltage centered around 1.4 V. Flow batteries have low energy densities of 20-30 Wh/kg, but their capacities are constrained only by the size of the tanks that contain the electrode solutions. Their specific power is limited to 5-10 W/kg because of the kinetic

barriers to the rapid transfer of electrons to and from solid current collectors to the active solute species. These kinetic barriers also result in a large drop in the voltage during discharge, an increase in voltage during charge, and therefore, a low energy efficiency of 70-80%.^{10, 14} Such flow batteries last for several thousand deep discharge cycles and their cost of about \$600/kWh makes them possible candidates for some low power applications on the grid.⁶⁻⁷

Finally, the lithium-ion batteries that have attained ubiquity in portable electronics have also received attention for some grid applications. Lithium-ion cells have high voltages (3.4-4.2 V) and their electrodes have high specific capacities (130-370 mAh/g), which together result in remarkably high specific energies and powers of up to 150 Wh/kg and 500 W/kg, respectively.^{1, 6-7, 10} Lithium-ion cells also have good cycle life, and some manufacturers have demonstrated over 10^4 deep discharge cycles on small scales.¹⁴ However, the organic electrolytes necessary to attain such high voltages are extremely flammable, and cells are known to catch on fire or explode.²⁰ Another detriment to lithium-ion batteries is their extremely high cost. For example, Southern California Edison recently completed installation of lithium-ion cells in the enormous Tehachapi Wind Energy Storage Project, which provides 32 MWh support capacity for a large wind farm at a cost of \$635 million.¹⁰ This installed cost of \$1800/kWh is typical for large-scale lithium-ion systems. The high cost of lithium-ion systems has required large government subsidies for their installation by utilities and independent power producers. Nevertheless, should their cost fall by a factor of 5-10, their high performance will result in widespread deployment on the grid.

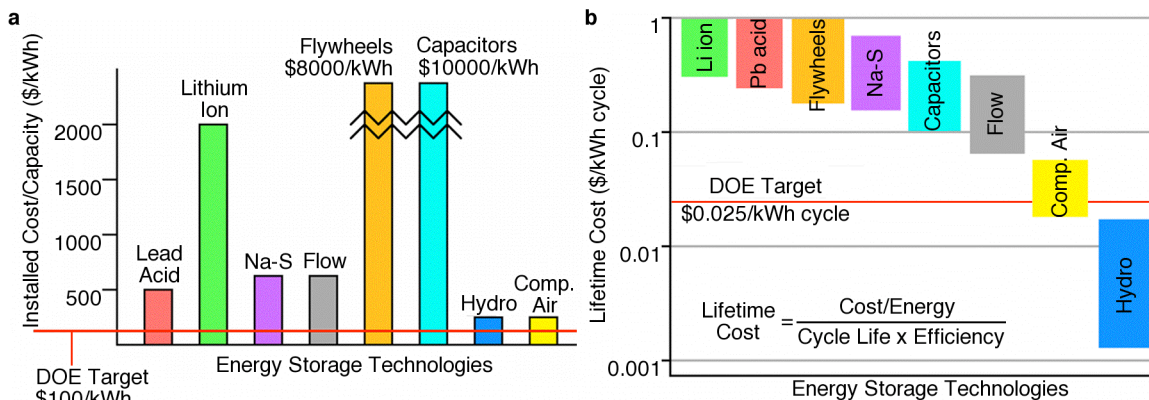


Figure 4: a) Installed costs of various energy storage technologies, with the DOE target indicated. b) Lifetime costs of various energy storage technologies and the DOE target. All data are adopted from Ref. 6-7, 10.

A complete discussion of the relationship between the power, energy efficiency, and cycle life of each storage technology and its usefulness for particular applications on the grid is beyond the scope of this text. However, it is instructive to compare the installed and lifetime costs of existing technologies to the DOE targets for broad market penetration. This is done in Fig. 4, which shows that for all storage technologies except pumped hydropower and compressed air energy storage, there is a large cost gap between the DOE

targets and the present installed (Fig. 4a) and lifetime (Fig. 4b) costs. Improving the cycle lives of the battery technologies by tenfold or more could push down their lifetime costs to a level close to the target of \$0.025/kWh-cycle. However, as battery manufacturing is already performed on large scales, large decreases in the installed cost of existing technologies will prove challenging. Reaching the DOE target of \$100/kWh will require new technology.

1.6: Motivation for Aqueous Batteries

The gap between the costs of existing battery technology and the present values of most storage applications on the grid currently limits the practicality of batteries for these applications. Any new battery technology designed specifically for use on the grid must be inexpensive when produced and installed on large scales. Therefore, before attempting to develop new types of batteries, it is worthwhile to consider what properties a device should have so that it can be produced cheaply. In many battery systems the materials used in the cell account for the majority of its cost. Such is the case of lithium-ion batteries: between 70% and 80% of the cost of commercially available cells results from the costs of the electrode materials, current collectors, separator, electrolyte, and other cell components.²¹ The organic electrolytes used in lithium-ion batteries are not only flammable and toxic, but also extremely expensive. Achieving a stable 4 V cell voltage without electrolyte decomposition or other deleterious chemical reactions requires high purity organic solvents that are electrochemically stable over a wide potential range, and that passivate any initial decomposition on the electrode surfaces. Such electrolytes allow lithium-ion batteries to achieve the high specific energy and power needed for vehicle propulsion. For stationary storage, however, specific energy and power are less important than low cost, safety, and long cycle and calendar lifetimes.^{6, 8} The use of an inexpensive aqueous electrolyte would drastically reduce the cost of lithium-ion batteries while resolving their current safety problems.

Several types of electrochemical cells that use aqueous electrolytes have already been commercialized. Lead acid batteries typically use concentrated aqueous sulfuric acid, while nickel-cadmium and nickel-metal hydride cells use concentrated aqueous potassium hydroxide.^{1, 14-15} Some capacitors have been studied using aqueous potassium hydroxide electrolyte, though an acetonitrile electrolyte is used to in the high voltage cells.¹ Flow batteries typically carry their active redox species in aqueous electrode solutions.¹⁴ As discussed above, these technologies do not have the low cost needed for widespread deployment on the grid. However, the bulk of their cost is not derived from their electrolytes, but rather, insufficient electrode capacity and cycle life (for lead acid), expensive electrode materials (nickel-metal hydride), very low specific energy (capacitors), or a combination of these problems (flow batteries).^{6-7, 10}

Aqueous electrolytes offer not only better safety and lower cost than organic ones, but also have higher ionic conductivity. For example, concentrated aqueous LiClO_4 has an ionic conductivity of about 150 mS/cm, but if water is replaced by propylene carbonate, the ionic conductivity decreases to about 5 mS/cm.²²⁻²³ A more recent study showed that concentrated aqueous LiNO_3 has an ionic conductivity 17 times greater than that of 1 M LiPF_6 in a mixture of ethylene carbonate and diethyl carbonate, a commonly

used electrolyte in organic lithium-ion cells.²⁴ Higher electrolyte ionic conductivity results in a lower resistance during cell cycling. Given the same electrodes and geometry, the use of a more conductive electrolyte will result in higher energy efficiency and power. Aqueous electrolytes are therefore attractive for energy storage applications on the grid, which frequently require that storage devices have both of these properties.

1.7: Types of Aqueous Batteries

As discussed above, aqueous lead acid, nickel/metal hydride, and flow batteries have already been commercialized. Recent reviews of battery technology by the DOE and EPRI have discussed the merits and detriments of each technology in the context of storage on the energy grid.⁶⁻⁷ Three other types of aqueous batteries, however, have received less attention elsewhere, but have relevance to the work performed for this thesis. These are aqueous lithium-ion, sodium-ion, and Prussian Blue batteries. Aqueous lithium-ion batteries have been studied for nearly twenty years as an alternative to their widely used organic counterparts.²⁵ Extensive study of electrode materials for use in organic electrolytes resulted in the unexpected development of some of these electrodes are also suitable for use in aqueous electrolytes. More recently, aqueous lithium-ion batteries using a LiMn_2O_4 cathode or a $\text{LiTi}_2(\text{PO}_4)_3$ anode were shown to have very long cycle life.²⁶⁻²⁷ The origins of aqueous lithium-ion batteries and important milestones in their development will be discussed in Chapter 2.

Aqueous sodium-ion batteries have received attention from the scientific community only recently. As sodium salts are more abundant and less expensive than lithium salts, they are an intuitive choice for an ultra-low cost battery. Unfortunately, few sodium-ion electrodes that cycle reversibly in aqueous electrolytes are known. Recently, however, some prominent battery scientists have turned their attention to sodium-ion electrodes, so this field may grow rapidly in the near future.²⁸⁻³⁴

Aqueous sodium-ion cells relying on a MnO_2 cathode and an activated carbon anode in a neutral Na_2SO_4 electrolyte were first demonstrated in 2008.²⁸ Soon afterwards, similar cells using a Na_xMnO_2 cathode were developed.²⁹⁻³¹ Activated carbon, a common capacitor electrode, was used as the anode in these studies because at the time, there was no well-known sodium-ion insertion material with a suitable reaction potential. Capacitive electrodes have extremely low capacities, and the use of activated carbon limited the capacity and energy of the aqueous NMO/carbon cell. In spite of this, the cost of this technology was low enough that it was rapidly commercialized. Even more recently, a $\text{NaTi}_2(\text{PO}_4)_3$ anode was demonstrated in aqueous electrolytes.³⁴ This material has a high specific capacity and an attractive reaction potential for use as an anode, and its future use with cathodes such as NMO or related MnO_2 phases may result in aqueous sodium-ion batteries with high capacity and energy.

The study of Prussian Blue battery electrodes began in 1979, just a year after the initial discovery that materials with the Prussian Blue crystal structure could undergo reversible electrochemical cycling.³⁵⁻³⁷ These studies typically used electrodeposited thin film electrodes of interest for electrochromic devices, and that were never scaled up to yield energy storage devices with practical capacities.³⁶⁻⁴⁶ A thorough

discussion of the history of Prussian Blue batteries will be presented in Chapter 3.

Though these three aqueous battery chemistries have been studied in some detail in recent years, it is likely that others may soon be demonstrated. The allure of a low cost electrolyte will continue to draw the attention of battery scientists who hope to develop devices less costly than those commercialized today. The principle requirement of electrodes that are chemically stable and that have reaction potentials within the electrochemical stability range of an aqueous electrolyte is not onerous, and many materials may have these properties. The rapidly growing need for low cost energy storage, including for stationary storage applications including the electrical grid, will drive further research on new battery systems, including ones that use aqueous electrolytes.

Chapter 2: Introduction to Aqueous Alkali-Ion Batteries

2.1 Choosing Electrodes for Aqueous Batteries

Commercial lithium-ion batteries contain organic electrolytes primarily comprised of ethylene carbonate and diethyl carbonate. The electrochemical stability of these organic solvents allows organic lithium-ion cells to operate at high voltages over 4 V, resulting in higher specific energy and power than any other battery chemistry. However, these organic electrolytes are extremely flammable. For applications requiring safe devices, nonflammable batteries containing aqueous electrolytes are surely more desirable. A large research community is actively investigating numerous electrode materials for use in organic lithium-ion cells. This research has also resulted in several cathodes that have reaction potentials that make them attractive for use in batteries with aqueous electrolyte.

It is more challenging to develop battery electrodes for use in aqueous electrolytes than in organic ones because of the limited thermodynamic stability of water against electrolysis to hydrogen and oxygen. Electrolyte decomposition is an irreversible process, so it is undesirable to expend charge and energy to break down the electrolyte of the battery, rather than to charge the electrodes. Furthermore, improper choice of electrodes could result in a decomposition of an unstable electrolyte while the battery is at rest, and in effect, the battery would self-discharge. The practical stability range of aqueous electrolytes is discussed in Chapter 3. However, it is instructive to consider the thermodynamic stability range of pH-neutral water (-0.41 V to 0.82 V vs. S.H.E.) when assessing which electrode materials could operate reversibly in aqueous electrolytes.

The reaction potentials of common lithium-ion cathodes are between 3.5 and 4.2 V with respect to Li^+/Li , or 0.5-1.2 V vs. S.H.E., within or near the thermodynamic electrochemical stability range of water (Fig. 5).⁴⁷ This allows the LiMn_2O_4 , LiCoO_2 , and LiFePO_4 cathodes to be readily used in aqueous electrolytes, even though they were originally developed for organic cells. Materials with potentials between 2.5 and 3 V vs. Li^+/Li , or -0.5 to 0 V vs. S.H.E., have reaction potentials near the lower limit of the electrochemical stability of water, so they can be useful as anodes in aqueous cells. Yet, such materials are not desirable as either cathodes or anodes in organic electrolyte devices because their reaction potentials are lower than the aforementioned cathodes, but much higher than common lithium-ion anodes such as graphite. As a result, materials with reaction potentials in that range were rarely studied, and few are known today. The vast majority of aqueous lithium-ion batteries have used a vanadate (VO_2 or LiV_3O_8) or lithium titanium phosphate ($\text{LiTi}_2(\text{PO}_4)_3$) anode.^{25, 27, 48-54} A few other materials including some lithium manganese oxides, and the conductive polymer polypyrrole are known to have appropriate reaction potentials and have received limited attention for use in aqueous lithium-ion devices.⁵⁵⁻⁵⁶

In summary, only a few viable lithium-ion electrode materials have been explored for use in aqueous electrolytes. The most desirable cathodes are LiCoO_2 and LiMn_2O_4 , which have high reaction potentials

near the oxidation potential of water. The most desirable anodes are vanadates and $\text{LiTi}_2(\text{PO}_4)_3$, which have low reaction potentials near the reduction potential of water to hydrogen. The combination of one of these cathodes with one of these anodes can therefore result in a full cell with a voltage of 1.2-1.5 V.

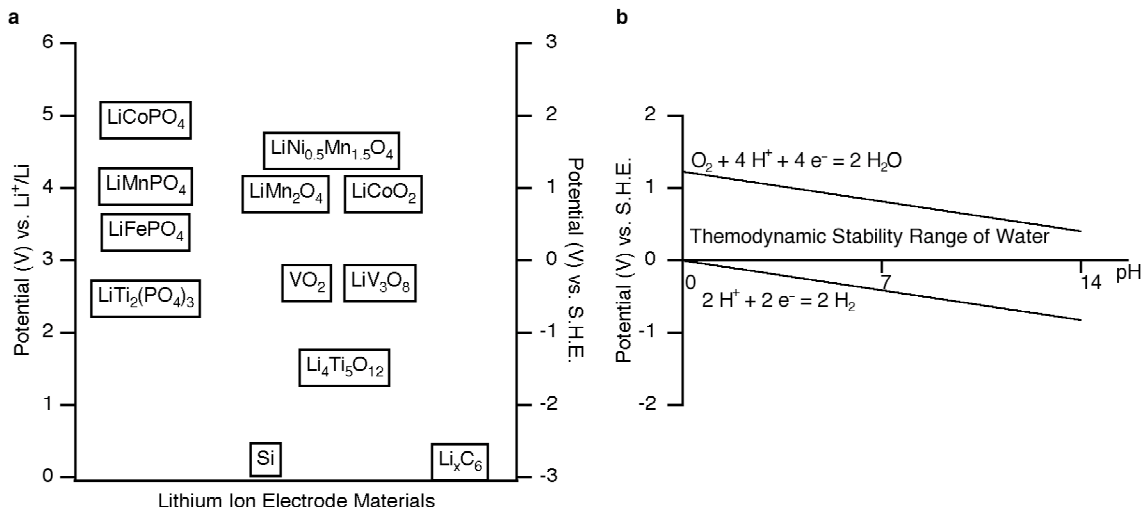


Figure 5: **a)** The reaction potentials of common lithium-ion electrodes span 0 V to 5 V vs. Li^+/Li , or -3 V to 2 V vs. S.H.E. **b)** The limited electrochemical stability range of water limits the choice of electrode materials for aqueous lithium-ion batteries to those which have reaction potentials between 2.5 V and 4.25 V vs. Li^+/Li , or -0.5 V and 1.25 V vs. S.H.E.

2.2 History of Aqueous Lithium-Ion Batteries

Li, Dahn, and Wainwright demonstrated the first aqueous lithium-ion battery in 1994, using a LiMn_2O_4 cathode, a VO_2 anode, and a 5 M LiNO_3 electrolyte.²⁵ This resulted in a full cell with an average operational voltage of 1.5 V. This relatively high voltage resulted in a specific energy of 75 Wh/kg on a basis of the mass of the electrodes. Assuming that half of the weight of a commercial battery is due to the electrodes, this means that the Wainwright cell could achieve a practical specific energy of 40 Wh/kg, higher than existing lead acid cells. Dahn and colleagues later showed that both LiMn_2O_4 and VO_2 reversibly inserted Li^+ , and not protons, when cycled in aqueous electrolytes.⁴⁸⁻⁴⁹

In later years, several other researchers studied devices relying on the LiMn_2O_4 , LiCoO_2 , or LiFePO_4 cathode. For instance, G. X. Wang and colleagues reported cells that used a LiMn_2O_4 cathode and a $\text{Li}_4\text{Mn}_5\text{O}_{12}$ anode to produce a 1.4 V cell.⁵⁵ More recently, G. J. Wang et al demonstrated cells using a LiCoO_2 cathode and a LiV_3O_8 anode.⁵⁰⁻⁵¹ Extremely short cycle life times of only tens of cycles were reported in these studies.

Longer cycle lives have been observed for cathode materials in aqueous half-cells. For instance, measurements on a LiMn_2O_4 /carbon nanotube working electrode using a reference electrode and a platinum counter electrode showed that at least 1,000 deep discharge cycles are possible in aqueous Li_2SO_4 .²⁶ The work on the LiCoO_2 cathode in half-cells reported in this thesis (Chapter 4) also cycle life of over 200

cycles.^{24, 57} The cycle lives observed for half-cell measurements on cathode materials are generally much longer than those observed for full cells.

Recently, $\text{LiTi}_2(\text{PO}_4)_3$ has begun to receive attention for use as an anode in aqueous lithium-ion batteries.^{27, 52-54} This material has a reaction potential near -0.5 V vs. S.H.E., near the potential of H_2 evolution in pH-neutral aqueous electrolytes. Cells that pair a $\text{LiTi}_2(\text{PO}_4)_3$ anode with a high potential cathode such as LiMn_2O_4 can achieve voltages of 1.5 V or more.⁵³ These cells are capable of reversible cycling at voltages greater than the 1.23 V stability window of pure water because concentrated aqueous salt electrolytes have larger effective stability window, as discussed in Chapter 3. One challenge related to the use of $\text{LiTi}_2(\text{PO}_4)_3$ is its low electronic conductivity. Successful electrochemical cycling requires the use of a large quantity of conductive additives in the electrode, or conformal carbon coating of individual $\text{LiTi}_2(\text{PO}_4)_3$ particles, or both.⁵²⁻⁵⁴ A more detailed discussion of the history of $\text{LiTi}_2(\text{PO}_4)_3$, including its use as both a solid electrolyte and an electrode, is presented in Chapter 6.

Conductive polymers have also been studied for use as lithium-ion electrodes in both organic and aqueous electrolyte batteries.^{56, 58-59} In particular, polypyrrole has been found to react with lithium at about -0.15 V vs. S.H.E., an attractive potential for an anode in pH-neutral aqueous electrolytes. Pairing polypyrrole with the LiCoO_2 cathode has resulted in 1 V cells.⁵⁶ However, the poor electronic conductivity of polypyrrole limited the performance of these cells. In this thesis, electrodes containing both polypyrrole and activated carbon were shown to have considerably better rate capability and cycle life (Chapter 14).

As shown by Luo et al in 2010, aqueous lithium-ion batteries with long cycle life can be achieved using sealed cells without oxygen in the electrolyte.²⁶ Oxygen reduction can occur along with H_2 evolution at the anode, so elimination of oxygen from the electrolyte improves the coulombic efficiency of the anode. This result is consistent with the work done for this thesis on the $\text{LiTi}_2(\text{PO}_4)_3$ anode, during which sealed cells (Chapter 5) were used.

The field of aqueous lithium-ion batteries remains small in comparison to that of organic lithium-ion cells. The only major review of this field was published by Manjunatha et al in 2010.⁶⁰ It contains a thorough description of work done on aqueous batteries until 2010.

It should be noted that there are several electrode materials are known to react with lithium at potentials within the stability range of aqueous electrolytes, but that have not yet been studied in aqueous electrolyte batteries. For instance, WO_3 is a well-known electrochromic material, with a reaction potential at about -0.2 V vs. S.H.E.⁶¹⁻⁶² Though it is known to rapidly and reversibly intercalate protons, Li^+ , Na^+ , and K^+ , it has not yet been studied in an aqueous lithium-ion battery. However, in one study, it was paired with a Prussian Blue analogue cathode in a potassium ion cell.⁴⁵ Another example of an unstudied material that could be used in an aqueous lithium-ion battery is $\text{LiFe}_2(\text{PO}_4)_3$.⁶³ This lithium-ion phosphate phase as a reaction potential of -0.2 V vs. S.H.E., much lower than the 0.45 V potential of the better-known LiFePO_4 phase. If the aqueous lithium-ion battery research community continues to grow, materials including WO_3 , $\text{LiFe}_2(\text{PO}_4)_3$, and others may be investigated as anodes.

2.3 History of Aqueous Sodium-Ion Batteries

Aqueous sodium-ion batteries have also received some attention from the research community. As sodium is far more abundant and less expensive than lithium, in principle aqueous sodium-ion batteries will have a cost advantage over aqueous lithium-ion cells.

In recent years, several research groups described aqueous sodium devices relying on a sodium manganese oxide insertion cathode and a capacitive carbon anode. Those cathodes include MnO_2 , $\text{Na}_{0.7}\text{MnO}_2$ and $\text{Na}_4\text{Mn}_9\text{O}_{18}$.²⁸⁻³¹ In $\text{Na}_4\text{Mn}_9\text{O}_{18}$, two Na^+ per formula unit may be extracted between 0.4 V and 1 V vs. S.H.E., resulting in a specific capacity of 45 mAh/g when cycled at very low current densities.³⁰⁻³¹ Unfortunately, during faster cycling the specific capacity is even lower, and only about 30 mAh/g are available at a 1.2C rate.³⁰ The performance of the $\text{Na}_4\text{Mn}_9\text{O}_{18}$ /activated carbon cells was further limited by the low capacity and sloping potential profile of the capacitive anode. Despite these limitations, commercialization of these devices began in 2010, and pilot line production is expected to begin before the end of 2012.

In another recent study, the properties of the $\text{NaTi}_2(\text{PO}_4)_3$ anode in aqueous sodium-ion electrolyte were examined.³⁴ This material has the same NASICON framework structure as the $\text{LiTi}_2(\text{PO}_3)_4$ anode used in aqueous lithium-ion batteries, except that Na^+ , rather than Li^+ , is inserted and removed from the interstices during electrochemical cycling. $\text{NaTi}_2(\text{PO}_4)_3$ was found to have a practical capacity of over 120 mAh/g at -0.5 V to -0.6 V vs. S.H.E. Its potential is near the lower limit of the stability range of pH-neutral aqueous sodium-ion electrolytes, so hydrogen gas evolution may limit its practicality. However, its high capacity makes it a promising candidate for use in aqueous sodium-ion batteries.

In this thesis, another family of sodium intercalation electrodes, the Prussian Blue analogues, is described. Those materials have an open framework structure that can accommodate large hydrated cations such as Na^+ . In one prior instance, electrodeposited thin films of Prussian Blue analogues were used in an aqueous sodium-ion battery, and though the device had good cycle life and rate capability, the μg masses of the electrodes and then use of a ruthenium-based anode limited its practicality.⁴² In contrast, the sodium-ion electrodes described in this thesis are synthesized from earth abundant precursors by scalable methods, and have much longer cycle life (Chapter 10).

2.4 Prior Studies of Potassium-Ion and Ammonium-Ion Electrodes

Aqueous potassium-ion and ammonium-ion batteries have received much less attention than the aqueous lithium-ion and sodium-ion devices. Though aqueous electrolytes containing potassium are common in nickel/metal hydride batteries, battery electrodes that reversibly react with potassium ions by an insertion mechanism are not well studied. The ionic radius of potassium is much larger than those of lithium and sodium, so fewer crystal structures are capable of reversible insertion of K^+ without suffering degradation.⁶⁴ In general, the few known potassium-ion insertion electrodes have structures containing large channels between interstitial sites.

Some phases of MnO_2 that have crystal structures containing large tunnels have been shown to react

with potassium by an insertion mechanism. The reversibility of this reaction remains poorly documented, and these materials have not been used as battery electrodes.⁶⁵⁻⁶⁶

The electrochemical properties of the well-known lithium-ion insertion electrode LiMn_2O_4 have also been studied in aqueous electrolytes containing K^+ and NH_4^+ .⁶⁷ Both K^+ and NH_4^+ were shown to reversibly insert into the LiMn_2O_4 electrode for one cycle. However, proton insertion may also have occurred, and the reaction of LiMn_2O_4 with K^+ and NH_4^+ remains poorly understood.

Prussian Blue and its analogues, which have an open framework structure containing large channels and interstitial sites, have been shown to react with potassium, ammonium, and a variety of other large insertion ions.⁶⁸⁻⁶⁹ Their ability to do so rapidly has been exploited in electrochromic devices.⁷⁰ In this thesis, Prussian Blue analogue battery electrodes are shown to reversibly insert lithium, sodium, potassium, and ammonium ions in aqueous electrolytes (Chapters 8-13).

Chapter 3: Extending The Limited Electrochemical Stability Range of Aqueous Electrolytes

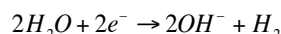
3.1: Introduction to Aqueous Electrolytes

Aqueous electrolytes are generally inexpensive, and their costs are derived primarily from salts or other additives. As such, they are far less expensive than the high purity organic electrolytes used in commercial lithium-ion batteries. Aqueous electrolytes are nonflammable, and therefore offer better safety than organic ones. Aqueous devices do not suffer the fires or explosions observed during failure of organic electrolyte lithium-ion cells.²⁰ Furthermore, aqueous electrolytes have much higher ionic conductivity than organic ones, allowing a higher energy efficiency to be achieved.²²⁻²⁴ For these reasons, aqueous electrolytes have been studied for battery applications.

3.2: The Thermodynamic Stability of Water

Water may be readily decomposed into hydrogen and oxygen by electrolysis. This limits the potential range over which electrodes in aqueous electrolytes may operate without causing electrolyte decomposition. Pure water has a 1.23 V thermodynamic electrochemical stability range, the absolute position of which varies with pH. For instance, pH-neutral water is thermodynamically stable between -0.41 V and 0.82 V vs. S.H.E.

Two water decomposition reactions can occur at potentials outside this thermodynamic stability range. At lower potentials, neutral water can be reduced, releasing hydrogen gas:



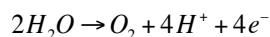
The equilibrium potential of this reaction as a function of pH and the activities of water and hydrogen can be found using the Nernst Equation:⁷¹

$$E = E^0 - \frac{RT}{2F} \ln \left(\frac{a_{H_2} a_{OH^-}^2}{a_{H_2O}^2} \right)$$

The standard potential for this reaction is the standard hydrogen electrode potential, and by convention, it is typically used as the reference for other electrochemical reactions. Setting E^0 to zero, in the case of pure water under one atmosphere of hydrogen, the Nernst Equation reduces to the well-known expression for the hydrogen evolution potential as a function of pH:

$$E = -(0.059 \text{ V}) \cdot pH$$

Similarly, at high potentials, neutral water can be oxidized, releasing oxygen gas:



Again using the Nernst Equation and substituting the standard potential of 1.23 V for the oxidation of water to oxygen, the following is found:

$$E = E^0 - \frac{RT}{4F} \ln \left(\frac{a_{O_2} a_{H^+}^4}{a_{H_2O}^2} \right) = 1.23 - (0.059) \cdot pH \text{ V}$$

Both H₂ and O₂ evolution have the same pH dependence, so the 1.23 V width of the thermodynamic stability window of pure water does not change with pH.

Though this 1.23 V window defines the range within which pure water is stable, it is not a rigorous limit on the useful potential range of aqueous electrolytes. The concentrated salts used in battery electrolytes lower the chemical activity of water because the majority of water molecules form concentric coordination shells around dissolved ions. A decrease in the activity of water results in an increase in the size of the logarithmic term in the Nernst Equation, and therefore, a lower equilibrium potential for hydrogen reduction. In the analogous equation for oxidation of water to oxygen at high potential, a decrease in the activity of water will increase the equilibrium potential for oxygen evolution. Thus, concentrated salt solutions are thermodynamically stable over a slightly wider potential window than is pure water.

3.3 The Kinetic Stability Range of Aqueous Electrolytes

Kinetic barriers to electron transfer from an electrode surface to water limit the rate at which water can be decomposed. Water may not decompose at an appreciable rate at the equilibrium potentials for hydrogen or oxygen evolution. Rather, an additional potential difference, or “overpotential” must be applied before water decomposes quickly, and its kinetic stability window will be greater than its thermodynamic one. The rate at which an interfacial electrochemical reaction occurs can be described in terms of the overpotential using the Butler-Volmer equation:⁷¹

$$i = i_0 \cdot \left(\exp \left[\frac{\alpha_{ox} n F \Delta V}{RT} \right] - \exp \left[- \frac{\alpha_{red} n F \Delta V}{RT} \right] \right)$$

Where i is the observed current density, i_0 is the exchange current density, α_{ox} and α_{red} are the oxidative and reductive charge transfer coefficients, respectively, and the overpotential $\Delta V = E - E_{equilibrium}$.

For large overpotentials, the second exponential term approaches zero and can be neglected:

$$i = i_0 \cdot \left(\exp \left[\frac{\alpha_{ox} n F \Delta V}{RT} \right] \right)$$

Rearranging this equation for ΔV results in the Tafel equation, where the constant A is the Tafel slope:

$$\Delta V = A \cdot \ln \left(\frac{i}{i_0} \right)$$

The Tafel equation can be used to determine the useful stability range of battery electrolytes. Battery electrodes typically operate at nearly constant potentials under steady state conditions. Electrochemical electrolyte decomposition at a battery electrode will result in a leakage current. This leakage current depends on the potential of the electrode, and may be approximated by the Tafel equation.

3.4 Experimental Methods For Evaluating Electrolyte Stability

A common technique used when roughly evaluating the electrochemical stability range of an electrolyte is cyclic voltammetry.⁷¹ In this dynamic technique, the potential of a working electrode is swept with respect to a reference electrode, and the current between the working electrode and a counter electrode is measured. Upon reaching a defined upper limit, the direction of the potential sweep is reversed. Scans between low and high potentials may be repeated to examine the reversibility of a reaction.

During cyclic voltammetry scans, a substantial increase in the current at high or low potentials may signal the onset of reactions involving the electrolyte. In contrast to the reversible reactions of battery electrode materials, reactions involving electrolyte decomposition are typically irreversible. This is that the onset of a large, irreversible current at extreme potentials often indicates the decomposition of the electrolyte. Unfortunately, the apparent potentials at which reactions involving the electrolyte occur can vary with the potential scan rate, the initial onset of current may be slow, and the observed current can be difficult to reproduce. For these reasons, cyclic voltammetry provides only qualitative information about the approximate electrochemical stability range of electrolytes.

Batteries are typically operated at or near relatively constant potentials, and when they are charged, are near their maximum operating potentials. Hence, steady-state measurements, rather than scanning techniques, are appropriate when evaluating the electrochemical stability of electrolytes for use in batteries. For example, the potential of a working electrode can be fixed, and the current measured over time. A non-zero equilibrium current at long times could indicate the equilibrium rate of electrolyte decomposition for an electrode at that chosen potential. Alternatively, a fixed current could be applied to the working electrode, and the equilibrium potential measured. Either of these techniques provides quantitative information about the rate of electrolyte decomposition at particular potentials.

3.4 Electrochemical Stability of Aqueous LiNO_3 and Li_2SO_4

In this work, constant current (galvanostatic) steps were applied to a flooded three-electrode cell containing platinum foil working and counter electrodes and a Ag/AgCl reference electrode.⁷² Before each measurement, the platinum foil electrodes were washed first with acetone, and then with concentrated sulfuric acid, and finally in de-ionized water. All but 1 cm² of the platinum was masked with nitrile cellulose so that the current densities at the electrode surface could be controlled. The working and counter electrodes were immersed 1 cm apart in aqueous solutions with the reference electrode between them. Galvanostatic steps were maintained for one hour, by which time the potentials of the electrodes had equilibrated. Aqueous electrolyte solutions of 5 M LiNO_3 and 2 M Li_2SO_4 were prepared from reagent grade precursors (Sigma Aldrich).

The equilibrium potentials for galvanostatic steps in 5 M LiNO_3 and 2 M Li_2SO_4 at several current densities are shown in Fig 6. The equilibrium potential varies linearly with the natural logarithm of the current density, consistent with the Tafel equation.

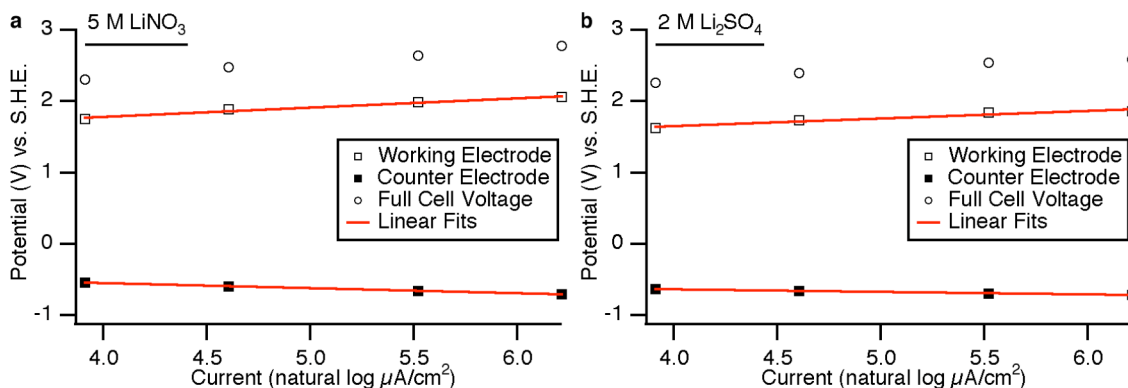


Figure 6: The equilibrium electrode potentials and full cell voltages of 5 M LiNO_3 (a) and 2 M Li_2SO_4 (b) during galvanostatic steps between two platinum foil electrodes.

Rapid self-discharge due to electrolyte decomposition would severely limit the utility of a battery, so the leakage current should be much lower than $50 \mu\text{A}/\text{cm}^2$ in practical batteries. Inconsistent and unstable potentials were measured during galvanostatic steps at lower current densities. The Tafel Equation was used to extrapolate the equilibrium electrode potentials observed between $50 \mu\text{A}/\text{cm}^2$ and $500 \mu\text{A}/\text{cm}^2$ to current densities as low as $1 \mu\text{A}/\text{cm}^2$. These extrapolated values are reported in Table 1. They approximate the useful electrochemical stability ranges of 5 M LiNO_3 and 2 M Li_2SO_4 . It must be noted that because these electrolytes were not de-aerated, both electrolysis of water to hydrogen and the reduction of oxygen gas to water occurred at the negative electrode. These two reactions have different equilibrium reaction potentials and kinetic limitations, and occur at different rates at a particular nonequilibrium potential. Thus, the extrapolation of the equilibrium potential of the negative electrode to lower current densities may not provide a meaningful estimate of the lower limit of electrolyte stability. In contrast, the only reaction occurring at the positive electrode was the oxidation of water to produce oxygen, so extrapolation of the equilibrium potential to lower current densities can be expected to provide reliable values.

Table 1: Extrapolated Equilibrium Electrode Potential (V vs. S.H.E.) vs. Current Density ($\mu\text{A}/\text{cm}^2$)

Current Density	5 M LiNO_3			2 M Li_2SO_4		
	Cathode	Anode	Full Cell	Cathode	Anode	Full Cell
1	1.254	-0.281	1.535	1.224	-0.498	1.722
5	1.465	-0.392	1.857	1.395	-0.556	1.951
10	1.556	-0.440	1.996	1.469	-0.581	2.050
25	1.676	-0.503	2.179	1.566	-0.614	2.180
50	1.767	-0.551	2.318	1.640	-0.639	2.279

Consider a hypothetical battery electrode, which contains an active material with a specific capacity of 100 mAh/g, with a mass loading of $50 \text{ mg}/\text{cm}^2$ (these values are comparable to commercial lithium-ion

electrodes). That electrode has a capacity density of 5 mAh/cm^2 , so a leakage current of $10 \text{ }\mu\text{A/cm}^2$ would fully discharge the electrode in 500 hrs, or about three weeks, if the potential of the electrode remained constant during discharge. However, during discharge the potential of a positive electrode typically decreases from its highest value, reducing the leakage current. Nevertheless, it is clear that leakage currents of less than $10 \text{ }\mu\text{A/cm}^2$ are desirable for practical battery at their operating potentials.

Adopting this current density as the maximum acceptable leakage current, 5 M LiNO_3 is stable between -0.440 V and 1.556 V vs. S.H.E., while $2 \text{ M Li}_2\text{SO}_4$ is stable between -0.581 V and 1.469 V vs. S.H.E. Battery electrodes may be expected to cycle reversibly between these potentials without electrolysis at a rate of more than $10 \text{ }\mu\text{A/cm}^2$. The kinetic stability windows of both electrolytes are about two volts, much larger than the 1.23 V thermodynamic stability window of pure water. If electrodes with reaction potentials near the limits of the kinetic stability window of the electrolyte are chosen, aqueous batteries with maximum voltages much greater than 1.23 V are possible.

It must be noted that in real batteries, the masses of the anode and cathode are nearly balanced so that neither electrode has a large excess of capacity. If one electrode has a potential that is low or high enough to result in appreciable electrolyte decomposition, but the other electrode does not, then self-discharge of one of the electrodes will occur. This results in an irreversible loss in capacity, as fully charging the electrode that suffers a leakage current requires overcharging the other electrode. Even in the case of slow electrolyte decomposition, it must occur at the same rate at both electrodes, or after many charge/discharge cycles they will have disparate charge states.

Negative electrodes in commercial lithium-ion batteries operate at potentials below the stability range of the electrolytes typically employed. Decomposition of the electrolyte results in the formation of a reaction product phase that is an ionic conductor, but an electronic insulator. This material, frequently called a solid-electrolyte interphase (SEI), prevents further electrolyte decomposition at the anode, at the cost of some loss in device capacity. The PbSO_4 phase present at both the anode and cathode of lead acid batteries also serves this function and mitigates electrolyte decomposition, even though the potentials of both electrodes are beyond the stability limits of water. Slow electrolyte decomposition still occurs in lead acid cells, resulting in low charge and energy efficiencies. Passivating SEIs are generally not present in aqueous alkali ion batteries, and future studies may find that these devices must operate near or within the thermodynamic stability range of their electrolytes to achieve long cycle and calendar lifetimes.

Chapter 4: The Lithium Cobalt Oxide Cathode

4.1 Previous Studies of Lithium Cobalt Oxide

Lithium Cobalt Oxide was one of the first high potential layered oxide cathode materials developed for lithium-ion batteries, and the first commercially available lithium-ion batteries relied on it as a cathode.⁷³ Its rhombohedral structure contains close-packed layers of O²⁻, with ordered, alternating layers of octahedrally coordinated Co³⁺ or Li⁺ between them.⁷³⁻⁷⁴ During oxidation, lithium ions are removed from the layers they occupy in the structure. This reaction may be described by:



In the case of the full removal of lithium from LiCoO₂, the specific capacity is 274 mAh/g. Only about half of this can be achieved in practice. The removal of Li⁺ from LiCoO₂ is limited by the structural instability of adjacent planes of O²⁻ when the occupancy of the Li⁺ layers is low.⁴⁷ Therefore, to ensure reversible cycling the maximum voltage during charging is usually chosen such that no more than one half of the Li⁺ is removed from the structure. A number of layer-structure oxides have been investigated.⁴⁷ Some, including lithium nickel manganese cobalt oxide, have disordered layer structures that are more stable during oxidation, and therefore, have higher practical charge capacities.

In a few instances, LiCoO₂ has been reported to cycle reversibly in aqueous electrolytes.^{24, 50-51, 57} G. J. Wang, et al demonstrated the pairing of LiCoO₂ with a LiV₃O₈ anode in aqueous LiNO₃.⁵⁰⁻⁵¹ This resulted in a cell with an average discharge voltage of about 1.2 V. In that study, LiCoO₂ electrodes were found to have specific capacities of only 50-90 mAh/g, suggesting that either not all of the LiCoO₂ was in electric contact with the current collector, or that not all of it had access to the electrolyte. Furthermore, rapid capacity loss was observed in these experiments, with only about 70% capacity retention after 12 charge discharge cycles of the full cell.

In a more recent study, the same authors paired LiCoO₂ with a polypyrrole (PPy) anode.⁵⁶ PPy was previously studied as a cathode in organic lithium-ion cells, but its reaction potential near -0.1 V vs. S.H.E. also makes it useful as an anode in aqueous cells. PPy is highly insoluble in water, making it capable of stable electrochemical cycling. These LiCoO₂/PPy cells had average voltages of 0.9 V, and little capacity loss was observed after 120 cycles. This result suggests that in some prior aqueous lithium-ion battery studies, vanadate anodes such as VO₂ and LiV₃O₈ limited the cycle life of the full cells.

4.2 Performance of Lithium Cobalt Oxide in Aqueous Cells

The electrochemical performance of LiCoO₂ in aqueous electrolytes was studied in collaboration with Dr. Riccardo Ruffo of the Universita di Milano Bicocca.⁵⁷ LiCoO₂ electrodes were prepared using standard lithium-ion cell processing techniques. Commercially available LiCoO₂ (Sigma Aldrich) was ground by hand with carbon black (Alfa Aesar) and a polyvinylidene difluoride (PVDF) binder (Kynar) before being dispersed in 1-methyl-2-pyrrolidinone (NMP). Electrodes were formed by dipping stainless steel foil into

this slurry, and then drying in air at 100° C for one hour. Typical electrodes contained 3 mg/cm² LiCoO₂ with an active area of 1 cm². Electrochemical testing was performed using flooded three electrode cells that contained a LiCoO₂ working electrode, a Ag/AgCl reference electrode, a large, partially charged Li_{0.5}Mn₂O₄ counter electrode, and a 5 M LiNO₃ electrolyte at pH = 7. The counter electrode served as a reversible lithium ion sink at a near-constant potential. Galvanostatic cycling of LiCoO₂ between 0.55 and 1.15 V vs. S.H.E. at a 1C rate was performed. Specific capacities of up to 118 mAh/g were observed between 0.9 and 1.15 V vs. S.H.E. (Fig. 7). The electrochemical cycling of LiCoO₂ in 5 M LiNO₃ is highly reversible, as 81% of the initial discharge capacity is retained after 200 cycles at a 1C rate (Fig. 7b). The coulombic efficiency was 99.8% after the first few cycles.

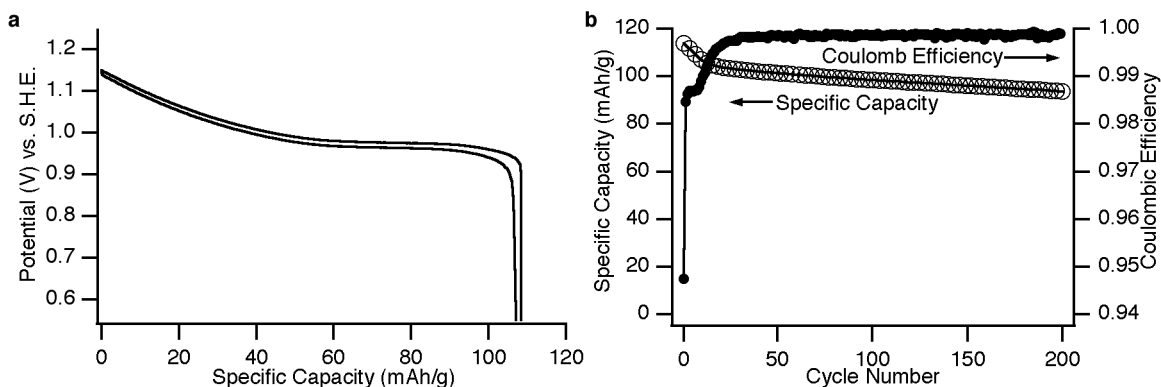


Figure 7: **a)** LiCoO₂ has a specific capacity of about 110 mAh/g when cycled at a 1C rate in 5 M LiNO₃ with an upper voltage cutoff of 1.15 V vs. S.H.E. The low hysteresis shows that this reaction is highly reversible. **b)** LiCoO₂ retains 80% of its initial discharge capacity after 200 cycles at 1C in 5 M LiNO₃. The coulombic efficiency is approximately 99.8% during cycling.

At the upper potential cutoff of 1.15 V, the potential profile of LiCoO₂ is still shallow, indicating that more capacity may be accessible at higher potentials. This was later confirmed in a separate study led by Dr. Ruffo that measured the effect of upper potential cutoff on specific capacity.²⁴ The small voltage hysteresis during cycling at a rate of 1C is in part aided by the low mass loading (3 mg/cm²), and is also consistent with the high conductivity of aqueous 5 M LiNO₃. The cycle life observed here was much greater than some of the previous studies of LiCoO₂ in aqueous electrolytes. In those studies, full cells combining LiCoO₂ with a LiV₃O₈ anode were used, and the partial solubility of the anode likely limited cell performance. Similar cycle life was observed when a PPy anode was used.

This brief study of the performance of LiCoO₂ in aqueous half-cells showed that this material has a high specific capacity and long cycle life. Attention was then turned to the development of an anode with similarly attractive properties so that full cells could be constructed.

Chapter 5: Experimental Methods for Three Electrode Cells

5.1 The Lithium Iron Phosphate Reference Electrode

Previous studies of lithium ion electrodes in aqueous cells used Ag/AgCl or other commercially available reference electrodes to measure the potential of the working electrode. The use of a reference electrode is necessary for accurate, stable, independent measurements of the operating potentials of the working and counter electrodes. However, the large size of commercially available reference electrodes usually prevents assembly of cells with the tightly pressed coin, wound, or pouch geometries of real batteries. In addition, the presence of a large reference electrode requires excess electrolyte, which may mask the deleterious effects of electrolyte decomposition or oxygen reduction at the electrode surfaces. To allow construction of a three-electrode pressed cell without excess electrolyte (Fig. 8a), a novel LiFePO₄/FePO₄ electrode was developed.

Electrochemical systems containing two pure, stoichiometric phases in equilibrium are desirable for use as reference electrodes because their electric potentials are fixed, no matter the relative quantities of the phases (in agreement with the Gibbs Phase Rule).⁷⁵ This allows stable measurement of the potentials of other electrochemical reactions. For instance, Ag/AgCl reference electrodes rely on an equilibrium of the pure solids Ag and AgCl in an electrolyte containing Cl⁻. The electrode potential depends on the Cl⁻ activity, and therefore, concentration (following the Nernst Equation), but it does not depend on the relative amounts of Ag and AgCl that are present (the activity of a pure solid is one).

Lithium iron phosphate is the best-known lithium ion cathode that has a two-phase reaction mechanism and thus, a fixed reaction potential.⁷⁶ Partial delithiation of LiFePO₄ results in the formation of biphasic particles containing pure LiFePO₄ and pure FePO₄.⁷⁷ The case of full oxidation of LiFePO₄ is described by the following expression:



For the case of a partial oxidation of LiFePO₄, the following reaction occurs:



Partial oxidation of LiFePO₄ results in a biphasic system containing LiFePO₄ and FePO₄. The potential of this reaction is 3.47 V vs. Li⁺/Li, or 0.42 V vs. S.H.E., and to a first-order approximation, it is invariant with the relative quantities of LiFePO₄ and FePO₄ present in the system. (The chemical potentials of the two phases actually do vary with the composition of the system, resulting in a small change in potential.⁷⁸)

Other lithium ion insertion electrodes including LiMnPO₄ and Li₄Ti₅O₁₂ also undergo biphasic reactions with constant potentials.⁷⁹⁻⁸⁰ As the oxidation potential of LiFePO₄ is within the electrochemical stability range of pH-neutral aqueous electrolytes, the LiFePO₄/FePO₄ system is particularly convenient for use as a reference electrode in aqueous batteries.

In this work, the following procedure was used to prepare and test $\text{LiFePO}_4/\text{FePO}_4$ reference electrodes for use in aqueous cells:

Commercially available (Hydroquebec) carbon coated LiFePO_4 , amorphous carbon black (Timcal Super P Li), and PVDF binder (Kynar HSV 900) were ground by hand and dispersed in NMP. This slurry was then deposited on stainless steel mesh substrates, and dried at 100°C in air. These electrodes were roll pressed to ensure good electrical contact between the electrode materials and the current collector.

The LiFePO_4 was then partially oxidized so that these electrodes could be used as reference electrodes. They were galvanostatically cycled at a C/5 rate in aqueous 2 M Li_2SO_4 to establish their electrochemical activity. After a time-limited 50% charge step, the open circuit potential was measured for 24 hours (Fig. 8b). The open circuit potential was 0.43 V vs. S.H.E., slightly higher than the 0.42 V standard potential for the $\text{LiFePO}_4/\text{FePO}_4$ system. This small discrepancy can be explained by the 4 M Li^+ concentration in the electrolyte. Following the Nernst Equation, an increasing Li^+ concentration in the electrolyte results in a higher reaction potential.

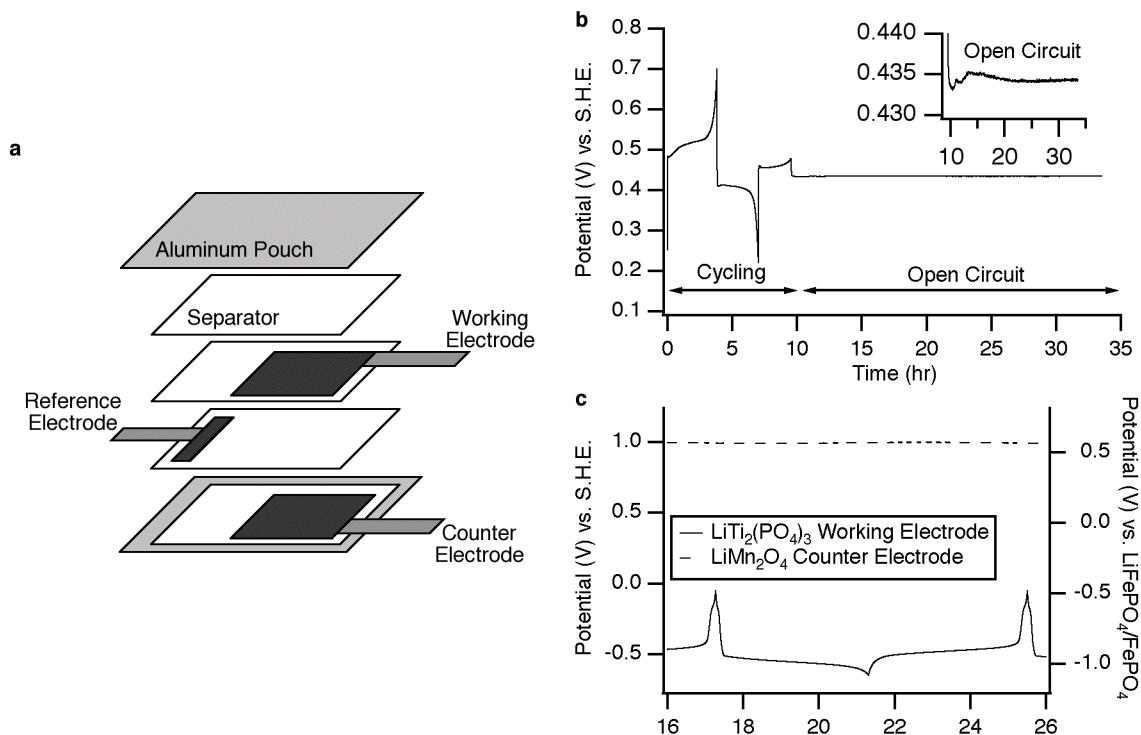


Figure 8: a) Schematic of a three-electrode pressed pouch cell. The electrode substrates were stainless steel mesh, while the current collectors were steel foil. The separators are filter paper (Whatman 42). Cells were vacuum-sealed. The extra separators behind the electrodes prevented rapid reactions with any trace O_2 gas remaining in the cell. b) Galvanostatic cycling and open circuit testing of a LiFePO_4 reference electrode immediately before insertion into a three-electrode pouch cell. c) An example of independent measurement of the potentials of a $\text{LiTi}_2(\text{PO}_4)_3$ working electrode and a LiMn_2O_4 counter electrode using the LiFePO_4 reference electrode.

5.2 Three Electrode Pouch Cells

After establishing the reaction potential of the $\text{LiFePO}_4/\text{FePO}_4$ electrode, it was used as a reference electrode in sealed pouch cells containing working and counter electrodes of $\text{LiTi}_2(\text{PO}_4)_3$ and LiMn_2O_4 . This allowed the independent measurement of the reaction potentials of those materials during full cell cycling (Fig. 8c).

Some additional comments on three electrode pouch cells should be made. Additional separators that contained electrolyte were placed behind the working and counter electrodes. They ensured that adequate electrolyte was in contact with the electrodes. Also, as the cells were assembled in air and contained de-aerated electrolyte before vacuum sealing, the additional separators ensured that the electrodes were not in direct contact with any oxygen gas that may have remained inside the pouch. Protection of the $\text{LiTi}_2(\text{PO}_4)_3$ anode from exposure to oxygen is critical to successful cycling, as its reaction potential is far below the reduction potential of oxygen.

Chapter 6: The Lithium Titanium Phosphate Anode

6.1 Introduction and History of Lithium Titanium Phosphate

A variety of cathode materials, including LiCoO_2 , are known to have good performance in aqueous electrolytes. However, the development of an anode has proved more challenging. This is because the reaction potential needed for an anode in aqueous electrolytes, about -0.5 V to 0 V vs. S.H.E., is in the middle of the electrochemical stability range of the organic electrolytes used in commercial lithium ion batteries. Use of such an electrode results in a lower voltage than the existing 4 V lithium-ion cells. For this reason, few lithium ion electrodes with reaction potentials between -0.5 V and 0 V vs. S.H.E. have been studied. One of those few is lithium titanium phosphate ($\text{LiTi}_2(\text{PO}_4)_3$). For this reason, $\text{LiTi}_2(\text{PO}_4)_3$ anodes were developed for this thesis. Before presenting that work, prior studies of this material are discussed.

Lithium titanium phosphate has the same crystal structure as the sodium super-ionic conducting (NASICON) $\text{NaZr}_2(\text{PO}_4)_3$ phase, which was first reported by Hong and Goodenough in 1976.⁸¹⁻⁸² Numerous other analogues with the same structure have also been reported.⁸³⁻⁸⁴ This rhombohedral (Space Group R3c) structure contains a framework of TiO_6 octahedra that share corner oxide ions with neighboring PO_4 tetrahedra.^{81-82, 85-86} These octahedral and tetrahedral are assembled as a three-dimensional framework of $\text{Ti}_2(\text{PO}_4)_3$ groups (Fig. 9). In stoichiometric $\text{LiTi}_2(\text{PO}_4)_3$, lithium ions fully occupy the octahedral M1 sites that lie above and below TiO_6 octahedra. Thus, the TiO_6 and M1 octahedra form ribbons along the c-axis.

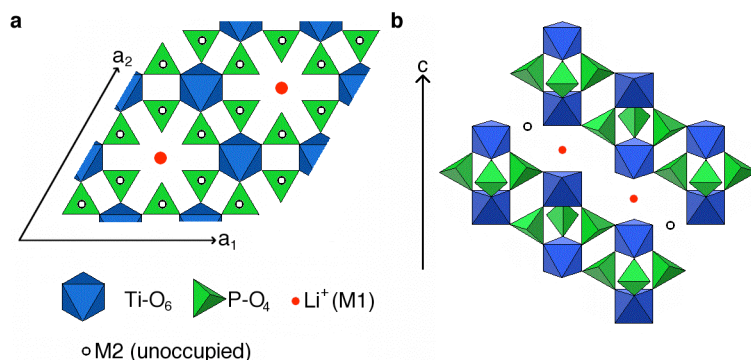
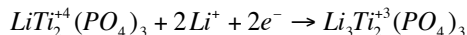


Figure 9: **a)** The basal plane of $\text{LiTi}_2(\text{PO}_4)_3$, showing the occupied M1 sites and the unoccupied M2 sites above and below the plane. **b)** View of the $\text{LiTi}_2(\text{PO}_4)_3$ structure, parallel to the c-axis. The M2 sites form layers that share the basal planes of the M1 octahedra. Insertion of Li^+ into the structure results in full occupancy of the M2 sites by Li^+ .

Insertion of additional lithium ions proceeds by a two-phase reaction in which a reduced phase containing Ti^{+3} is formed:⁸⁵



The inserted lithium ions fully occupy a crystallographically distinct, octahedrally coordinated M2 site.⁸⁵ The M2 sites form close packed layers in the basal planes of the M1 sites. In other NASICON materials, the alkali cations initially present may occupy a combination of M1 and M2 sites, or may be randomly distributed with partial occupancy amongst only the M2 sites.⁸⁴⁻⁸⁵ In those cases, single-phase insertion reactions may be observed. Partial occupancy of the M2 sites can also be observed if Al^{+3} is substituted for some of the Ti^{+4} , resulting in materials of the form $\text{Li}_{1+x}\text{Al}_x\text{Ti}_{2-x}(\text{PO}_4)_3$, which have extremely high Li^+ conductivity and which can be used as solid electrolytes.⁸⁷⁻⁸⁸

Lithium titanium phosphate has a low reaction potential of -0.5 V vs. S.H.E., as first shown by Delmas et al in 1988.⁸⁵ Because of the two-phase nature of its intercalation of Li^+ , $\text{LiTi}_2(\text{PO}_4)_3$ has a flat reaction potential profile. For the insertion of two Li^+ per formula unit, the specific capacity of $\text{LiTi}_2(\text{PO}_4)_3$ is 138.8 mAh/g. In addition, it has high lithium ion conductivity and is insoluble in pH-neutral aqueous solutions, making attractive for use as an anode in aqueous batteries.

Nearly two decades after the initial discovery of its 2.5 V reaction potential, $\text{LiTi}_2(\text{PO}_4)_3$ was indeed studied as an anode in aqueous lithium ion batteries. In 2007, Wang et al demonstrated that both $\text{LiTi}_2(\text{PO}_4)_3$ and a related titanium pyrophosphate phase (TiP_2O_7) could be used as an anode in cells that contained a LiMn_2O_4 cathode and a 5 M LiNO_3 electrolyte.⁵² Unfortunately, the presence of air in their cells led to a low coulomb efficiency at the anode, as oxygen was reduced along with the reduction of $\text{LiTi}_2(\text{PO}_4)_3$. This resulted in destructive overcharging of the LiMn_2O_4 cathode and rapid capacity loss: after 25 cycles, only about one third of the cells' initial capacity remained.

Later in 2007, Luo and Xia also described aqueous cells containing a $\text{LiTi}_2(\text{PO}_4)_3$ anode and a LiMn_2O_4 cathode.⁵³ In their study, they addressed the poor electronic conductivity of $\text{LiTi}_2(\text{PO}_4)_3$ by coating the material with a conformal coating of conductive carbon. Transmission electron microscopy (TEM) found that the carbon coating was several tens of nanometers thick. This relatively thick coating accounted for 12% of the electrode mass. The result was much more stable cycling, as 80% of the initial discharge capacity of the full cell was retained after 200 deep discharge cycles at a current rate of about 7C.

Later, in 2009, Liu et al showed that $\text{LiTi}_2(\text{PO}_4)_3$ could also be combined with LiFePO_4 to make a 1 V cell.⁵⁴ Its cycle life was limited, however; 75% of its initial capacity was retained after 50 cycles. The authors alleged that electrolyte decomposition was not the cause in the loss of cycle life, but did not propose another explanation. There is some evidence that LiFePO_4 itself is water-soluble, and this effect can be exacerbated at the mildly acidic pH of the 2 M Li_2SO_4 electrolyte used in this study.⁸⁹

Cells using a $\text{LiTi}_2(\text{PO}_4)_3$ anode and a LiFePO_4 cathode that had extremely long cycle life were demonstrated in 2010 by Luo, Xia, and colleagues.²⁷ In this study, the deleterious activity of oxygen reduction at the anode was described in detail. After removing oxygen from the cell, 90% of the initial discharge capacity was retained after 1,000 cycles at a 6C rate. The use of a more basic pH of 13 also lowered the potential for hydrogen evolution to -0.75 V vs. S.H.E., allowing the $\text{LiTi}_2(\text{PO}_4)_3$ anode to cycle without side reactions involving either oxygen or water.

6.2 Synthesis and Carbon-Coated Lithium Titanium Phosphate Nanoparticles

In the work performed for this thesis, a method for the synthesis of carbon-coated, nanoparticulate $\text{LiTi}_2(\text{PO}_4)_3$ was developed to overcome the poor electronic conductivity of this material.⁹¹⁻⁹² Nanoparticulate $\text{LiTi}_2(\text{PO}_4)_3$ was synthesized using a Pechini sol-gel method, similar to one previously documented by Mariappan et al.⁹⁰ About 3 g of titanium isopropoxide (Sigma Aldrich) was added to a solution containing 40 mL 30% hydrogen peroxide and 15 mL 30% ammonium hydroxide under vigorous stirring. Rapid ligand exchange results in the formation of titanium hydroxy complexes, which are easily identified by their bright yellow color. After stirring for 20 minutes, citric acid was added in a 2:1 molar ratio with respect to titanium. After stirring for another 20 minutes, lithium carbonate, dissolved in 10 mL of concentrated nitric acid, and in a 1:2 molar ratio with respect to titanium, was added. Immediately following the addition of the lithium carbonate solution, a stoichiometric amount (3:2 with respect to titanium) of ammonium phosphate monobasic in 10 mL water was added. The addition of the acidic lithium precursor resulted in a bright orange solution, as some of nitric acid decomposed to nitrogen dioxide. After stirring for a further 20 minutes, ethylene glycol was added in a 2:1 molar ratio with respect to titanium to act as a chelating agent with the citric acid.

The temperature was then raised to 80° C and held for two hours, while stirring continued, allowing volatiles and water time to evaporate. Then the temperature was raised to 140° C over a one hour ramp, and held for 20 minutes. The 140° C heating step allowed the ethylene glycol and citric acid to polymerize, resulting in a viscous, foamy brown gel. This product was heated in air at 300° C for two hours to burn off excess organic matter, ground by hand, and then sintered at 800° C for four hours in air. The bright white product was ground for one hour using a high impact ball mill, resulting in a fine white powder. X-ray diffraction (XRD) found that the $\text{LiTi}_2(\text{PO}_4)_3$ product was virtually phase-pure, though in some cases a small minority phase of titanium pyrophosphate (TiP_2O_7) was also observed. The addition of a slight excess of lithium carbonate during synthesis was found to alleviate the formation of TiP_2O_7 .

Pure $\text{LiTi}_2(\text{PO}_4)_3$ is an electronic insulator that can be electrochemically cycled only after further treatment. To aid electronic transfer to the $\text{LiTi}_2(\text{PO}_4)_3$ nanoparticles, a carbon coating treatment developed by Dr. Fabio La Mantia was performed. First, a polymer solution to be used as a precursor to the carbon coating was prepared. One and a half grams of glucose were added to 5 mL water and 30 mL ethylene glycol while stirring in a nitrogen atmosphere. This solution was heated to 100° C and held at that temperature for 20 minutes. Then 4 mL of 30% ammonium hydroxide was added to facilitate polymerization of the glucose. After another 20 minutes, the temperature was raised to 180° C and held for eight hours. The product was a viscous, dark brown liquid. Between 0.4 and 0.5 g of $\text{LiTi}_2(\text{PO}_4)_3$ was added to 15 mL of the carbon coating precursor solution and then repeatedly sonicated and stirred by hand. Vacuum filtration was performed to remove the polymer-coated powder, and the carbon coating precursor solution was refluxed. The product was then dried at 100° C under vacuum for one hour. Finally, the polymer-coated powder was placed in a ceramic boat and heated to 800° C in a tube furnace in a N_2

atmosphere. The heating ramp was eight hours long, and the final temperature was held for an additional eight hours. Another ceramic boat containing carbon black was placed upstream of the sample to prevent combustion of the polymer coating of the $\text{LiTi}_2(\text{PO}_4)_3$. After this carbonization treatment, the carbon coated $\text{LiTi}_2(\text{PO}_4)_3$ was black. It was ground by hand before use in electrodes.

Slurries of the fresh and carbon-coated $\text{LiTi}_2(\text{PO}_4)_3$ were prepared by grinding the active material by hand with amorphous carbon (Timcal Super P Li), PVDF (Kynar HSV 900), and graphite (Timcal KS6) in a 73:15:10:2 ratio before adding NMP. This slurry was stirred for several hours and then deposited on stainless steel foil or mesh. These electrodes were dried in air at 100°C for one hour. Preliminary electrochemical characterization of the fresh and carbon-coated $\text{LiTi}_2(\text{PO}_4)_3$ was performed using two-electrode pouch cells that contained excess lithium foil as a reference and counter electrode, a polymer separator, and an electrolyte of 1 M lithium hexafluorophosphate (LiPF_6) salt in a 1:1 EC:DEC solvent.

6.3 Physical Characterization of Lithium Titanium Phosphate

X-ray diffraction (XRD) and scanning electron microscopy (SEM) were used to characterize the crystallinity and morphology, respectively, of the $\text{LiTi}_2(\text{PO}_4)_3$ powder. The fully indexed XRD spectrum (Fig. 10a) shows that the $\text{LiTi}_2(\text{PO}_4)_3$ was phase pure. In some instances, a small minority phase of TiP_2O_7 was detected by its 600 diffraction peak at 22.55° in 2θ ($d_{600} = 3.94\text{ \AA}$). This impurity was due to the loss of Li_2O from the material during high temperature annealing, as has been reported previously. The presence of the TiP_2O_7 minority phase could be limited by adding a small excess of lithium during the synthesis.

The secondary electron SEM image of ball-milled $\text{LiTi}_2(\text{PO}_4)_3$ shows polydisperse particles of 100-300 nm. In spite of the good crystallinity observed by XRD, the particles were not faceted. This morphology is advantageous because, Li^+ and electrons can rapidly access the entire volume of the particle. The end result is greater capacity retention at high cycling rates.

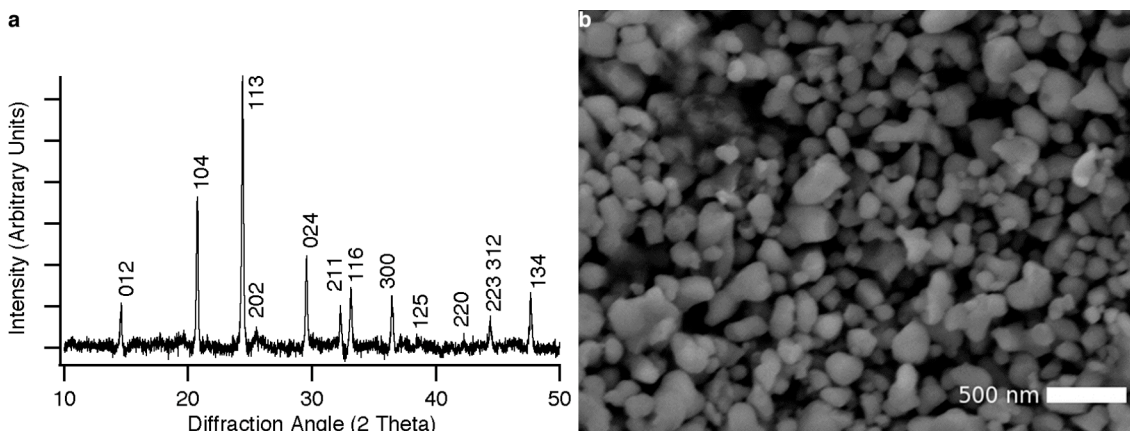


Figure 10: a) Powder XRD of freshly synthesized $\text{LiTi}_2(\text{PO}_4)_3$ powder reveals a phase pure material. In some samples, a small minority phase of TiP_2O_7 was detected by its 600 diffraction peak at 22.55° 2θ (not shown here). b) After high impact ball milling of $\text{LiTi}_2(\text{PO}_4)_3$, SEM revealed nanoparticles of 100-300 nm

Transmission electron microscopy (TEM) was performed on the carbon coated $\text{LiTi}_2(\text{PO}_4)_3$. A conformal coating about 5 nm thick was observed (Fig. 11a). The purpose of this carbon coating was to ensure that the individual $\text{LiTi}_2(\text{PO}_4)_3$ nanoparticles were in good electrical contact with the rest of the electrode. This was confirmed to be the case: galvanostatic cycling of carbon-coated and uncoated $\text{LiTi}_2(\text{PO}_4)_3$ at a 1C rate in cells containing organic electrolyte and a lithium counter electrode showed that only the carbon-coated material was electrochemically active (Fig. 11b). A specific capacity of over 110 mAh/g was observed for carbon-coated material, while almost no capacity was observed for uncoated $\text{LiTi}_2(\text{PO}_4)_3$. For these measurements, the same synthesis batch of $\text{LiTi}_2(\text{PO}_4)_3$ was used in both cells, and the samples differed only by the presence or absence of the carbon coating. The need for carbon coating of $\text{LiTi}_2(\text{PO}_4)_3$ to overcome its poor electronic conductivity has also been observed by other research groups.

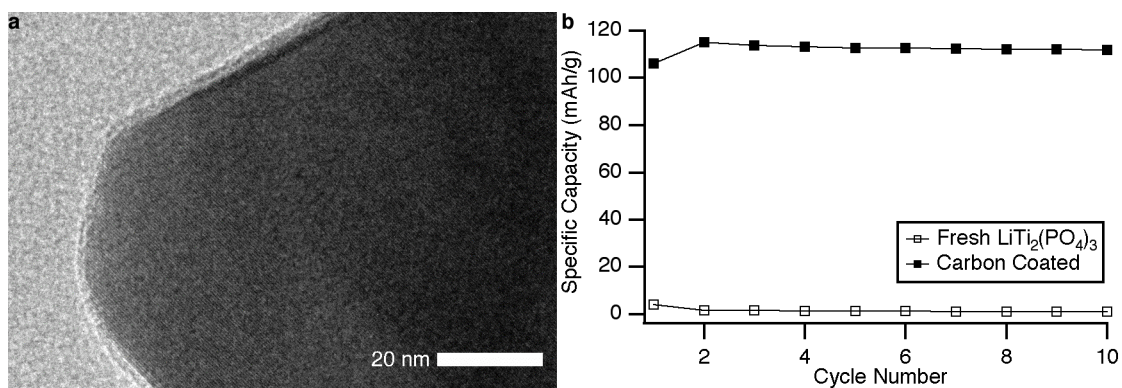


Figure 11: **a)** TEM of carbon coated $\text{LiTi}_2(\text{PO}_4)_3$ shows a 2-3 nm thick amorphous layer on the surface of the nanoparticles. **b)** Galvanostatic cycling of electrodes containing fresh and carbon coated $\text{LiTi}_2(\text{PO}_4)_3$ shows that substantial capacity can only be achieved with carbon coating.

6.4 Electrochemical Characterization of Lithium Titanium Phosphate

Electrochemical characterization of the carbon-coated $\text{LiTi}_2(\text{PO}_4)_3$ electrodes by cyclic voltammetry and galvanostatic cycling was performed on both organic and aqueous cells. The aqueous cells contained a $\text{LiTi}_2(\text{PO}_4)_3$ working electrode, a partially oxidized $\text{LiFePO}_4/\text{FePO}_4$ reference electrode, a partially charged $\text{Li}_{1-x}\text{Mn}_2\text{O}_4$ counter electrode, and a 2 M Li_2SO_4 (pH=8-9) electrolyte. The methods for preparing the reference and counter electrodes were described in Chapters 5.1 and 4.2, respectively. Three-electrode pouch cells were prepared as described in Chapter 5.2. In these cells, the slurry electrodes of $\text{LiTi}_2(\text{PO}_4)_3$, LiFePO_4 and LiMn_2O_4 were prepared on stainless steel mesh to increase the mass loading.

Cyclic voltammetry of $\text{LiTi}_2(\text{PO}_4)_3$ electrodes at a slow 0.1 mV/s scan rate found reversible activity at 2.5 V vs. Li^+/Li , or -0.5 V vs. S.H.E. in both organic and aqueous electrolytes (Fig. 12a). A sharp reaction was observed for reduction of $\text{LiTi}_2(\text{PO}_4)_3$ to $\text{Li}_3\text{Ti}_2(\text{PO}_4)_3$ in both electrolytes. However, oxidation of $\text{LiTi}_2(\text{PO}_4)_3$ occurs much more slowly in the aqueous electrolyte than in the organic one. The mechanism responsible for this effect is unknown. A small peak observed during reduction at 2.6 V corresponds to the small minority phase of TiP_2O_7 , which is known to be electrochemically active at 2.6-2.7 V.

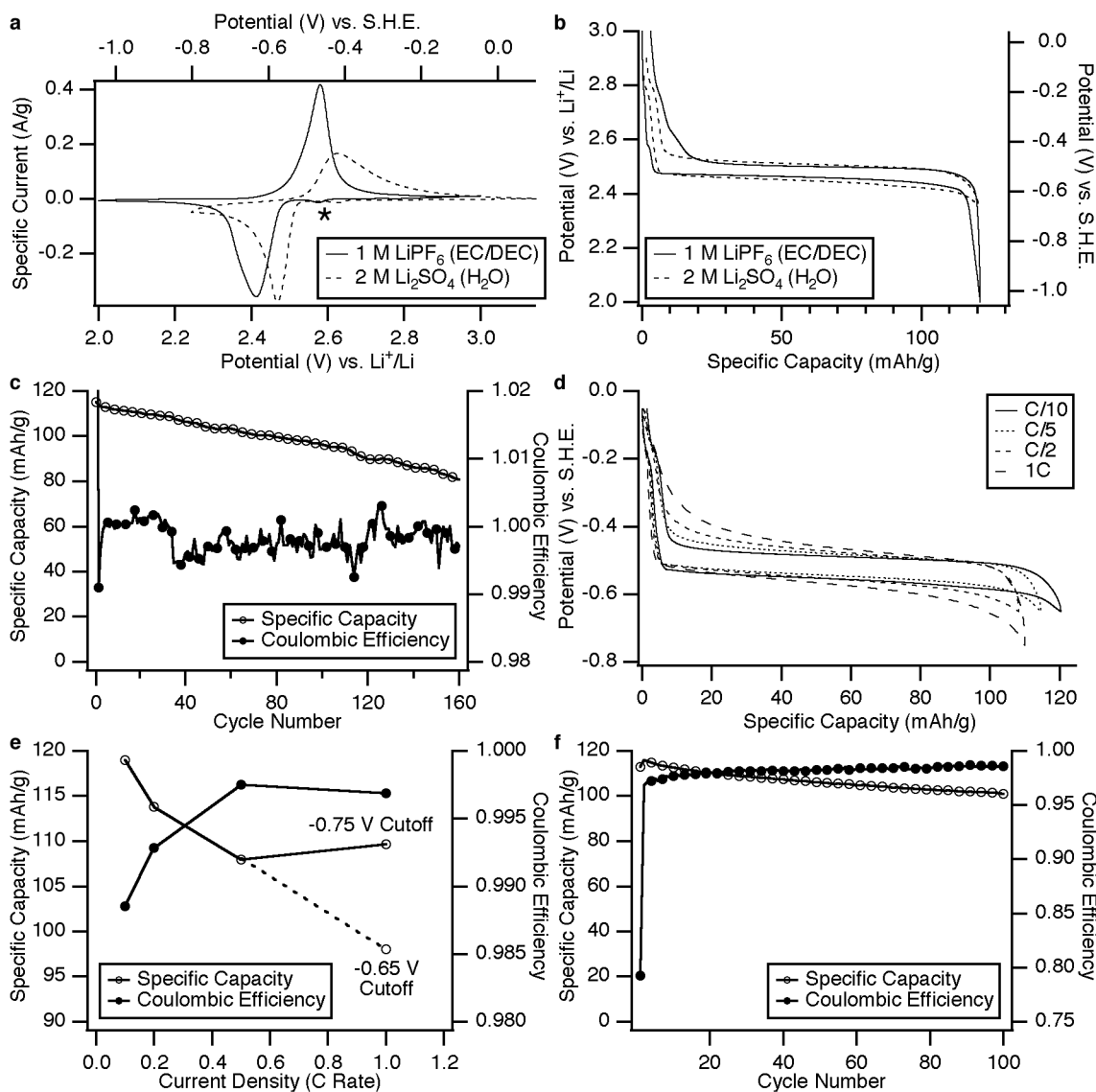


Figure 12: **a)** Cyclic voltammety of $\text{LiTi}_2(\text{PO}_4)_3$ in organic and aqueous electrolytes. **b)** The potential profiles of $\text{LiTi}_2(\text{PO}_4)_3$ during galvanostatic cycling at a C/10 rate in organic and aqueous electrolytes. **c)** Long-term cycling of $\text{LiTi}_2(\text{PO}_4)_3$ at a 1C rate in organic electrolyte. **d)** The potential profiles of $\text{LiTi}_2(\text{PO}_4)_3$ in aqueous electrolyte at various current densities. **e)** The specific capacity and coulombic efficiency of $\text{LiTi}_2(\text{PO}_4)_3$ during galvanostatic cycling in aqueous electrolyte at various rates. **f)** The specific capacity and coulombic efficiency of $\text{LiTi}_2(\text{PO}_4)_3$ during extended cycling at a C/5 rate in aqueous electrolyte.

The electrochemical behavior of $\text{LiTi}_2(\text{PO}_4)_3$ in the organic and aqueous electrolytes was also compared using galvanostatic cycling at a C/10 rate (Fig. 12b). Specific capacities of about 120 mAh/g were observed in both electrolytes. Some samples achieved over 132 mAh/g, close to the 138.8 mAh/g theoretical specific capacity of $\text{LiTi}_2(\text{PO}_4)_3$ (not shown). However, due to some variation in the synthesis of

$\text{LiTi}_2(\text{PO}_4)_3$ and the effectiveness of the carbon coating, observation of specific discharge capacities substantially greater than 120 mAh/g was inconsistent. A flat reaction plateau at 2.5 V was observed, which corroborated previous studies. The constant potential over a large composition range indicates that lithium ion insertion results in a two-phase system, with stoichiometric $\text{LiTi}_2(\text{PO}_4)_3$ and $\text{Li}_3\text{Ti}_2(\text{PO}_4)_3$ present at intermediate charge states. The lower potential cutoff during cycling was 2.0 V vs. Li^+/Li in the organic electrolyte, but was 2.4 V vs. Li^+/Li , or -0.65 V vs. S.H.E. during cycling in the aqueous electrolyte. The higher potential cutoff in the aqueous electrolyte was chosen in an effort to avoid excessive H_2 generation at especially low potentials.

Extended cycling of $\text{LiTi}_2(\text{PO}_4)_3$ was performed in organic electrolyte cells. At a 1C rate, an initial discharge capacity of 118 mAh/g was observed, of which 84% was retained after 100 cycles, and of which 70% was retained after 160 cycles (Fig. 12c). During cycling in the organic electrolyte, the coulomb efficiency was above 99.5%. The NASICON framework structure of $\text{LiTi}_2(\text{PO}_4)_3$ suffers only small distortions during reduction, so it is unlikely that damage to the structure during cycling causes the slow capacity loss. Instability of the carbon coating on the particle surfaces could result in capacity loss, as the carbon coating must be present to facilitate electron transport during electrochemical cycling.

The rate capability of $\text{LiTi}_2(\text{PO}_4)_3$ was studied in aqueous 2 M Li_2SO_4 . A maximum specific discharge capacity of 120 mAh/g was observed at a C/10 rate between -0.65 and -0.05 V vs. S.H.E. (Fig. 12d-e), most of which was retained at faster cycling rates of C/5 and C/2. Extending the lower potential cutoff to -0.75 V from -0.65 V vs. S.H.E. resulted in an increase in specific capacity from 96 mAh/g to 110 mAh/g, but at a cost of a marginal decrease in coulombic efficiency. At the -0.65 V cutoff, coulombic efficiencies of up to 99.7% were achieved, showing that restricting the lower cutoff could successfully minimize side reactions, including hydrogen reduction. The poor electronic conductivity and high mass loading ($10\text{-}15$ mg/cm^2) of $\text{LiTi}_2(\text{PO}_4)_3$ limited the high-rate cycling performance.

Long-term cycling of $\text{LiTi}_2(\text{PO}_4)_3$ was also performed in aqueous cells. At a C/5 rate, an initial discharge capacity of 113 mAh/g was observed, 89% of which was retained after 100 cycles (Fig. 12f). After the first cycle, during which some residual O_2 in the electrolyte was reduced to H_2O , the coulombic efficiency was over 98.5%. As in the case of extended cycling of organic electrolyte cells, the mechanism for the capacity loss of the $\text{LiTi}_2(\text{PO}_4)_3$ electrode is not well understood, though instability of the carbon coating is one possibility. At the time of these measurements, no research group had ever reported such long cycle life for an anode in an aqueous lithium ion battery. Later, it was shown that $\text{LiTi}_2(\text{PO}_4)_3$ could last up to 1,000 cycles in aqueous two-electrode coin cells using a LiFePO_4 cathode.²⁷

6.5 Final Comments on Aqueous Lithium Ion Batteries

The safety and low cost of aqueous electrolytes make aqueous batteries inherently attractive, yet relatively little attention has been paid to aqueous lithium ion batteries since their invention nearly two decades ago. The immense portable electronics market has driven most of the battery research community to study organic electrolyte devices with high voltages and specific energy. The limited stability range of

water prevents aqueous devices from ever achieving the high (150 Wh/kg) specific energy of organic electrolyte lithium ion batteries, so they are not practical for portable applications. But more recently, a larger portion of the battery research community has turned its attention to stationary storage applications including the electrical grid. Stationary storage does not require an especially high specific energy, and aqueous lithium ion batteries could satisfy this application. However, their future development and commercialization faces the major challenges of the limited electrochemical stability range of the electrolytes and the small number of lithium ion electrodes with suitable reaction potentials.

The biggest challenge to commercialization of aqueous lithium ion batteries is the lack of a suitable anode. The vanadate anodes used in the early studies are partially soluble, but no work on protective surface modifications or other stabilizing processes has yet been reported. The -0.5 V vs. S.H.E. reaction potential of the $\text{LiTi}_2(\text{PO}_4)_3$ anode studied here is too low, the data reported here never showed coulombic efficiency above 99.7% (and that only at high rates) because of hydrogen evolution. Increasing the pH of the electrolyte could mitigate this problem, though the LiMn_2O_4 and LiCoO_2 cathodes may have reaction potentials too high for operation in a basic solution. Another recently reported anode, polypyrrole (PPy), has an attractive reaction potential near S.H.E., but its low electronic conductivity resulted in poor performance. Future adoption of lithium ion electrode materials with reaction potentials just below S.H.E., such as $\text{LiFe}_2(\text{PO}_4)_3$ and $\text{Li}_2\text{FeSiO}_4$, may also result in an anode that is compatible with aqueous electrolytes and has sufficient cycle life and efficiency to be used in practical cells.

The most desirable property of aqueous batteries- a nonflammable, inexpensive, highly conductive electrolyte- is not predicated upon electrodes relying on any particular insertion ion. While the study of aqueous lithium ion batteries may be convenient due to prior knowledge of electrode properties in organic electrolytes, many other electrode families have also been studied in water. Aqueous sodium ion batteries have recently been commercialized in spite of the dearth of sodium cells using organic electrolytes. In Part 3 of this thesis, the recent adoption of Prussian Blue analogues from electrochromic devices to batteries is described in detail. Given the limited number of lithium ion electrodes compatible with aqueous electrolytes, it is appropriate and necessary that other materials systems are also examined.

Chapter 7: Introduction to Prussian Blue

7.1: The Impetus for Developing Prussian Blue Batteries

As discussed in the introductory chapter, new energy storage technology with very long cycle life, high power and efficiency, and low cost is needed for stationary storage applications including those related to the electrical grid. Ferric ferrocyanide, which is commonly known as Prussian Blue, has been studied as an electrode in electrochromic devices with aqueous electrolytes. In some cases, Prussian Blue electrodes were found to be extremely durable, lasting 10^5 - 10^7 deep discharge cycles.^{70, 93-94} This truly remarkable stability, which is observed in inexpensive aqueous electrolytes, suggests that Prussian Blue could operate as a high performance battery electrode. Well before the conclusion of the study of $\text{LiTi}_2(\text{PO}_4)_3$ (Chapter 6), the limitations of those batteries had already become apparent. With the hope of developing an electrode with longer cycle life and faster rate capability, in January 2010, Professor Robert A. Huggins proposed that Prussian Blue be examined as a possible battery electrode. The work that followed, discussed below (Chapters 8-15), found that a large family of materials with the same crystal structure as Prussian Blue could indeed be used as electrodes in aqueous batteries.

This chapter provides background and historical context for the work performed for this thesis. In a few instances, data collected during this thesis are used in this chapter while explaining general concepts about Prussian Blue analogues. Chapters 8-15 describe the work done for this thesis in detail.

7.2: The History of Prussian Blue

Knowledge of Prussian Blue predates its scientific study by nearly two centuries. Sometime between 1704 and 1706, Deisbach, a German painter, was the first to synthesize Prussian Blue, possibly during a collaboration with Johann Conrad Dippel, a noted alchemist.⁹⁵ Deisbach combined potassium carbonate, animal oil, iron sulfate, and cochineal, and though he expected to produce a red pigment (cochineal red lake), he obtained a different reaction product: “quanto magis hoc procedit, tanto magis purpureum colorem, in caeruleum, imo tandem profunde cyaneum,” which roughly translated reads, “as this proceeds, the more purple the color, into the blue, and yea, at length deep blue.”⁹⁵

Prussian Blue cost much less than ultramarine, which was the most common blue pigment at that time, and which was mined principally in Afghanistan, so by 1709 painters were using Prussian Blue throughout Europe.⁹⁶⁻⁹⁷ Its use as a pigment and dyestuff would continue into the 20th century. In 1752, the French chemist Pierre Macquer found that Prussian Blue could be decomposed into hydrogen cyanide and an iron salt, suggesting that it was predominantly an iron cyanide.⁹⁸

By the middle of the 19th century, Prussian Blue and many other metal ferrocyanides had been synthesized by chemical precipitation. At that time, Prussian Blue was synthesized on industrial scales from salts of Fe^{3+} and $\text{Fe}^{\text{II}}(\text{CN})_6^{4-}$. Early chemists believed that syntheses using salts of Fe^{2+} and $\text{Fe}^{\text{III}}(\text{CN})_6^{3-}$ resulted in a different material, which they named Turnbull's Blue.⁹⁹⁻¹⁰⁰ However, Watts articulated the

illogic of this belief in 1879:

“One the one hand, ferrous salts exert a reducing action on potassium ferricyanide, and that, on the other hand, ferric salts exert an oxidizing action on the ferrocyanide... There is therefore no ground for assuming that the iron-atoms in Turnbull’s and in Prussian blue are in different states...” (Ref. 100)

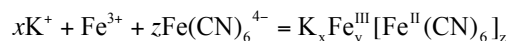
Controversy over whether Prussian Blue was the ferric salt of ferrocyanide ($\text{Fe}_x^{\text{III}}[\text{Fe}^{\text{II}}(\text{CN})_6]_y$), or the ferrous salt of ferricyanide ($\text{Fe}_x^{\text{II}}[\text{Fe}^{\text{III}}(\text{CN})_6]_y$) continued into the 1960s. In 1962, Robin measured the optical properties and electronic structure of both Prussian Blue and Turnbull’s Blue, finding that all mixed-valence iron cyanides were ferric ferrocyanide.¹⁰¹⁻¹⁰² Irrefutable evidence that this is the correct mixed valence state was obtained by Fluck, et al in 1963 using Mössbauer spectroscopy, which is sensitive to the valence, spin state, and bonding environment of iron cations.

Industrial and scientific interest in Prussian Blue and analogous materials with the same crystal structure grew during the 20th century. By 1939, annual production of Prussian Blue for use as a dyestuff reached nearly 10^7 kg in the United States.¹⁰⁴ In 1936, Keggin and Miles performed the first characterization of the crystal structure of Prussian Blue using X-ray diffraction, and soon afterwards, some related materials were found to have the same structure.¹⁰⁵⁻¹⁰⁷ As early as the 1950s, the ability of some Prussian Blue analogues to act as selective ion membranes and as selective adsorbers of toxic ions such as Cs was studied.¹⁰⁸⁻¹¹⁰ Some of the modern literature on the use of Prussian Blue for these applications appears to repeat early work that was done in Soviet Russia, much of which is no longer readily available.¹¹¹⁻¹¹⁶ Until the late 1970s, most of the scientific study of Prussian Blue and its analogues was related to their synthesis, structure, and physical properties.^{105-107, 117-133}

Modern interest in the electrochemistry of Prussian Blue began in 1978, when Vernon Neff demonstrated that Prussian Blue electrodes could be reversibly reduced to form Everitt’s Salt.³⁵ The remarkable change in color from deep blue to colorless during this reaction catalyzed widespread interest in using Prussian Blue in electrochromic devices.^{70, 93-94, 138-149} Just one year later, in 1979, a French research group studied Prussian Blue analogues for use as cathodes in organic lithium ion cells.³⁶⁻³⁷ That work went largely unnoticed, and Neff is generally credited for demonstrating the first Prussian Blue battery in 1985.³⁸ In that work and in a few subsequent studies, batteries using electrodeposited thin film electrodes of Prussian Blue were shown to have modest cycle life, but their limited performance failed to attract widespread attention of the research community.³⁹⁻⁴⁶ It was not until 2011 that during work for this thesis, batteries using bulk quantities of Prussian Blue analogues for electrodes were finally demonstrated (Chapter 8-15).¹⁵⁰⁻¹⁵⁴

7.3: General Synthesis Methods for Prussian Blue and its Analogues

The synthesis of Prussian Blue and analogous materials that have the same crystal structure is performed, with few exceptions, by either bulk chemical precipitation or electrodeposition. In the former case, spontaneous chemical precipitation of Prussian Blue from a ferric salt such as FeCl_3 and a ferrocyanide salt such as $\text{K}_4\text{Fe}(\text{CN})_6$ proceeds by the following reaction:



This reaction may be generalized for a large family of materials with the same crystal structure as Prussian Blue.^{99-102, 120-122, 124-130, 136-137} The general synthesis for a Prussian Blue analogue may be described by the following expression:



Here, A^+ is an alkali cation such as K^+ or Na^+ , or another small cation such as NH_4^+ , P^{m+} is a cation of a transition metal such as Mn, Fe, Co, Ni, Cu, or Ni, and $\text{R}(\text{CN})_6^{n-}$ is a hexacyanometalate anion of Fe, Mn, Co, Cr, Pt, Ir, or Ru. The choice of $\text{R}(\text{CN})_6$ is limited by the relatively small number of chemically stable hexacyanometalates,¹⁵⁶ but Prussian Blue analogues containing dozens of different transition metal and alkaline earth metals as the P site cation have been synthesized.^{126, 133, 157-162} The A:P:R(CN)₆ stoichiometry, which may be written as $x:y:z$ in this case, depends on the synthesis conditions, but must be chosen to fulfill charge neutrality of the formula, and thus, it depends on the charge ratio $m:n$ and on the concentration of A^+ in the structure. The details of how the stoichiometry of A:P:R(CN)₆ affects the structure of the material are discussed below (Chapter 7.4). The precursors for the chemical precipitation of Prussian Blue analogues are typically prepared in aqueous solutions with concentrations between 0.01 and 0.1 M.^{126, 136} The metal salt solution is added to the hexacyanometalate solution, or the opposite may be done. In rare cases, both precursor solutions have been combined in a constant ratio by simultaneous addition to a third solution (typically water). Extensive reviews of the synthesis of copper hexacyanoferrate (CuHCF) have found correlations between synthesis conditions and the structure factor of the product,¹⁶³⁻¹⁶⁴ but in general, a complete chemical analysis must be performed to find the true composition of Prussian Blue analogues.

The other synthesis method, electrodeposition, was employed by electrochemists throughout the 1980s during the peak of interest in Prussian Blue's electrochromic properties.^{138-145, 161} Many Prussian Blue analogues are somewhat soluble when the hexacyanoferrate group is fully oxidized. This allows preparation of dilute, stable solutions of an alkali ferricyanide (for example, $\text{K}_3\text{Fe}(\text{CN})_6$) and a transition metal salt. To avoid rapid, spontaneous precipitation of the product, these electrodeposition solutions have salt concentrations of about 1 mM or less. The application of a negative potential to an electrode results in the reduction of ferricyanide to ferrocyanide, and a subsequent rapid reaction of ferrocyanide with the transition metal salt. The result is a Prussian Blue analogue thin film. The thickness of these films depends on the duration of the deposition, but is typically 300 nm or less.¹⁴⁵ These thin film samples therefore have mass loadings of about 1 $\mu\text{g}/\text{cm}^2$.

The rapid kinetics for alkali ion transport in the Prussian Blue structure during electrochemical cycling allows these electrodeposited thin films to be fully oxidized or reduced in one second or less.^{70, 93-94} In

addition, the absorption of many Prussian Blue analogues dramatically changes when the oxidation state is changed.^{35, 93-94, 136, 142, 144-147, 154} Together, these properties make electrodeposited thin films of Prussian Blue analogues useful in electrochromic devices.

In contrast, batteries require macroscopic electrodes of relatively large mass, so the bulk precipitation method is more useful when preparing Prussian Blue analogues for use in batteries. Chapter 8 contains a detailed discussion of the co-precipitation synthesis method used in this thesis for production of the CuHCF and nickel hexacyanoferrate (NiHCF) battery electrode materials characterized in this work.

7.4: The Crystal Structure of Prussian Blue and its Analogues

The crystal structure of Prussian Blue was examined for the first time in 1934 by Keggin and Miles.¹⁰⁵ Using powder X-ray diffraction, they correctly determined that the octahedral $\text{Fe}^{\text{II}}(\text{CN})_6^{4-}$ and Fe^{3+} formed a face centered cubic (FCC) lattice, in which the Fe^{3+} is six-fold coordinated to the nitrogen ends of the cyanide ligands. This forms an open framework that contains large interstices at the centers of the eight subcells of the FCC unit cell (Fig. 13).^{105-107, 120-122, 126, 133, 136-137} Typical lattice parameters for hexacyanoferrate-based Prussian Blue analogues are between 10 and 10.3 Å, though those containing hexacyanochromate, hexacyanomanganate, or hexacyanoiridate may have lattice parameters of 10.6 Å or more. The interstitial “A sites” may contain zeolitic water or hydrated alkali cations.¹³⁶⁻¹³⁷ In many cases, the framework is not altered by partial or complete replacement of the nitrogen-coordinated Fe^{3+} with another transition metal cation, or by the replacement of $\text{Fe}^{\text{II}}(\text{CN})_6^{4-}$ with another hexacyanometalate.¹⁶⁶⁻¹⁶⁹ Thus, a wide variety of Prussian Blue analogues with the same crystal structure have been identified.

These Prussian Blue analogues may be described by the following chemical formula: $\text{A}_x\text{P}_y[\text{R}(\text{CN})_6]_z \cdot n\text{H}_2\text{O}$, where the species that may occupy the A, P, and $\text{R}(\text{CN})_6$ sites are as discussed in Chapter 7.2. Partial replacement of the cyanide ligands with others such as carbonyl or nitrosyl is also possible, though not well documented.^{156, 163, 170} The structure typically contains 3-4 zeolitic H_2O for each chemical formula unit, which results in up to 16 H_2O in each unit cell.¹³⁶⁻¹³⁷

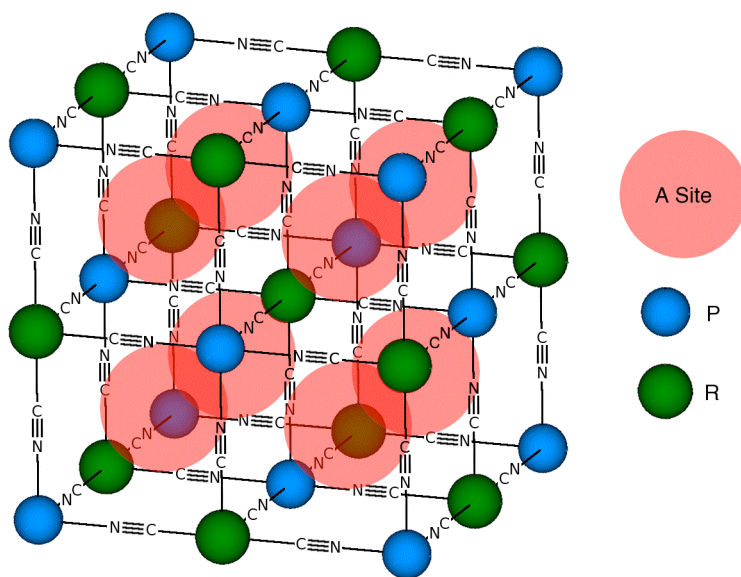


Figure 13: The unit cell of Prussian Blue. Octahedrally coordinated hexacyanometalates $[\text{R}(\text{CN})_6^{n-}]$ are linked in a FCC lattice with six-fold nitrogen coordinated P^{m+} transition metals. Each unit cell contains eight cubic subcells. The subcells have large interstices at their centers known as the A sites. The occupancy of the A sites may vary between zero and two per formula unit of $\text{A}_x\text{P}(\text{R}(\text{CN})_6)$, or equivalently, between zero and eight per unit cell. During electrochemical cycling, alkali cations are inserted and removed from the A sites.

Using a hard sphere model and tabulated values for the crystal ionic radii of transition metals, carbon, and nitrogen, and their known coordinates in the unit cell, the hard sphere radius of the A sites and the channels between them can be readily calculated. As shown in Fig. 14, for Prussian Blue itself, the radius of the A site is about 2.51 Å, while the radius of the channel between adjacent A sites through the {200}-type planes is 1.58 Å. Other Prussian Blue analogues containing hexacyanoferrate have crystal structures that are within 1% of that of Prussian Blue, so their A site and channel radii are similar in size.

In comparison, the crystal ionic radii of K^+ , the most common intercalant during electrochemical cycling of Prussian Blue analogues, is 1.52 Å.⁶⁴ Another common intercalant, Na^+ , has an even smaller crystal ionic radius of 1.12 Å. It is likely that these ions are hydrated when inside the structure, for they are too small to occupy the A sites alone. Intercalants that are too small for an interstitial site typically do not occupy the center of the site, but rather, are attracted to some of the species on the site walls. Therefore, their mobility from one interstitial site to the next is generally low. The rapid electrochemical reactions observed in Prussian Blue analogues indicate that K^+ and Na^+ rapidly move through the framework, so it is likely that they are hydrated when in the A sites.

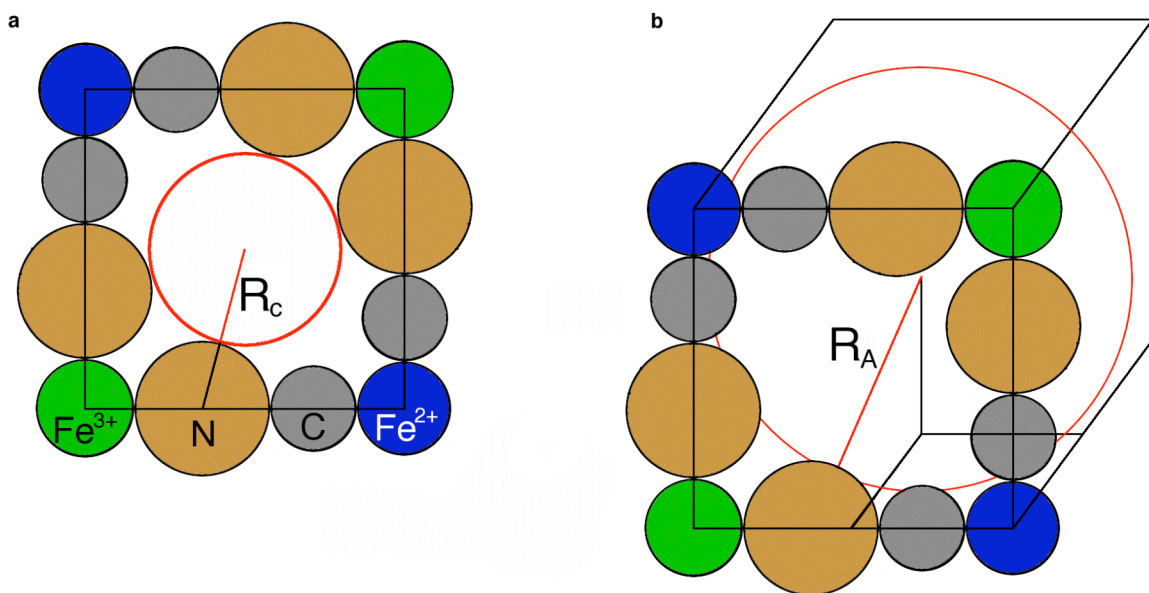


Figure 14: (a) Using a hard sphere model, the minimum radius of a channel between two adjacent A sites (R_c) in the Prussian Blue ($a_0 = 10.16$ Å) structure is 1.58 Å. (b) The minimum radius of the A site (R_A) in Prussian Blue is 2.51 Å.

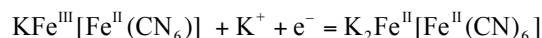
Prussian Blue analogues are typically synthesized from an alkali salt hexacyanometalate salt such as $K_4Fe(CN)_6$. The presence of potassium during synthesis results in its partial occupancy of the interstitial A sites before any electrochemical treatment occurs. In addition, for many Prussian Blue analogues an excess of the P salt precursor is needed for the solid product to form at a reasonable rate. This has led to considerable confusion about the true nature of the Prussian Blue crystal structure. Indeed, well into the

20th century, it was believed that two chemically distinct forms of Prussian Blue existed.^{101-104, 124, 129, 136} The “insoluble” Prussian Blue was believed to have the formula $\text{Fe}_4[\text{Fe}(\text{CN})_6]_3$ (neglecting zeolitic water), while the “soluble” material was believed to have the composition $\text{KFeFe}(\text{CN})_6$. In the former compound, none of the A sites are occupied, while in the later, one half of them are, and the four interstitial K^+ per unit cell occupy the sites such that they form tetrahedral array about the $\text{Fe}(\text{CN})_6^{4-}$ at the center of the unit cell (Fig. 13). The terms “insoluble” and “soluble” do not denote true chemical solubility, but rather, were adopted by pigment manufacturers to describe how a stable colloidal solution could be formed from dry Prussian Blue powder.¹⁰² In fact, most syntheses of Prussian Blue and its analogues result in a material with an intermediate chemical formula: some alkali cations occupy the A sites, there is some excess of the P cation, and together their charges balance the charge of the hexacyanometalate anion.

The complicated general formula of $\text{A}_x\text{P}_y[\text{R}(\text{CN})_6]_z \cdot n\text{H}_2\text{O}$ has resulted in considerable debate by crystallographers about the true nature of the Prussian Blue structure.^{105-107, 120-124, 126, 130-133, 136-137} Any deviation from the stoichiometric $\text{A}^+\text{P}^{(n-1)+}\text{R}(\text{CN})_6^{n-}$ or $\text{P}^{m+}_n[\text{R}(\text{CN})_6^{n-}]_m$ must result in a defective structure in which either interstitial, hydrated P cations partially occupy the A sites, or in which there are some $\text{R}(\text{CN})_6$ vacancies in the framework, or both of these. Keggin and Miles originally posited the former explanation when they first determined the nature of the framework structure.¹⁰⁵ Later studies found some evidence of A site occupancy by transition metal cations.^{127, 129} However, assuming the commonly observed extent of zeolitic hydration, the complete fulfillment of charge neutrality by interstitial transition metal cations results in a density of 2.2 g/cm^3 , 10-20% higher than the commonly observed densities of Prussian Blue analogues.¹³³ Complete Reitveld refinement of Prussian Blue using single crystal XRD and powder neutron diffraction found $\text{Fe}(\text{CN})_6^{4-}$ vacancies in the framework, rather than interstitial Fe^{3+} .¹³⁶⁻¹³⁷ The more recent use of advanced techniques including infrared spectroscopy, magnetic susceptibility measurements, X-ray photoelectron spectroscopy (XPS), extended X-ray absorption fine structure (EXAFS), nuclear magnetic resonance (NMR), and hydrogen gas sorption measurements have confirmed that for many Prussian Blue analogues, charge neutrality is achieved at least in part with $\text{R}(\text{CN})_6^{n-}$ vacancies.¹⁷¹⁻¹⁷⁴ For each vacancy of this type, six neighboring P^{m+} cations lose one nitrogen atom from their coordination shell. Studies using XRD and neutron diffraction, as well as XPS and EXAFS have found that a water molecule will fill the empty site in the coordination shell of the P site cation.^{136-137, 171-172} The presence of this coordinated water helps explain the large hydration (14-16 H_2O per unit) cell observed for many Prussian Blue analogues, as there is insufficient interstitial space for all of the water to be zeolitic. However, measurement of the magnetic susceptibility of cobalt hexacyanocobaltate, and more recently, electrochemical characterization of the nickel/palladium hexacyanoferrate system reported evidence that under certain synthesis conditions, transition metals may occupy the A sites.^{127, 168} Detailed study of the structures of the majority of the common Prussian Blue analogues, let alone the entire family, has not yet occurred. Thus, for most Prussian Blue analogues, including those discussed below for their use in batteries, no claims can yet be made about the true nature of defects in the structure, or under which circumstances (chemical composition, synthesis methods, etc.) a particular type of defect will occur.

7.5: Electrochemical Cycling of Prussian Blue

The vast majority of transition metals may be oxidized to multiple valence states. For instance, metallic Fe^0 may be oxidized first to Fe^{2+} , and then Fe^{3+} . Electrodes in many types of batteries, including lithium ion, lead acid, nickel/metal hydride, and flow batteries all rely on changes in the valence state of one or more transition metal cations during their charge and discharge. The Co^{3+} in LiCoO_2 , for example, may be reversibly oxidized to Co^{4+} when the electrode is charged.⁷³ The same is true for Prussian Blue and its analogues: the transition metal cations they contain may undergo reversible changes in their valence states, the result of which is the ability to reversibly oxidize and reduce these materials. As both the P and R sites in the crystal structure contain transition metals, either the P site cation, or the R site cation, or both, may undergo reversible electrochemical cycling. For example, during the reduction of Prussian Blue to Everitt's Salt, the P-site Fe^{3+} is reduced to Fe^{2+} at 0.45 V vs. S.H.E. (Fig. 15):^{35, 145, 175}



The reduction of the P-site Fe^{3+} occurs concurrently with the insertion of K^+ (or another alkali ion) into the unoccupied A sites in the structure. The carbon-coordinated Fe^{2+} in the R site of Prussian Blue can also be oxidized to Fe^{3+} at 1.1 V vs. S.H.E., producing Berlin Green:

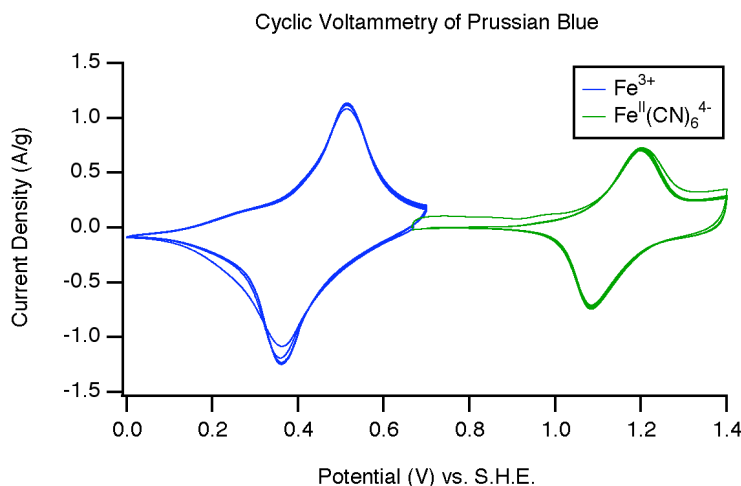
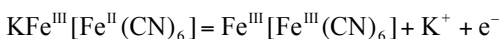
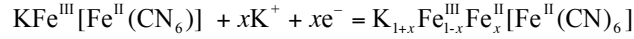


Figure 15: Cyclic voltammetry of Prussian Blue in 1 M KNO_3 at a scan rate of 1 mV/s shows two reactions. At 0.45 V vs. S.H.E., nitrogen-coordinated Fe^{3+} at the P sites is reduced to Fe^{2+} , producing Everitt's Salt. At 1.1 V, $\text{Fe}^{\text{II}}(\text{CN})_6^{4-}$ is oxidized to $\text{Fe}^{\text{III}}(\text{CN})_6^{3-}$, producing Berlin Green. These samples were prepared and tested using techniques described in Chapters 8 and 9.

During the electrochemical cycling of a Prussian Blue analogue, the occupancy of the A sites by the insertion species varies, but there are no changes to the framework structure.¹⁷⁵⁻¹⁷⁷ These reactions therefore proceed by a single-phase, solid solution reaction. As a simple example, consider the partial reduction of

Prussian Blue to an intermediate oxidation state:



When $0 \leq x \leq 1$, a solid solution of Fe^{3+} and Fe^{2+} exists on the P sites. Evidence that electrochemical cycling of Prussian Blue analogues proceeds by a single phase insertion reaction includes the gradual change in lattice parameter and optical properties with charge state, and the single, smoothly curved potential profile of the reaction.^{94, 144, 176} The thermodynamics of this reaction were discussed at length by McCargar and Neff.¹⁴⁵ An example of the latter is shown in Fig. 16, which shows the potential profile of CuHCF during its reaction with K^+ .

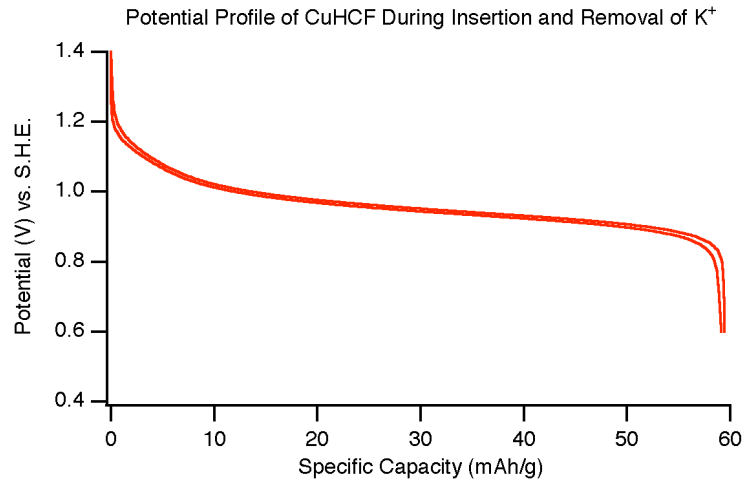


Figure 16: The reaction potential profile of CuHCF during the reversible insertion of K^+ . The details of the experimental setup for electrochemical cycling of CuHCF electrodes are discussed in Chapter 9.1. This S-curve profile indicates a single-phase solid solution reaction.

In the case of an insertion reaction with no changes in the structure of the solid phase, but a varying concentration of the intercalant at interstitial sites, the reaction potential may be related to the fractional occupancy of those sites by the following expression:⁷⁵

$$V(x) = A - B \left(\frac{x^{2/3}}{m^*} \right) - \left(\frac{RT}{nF} \right) \ln \left(\frac{x}{1-x} \right)$$

Here, x is the fractional occupancy of available interstitial sites by the intercalant, m^* is the effective electron mass, and A and B are constants. The second term is related to the Fermi level of the electrons in the material, which in turn depends on its oxidation state (and therefore, the concentration of the intercalant). The last term is responsible for the change in the curvature of $V(x)$ that creates the S-shape, and it represents the effect of the insertion species concentration on the configurational entropy of the intercalant. The S-curve potential profile of CuHCF during its reaction with K^+ is therefore indicative of an insertion reaction during which the intercalant concentration at the A sites varies, but during which there is no change in the phase of the framework.

Most of the Prussian Blue analogues used in electrochromic devices and batteries rely on the reversible oxidation of hexacyanoferrate at the R site. Hexacyanoferrate has been shown to be the electrochemically active group in Prussian Blue analogues containing ions of Ti, V, Cr, Mn, Fe, Co, Ni, Cu, Zn, and many other transition metals at the P sites.^{100, 107, 120-122, 126, 133, 157-163} The reaction potential of hexacyanoferrate in Prussian Blue analogues is typically between 0.8 and 1.1 V vs. S.H.E., and smaller, more highly charged P-site cations result in higher reaction potentials for the hexacyanoferrate.^{159, 178} Prussian Blue analogues containing other R-site species besides Fe may also be prepared, as hexacyanometalates of Ti, V, Cr, Mn, Co, Ir, Ru, and Pt also exist.^{120-122, 156} However, they are used as electrodes much less often than hexacyanoferrates because of their chemical instability and low reaction potentials. Further discussion of non-hexacyanoferrate Prussian Blue analogues occurs in Chapter 13.

In Prussian Blue itself and a few of its analogues, the P-site cation is electrochemically active.^{158, 175, 179} For this to occur, the cation at that site must be capable of a valence change that does not destabilize the structure, at a reaction potential within the stability window of the electrolyte. In zinc hexacyanoferrate, for example, electrochemical activity of the P-site Zn^{2+} has never been observed because Zn^{2+} is reduced directly to metallic Zn^0 , rather than Zn^+ , and because the reduction potential of Zn^{2+} is -0.76 V vs. S.H.E., far below the hydrogen reduction potential of the mildly acidic aqueous electrolytes in which Prussian Blue analogues are typically used. On the other hand, the P-site Fe^{3+} in Prussian Blue can be reduced to Fe^{2+} at a moderate potential of 0.45 V vs. S.H.E., so its activity is easily observed. Hexacyanoferrates of Cr, Mn, Co, Ni, Cu, and Zn, among others, have no P-site electrochemical activity, and only the hexacyanoferrate can be electrochemically cycled.¹⁵⁹ However, it was recently shown that P-site Cu^{2+} can be reversibly reduced to Cu^+ in copper hexacyanocobaltate, even though Cu^{2+} is electrochemically inert in CuHCF .¹⁶⁹ This illustrates that while some general principles govern which species are electrochemically active in the Prussian Blue structure, unpredictable exceptions exist.

The theoretical specific capacity for the complete reaction of either the P site or R site cations in the Prussian Blue framework is about 85 mAh/g. This value varies for different Prussian Blue analogues because each one has a different mass. The observed specific capacities are actually about 60 mAh/g because of the substantial hydration of the structure, and because the P:R ratio is typically greater than one. The true specific capacity of a Prussian Blue analogue can be determined using the results of a chemical analysis, which allows calculation of the mass fraction that is an electrochemically active group (such as $\text{Fe}(\text{CN})_6$). Prussian Blue analogues have about one third of the specific capacity of the lithium ion insertion electrodes used in lithium-ion batteries. However, for stationary storage applications, capacity is less important than cycle life, power, and energy efficiency.^{6-7, 10}

The electrochemical activity and electrochromism of Prussian Blue was first exploited by Neff in 1978, who showed that electrodeposited thin films of it could be reversibly reduced to Everitt's Salt, or reversibly oxidized to form Berlin Green during insertion or removal of potassium ions.³⁵ Soon afterwards, in 1981, Itaya and Shibayama found that Prussian Blue could be reversibly reduced to Everitt's Salt over 10^5 times without substantial capacity loss.⁹³ This latter result sparked a flurry of attempts to commercialize

electrochromics based on Prussian Blue. In later years, others duplicated Itaya's initial result, and in some cases nearly 10^7 cycles were demonstrated for Prussian Blue thin films.⁷⁰ The vast majority of research during this time relied on K^+ as an insertion ion, though in 1982, both Prussian Blue and nickel hexacyanoferrate (NiHCF) were found readily insert other alkali ions.^{68-69, 139} Of these studies on the effects of different insertion ions, most interesting was work led by Andrew Bocarsly, which achieved 18,000 cycles of Na^+ insertion into NiHCF with only 10% capacity loss.¹⁴¹ Interest in the behavior of Prussian Blue analogues was not confined to NiHCF, and during the mid-1980s, CuHCF and some non-hexacyanoferrates such as iron hexacyanoruthenate (Ruthenium Purple) were also studied.^{138, 140}

Just after Neff's initial discovery of electrochromism in Prussian Blue, a French research group studied Prussian Blue analogues as cathodes for organic electrolyte lithium-ion batteries.³⁶⁻³⁷ This work has generally been overlooked, and Neff is frequently credited for the invention of the first Prussian Blue battery in 1985.³⁸ In Neff's cell, both electrodes were comprised of Prussian Blue when fully discharged. However, upon charging, the cathode was oxidized to Berlin Green, while the anode was reduced to Everitt's Salt. This resulted in a full cell voltage of about 0.6 V. Others soon duplicated Neff's design, and throughout the late 1980s and early 1990s, batteries using Prussian Blue anodes and cathodes were studied in a variety of geometries.³⁹⁻⁴⁶ The use of other analogues as battery electrodes instead of Prussian Blue itself was first reported by Grabner and Kalwellis-Mohn.³⁹ In 1986, they described a cell containing a CuHCF cathode and a Prussian Blue anode, which achieved over 700 cycles. Soon afterwards, in 1989, the pair demonstrated a cell that cycled a NiHCF cathode and a nickel hexacyanoruthenate anode in an aqueous Na^+ electrolyte.⁴² It must be noted that all of these studies used electrodeposited thin film electrodes. With electrode mass loadings on the order of $1 \mu\text{g}/\text{cm}^2$, these devices had limited practical use. Until the work performed for this thesis (Chapters 8-16), with few exceptions bulk Prussian Blue analogue electrodes were not studied for use in batteries.⁴³⁻⁴⁴

7.6: Other Applications for Prussian Blue Analogues

Though the work done for this thesis concerns the electrochemical properties of Prussian Blue analogues, and how they can be used as battery electrodes, members of this materials family have been used for many other applications. Prussian Blue is still used for its original application, as a pigment and dye for art, clothing, blueprints, and even cell staining.

Of the modern applications for Prussian Blue analogues, foremost is its use in electrochromic devices. Numerous Prussian Blue analogues exhibit electrochromic behavior, and over 38 years after the initial discovery, research in this area continues.

The affinity of Prussian Blue analogues for so many hydrated cations has led to some development of selective ion sensors based on a variety of hexacyanoferrate-based materials. Indeed, Prussian Blue's rapid sorption of cesium has resulted in its use as an antidote for Cs-137, a dangerous radioisotope. It has also been used as an antidote to heavy metal poisoning (most commonly thallium).^{139, 180-181}

For several decades, Prussian Blue and its analogues have received considerable attention from the

physics community because of their magnetic properties. In Prussian Blue, the P site Fe^{3+} is in a high spin ($s=5/2$) state, and near absolute zero, these spins will order, making the material highly magnetic.¹⁰¹⁻¹⁰² Other, more complex Prussian Blue analogues based on the hexacyanochromate, hexacyanomanganate, and even hexacyanovanadate complexes have been found to have magnetic ordering temperatures near and above room temperature. Practical applications for these temperature-controlled magnetic switches remain to be seen, for those particular materials are chemically unstable against the release of hydrogen cyanide.¹⁸²⁻¹⁸⁵

Finally, the zeolitic nature of the Prussian Blue structure allows it to store not only ions from an electrolyte, but gaseous species. Recent research in this area has targeted a number of Prussian Blue analogues for hydrogen storage and CO_2 capture applications.¹⁸⁶⁻¹⁸⁷

In summary, materials in the Prussian Blue family can be used not only as battery electrodes, but also for many other purposes. This is due primarily to the open framework structure, which allows reversible transport of many different intercalants in and out of the structure.

Chapter 8: Bulk Co-Precipitation Synthesis of Prussian Blue Analogues

8.1 Motivation for the Development of Bulk Synthesis Methods

In Chapter 7.3, two general strategies for the synthesis of Prussian Blue analogues were described: chemical precipitation, and electrodeposition. Only chemical deposition can be used to produce a practical amount of material for battery applications. Electrodeposition has been used in the vast majority of studies of the electrochemical properties of these materials; however as the thin films formed by electrodeposition have the form and properties that make them desirable electrochromic materials.

Electrodeposited thin film samples are not desirable for use in batteries. They typically have mass loadings of about $1 \mu\text{g}/\text{cm}^2$. In contrast, commercial batteries have electrode mass loadings of tens of mg/cm^2 . To achieve an increase in mass loading of a factor of 10^4 to 10^5 , electrodeposition must be abandoned in favor of bulk synthesis by chemical deposition, which can readily be scaled up to produce kg, or even metric tonnes, of Prussian Blue analogue powders.

8.2: Synthesis of Copper Hexacyanoferrate and Nickel Hexacyanoferrate

A new co-precipitation method was developed to produce Prussian Blue analogues with consistent chemical compositions in bulk. It is fast and scalable, and is performed at or near room temperature using inexpensive, reagent grade precursors in aqueous solutions. In a typical synthesis, 70 mL of aqueous $\text{Cu}(\text{NO}_3)_2$, $\text{Ni}(\text{NO}_3)_2$, or both, and a second precursor solution of 70 mL aqueous $\text{K}_3\text{Fe}(\text{CN})_6$ were combined by slow, simultaneous drop-wise addition to 60 mL pure water with constant, vigorous stirring, such that the final concentrations were 40 mM of Cu^{2+} or Ni^{2+} , and 20 mM $\text{Fe}(\text{CN})_6^{3-}$. For example, 0.008 mol Cu^{2+} was present at a concentration of 40 mM in 200 mL total volume upon complete addition of the precursors; however, during the initial addition of the precursor solutions to water, their concentrations were much lower. Combination of reactants by this co-precipitation method resulted in a constant ratio of Cu^{2+} or Ni^{2+} to $\text{Fe}(\text{CN})_6^{3-}$.

In contrast, virtually all of the previously described precipitation syntheses of CuHCF and NiHCF rely on the direct addition of one precursor solution to the other, so the ratio of Cu^{2+} or Ni^{2+} to $\text{Fe}(\text{CN})_6^{3-}$ varies during the reaction.¹⁶⁴ The composition of CuHCF has been shown to depend on the ratio of Cu^{2+} to $\text{Fe}(\text{CN})_6^{3-}$ present during synthesis, so the co-precipitation method avoids any inconsistencies in the properties of CuHCF or NiHCF that might result from variations in their stoichiometry.¹⁶⁴⁻¹⁶⁵

During the reaction, the co-precipitated Prussian Blue analogues initially formed colloidal suspensions. Without a large excess of the metal salt precursor, these colloids were stable, the product particles were too small to filter from the solvent, and it could be isolated only through centrifugation or solvent evaporation. For this reason, a 2:1 ratio of the metal salt precursor to $\text{Fe}(\text{CN})_6^{3-}$ was used. When given adequate time (up to four hours), the products of these reactions with excess metal salt precursors fully precipitated.

Characterization of NiHCF by XRD and SEM found little change in the morphology or crystallinity when the solid product was collected immediately after precipitation, or eight hours later (Fig. 17). Heating (if any) was stopped at completion of the addition of the precursor solutions, and heated solutions were cooled slowly to room temperature. The precipitated Prussian Blue analogues were collected using vacuum filtration, and dried in vacuum at room temperature. Grinding by hand produced fine powders that were used for physical characterization and electrode preparation.

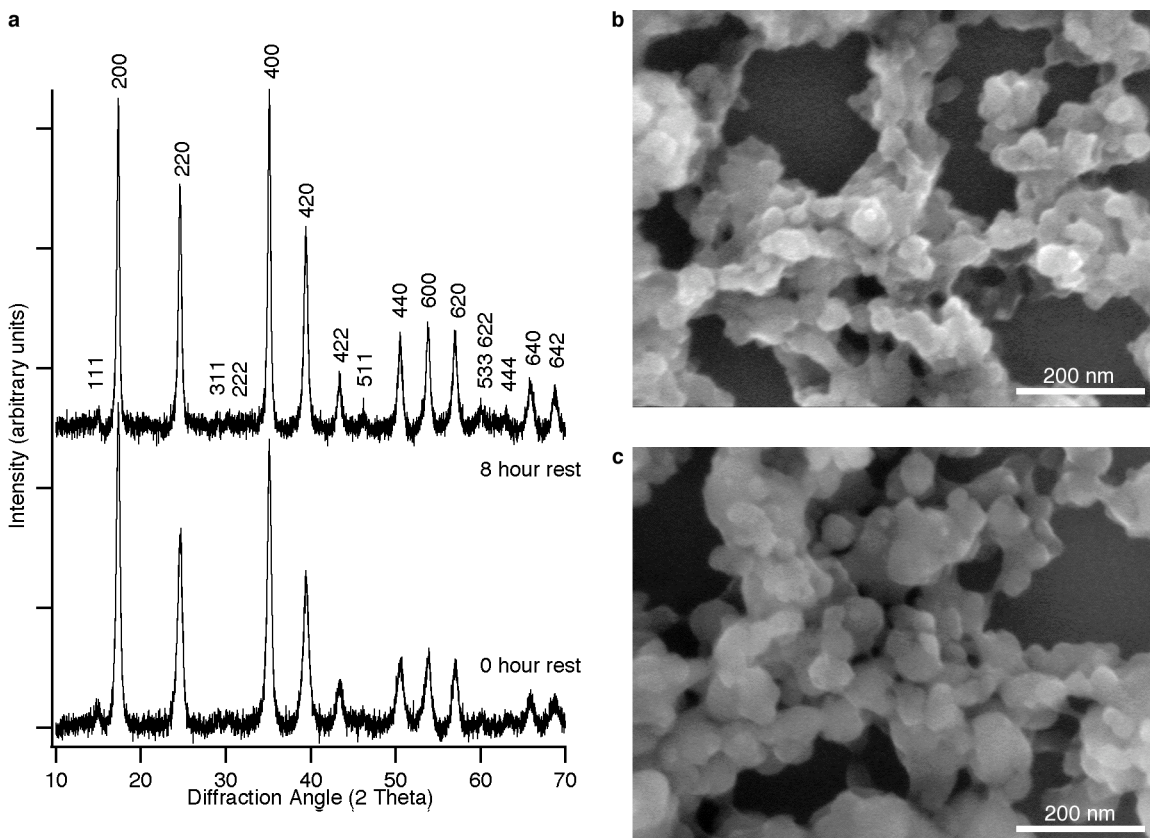


Figure 17: Physical characterization of NiHCF synthesized at 70° C by XRD shows that an eight hour delay before filtering NiHCF after the initial precipitation does not result in a change in crystallinity. Furthermore, SEM shows no substantial differences between the morphologies of freshly precipitated NiHCF (**b**), and NiHCF collected after eight hours in solution (**c**).

The crystallinity of Prussian Blue analogues synthesized using the co-precipitation method was found to depend on the equilibrium precursor concentration needed to initiate precipitation, and therefore, on the temperature. At higher temperatures, the trace solubility of Prussian Blue analogues is higher, so the precursors can be present in higher concentrations before they become supersaturated and precipitation begins. The exchange of precursor species between the solution and the surface of a growing nanoparticle will be faster at higher temperatures, which results in slower nanoparticle growth, fewer defects, and higher crystallinity. Another way to slow down nucleation and growth of a solid precipitate is to decrease the concentration of the precursors. During precipitation, the precursors are supersaturated. By keeping their

concentration as close to the equilibrium saturation limit as possible, the thermodynamic driving force for precipitation will be smaller and particle growth will occur more slowly. Though a quantitative study of the relationship between synthesis temperature, precursor solution concentration, precursor saturation limit, and the crystallinity and morphology of Prussian Blue analogues was not undertaken, the general trends between these variables will be elucidated using several examples.

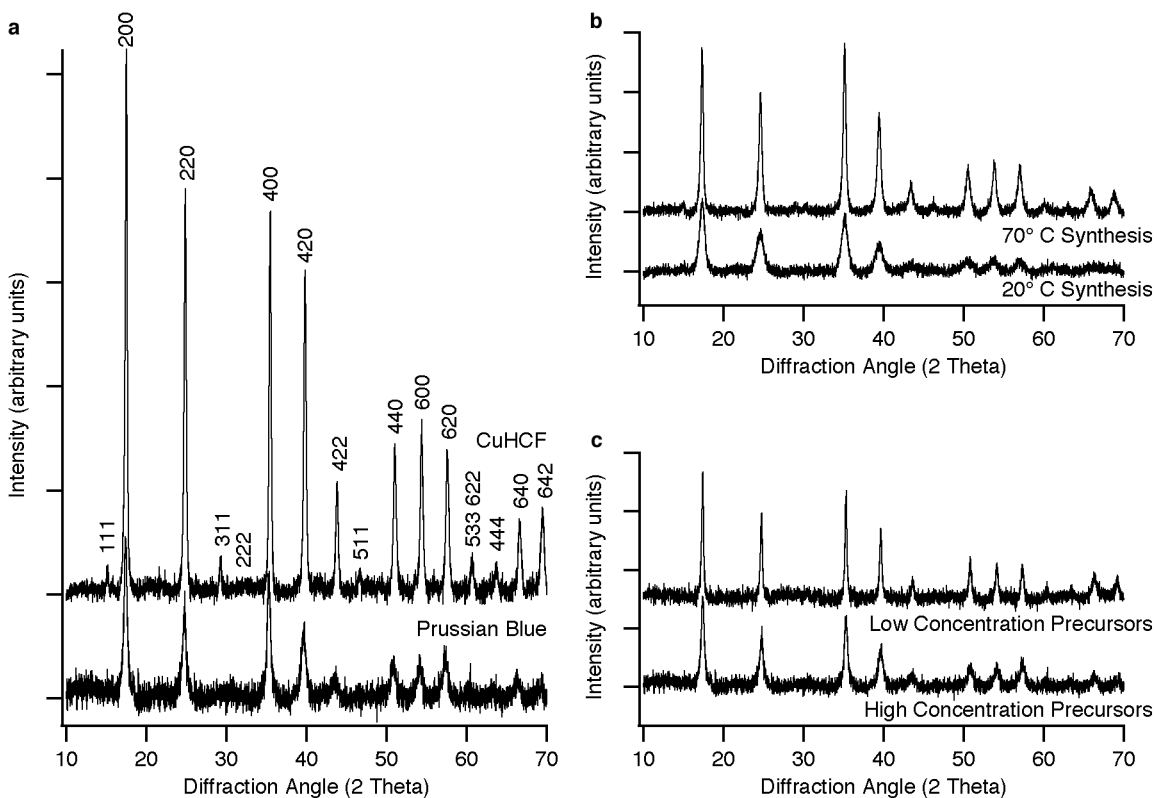


Figure 18: The effects of synthesis conditions on the crystallinity of Prussian Blue analogues. **(a)** CuHCF has high crystallinity when synthesized at room temperature. In comparison, Prussian Blue synthesized using the same precursor concentrations as for CuHCF, but at 70° C, has poorer crystallinity. **(b)** The crystallinity of NiHCF synthesized at 70° C is greater than that of NiHCF synthesized at 20° C. **(c)** Decreasing the concentration of the precursor solutions tenfold results in a small improvement in crystallinity of Prussian Blue. The intensities of the scans in each panel are normalized, but the intensity scales of the panels are different from one another. The “High Concentration Precursors” Prussian Blue sample in **(c)** is also plotted in **(a)** to show that CuHCF has much better crystallinity.

At room temperature, CuHCF did not begin to precipitate upon the initial combination of the Cu^{2+} and $\text{Fe}(\text{CN})_6^{3-}$ precursors, but began once the precursor concentrations reached about 5 mM (the approximate saturation limit). This resulted in a highly crystalline CuHCF product, even when synthesis was performed

at room temperature (Fig. 18a). However, this was not generally observed for other Prussian Blue analogues, many of which precipitate much more rapidly at much lower precursor concentrations. For example, at room temperature precipitation of NiHCF begins immediately upon the combination of its Ni^{2+} and $\text{Fe}(\text{CN})_6^{3-}$ precursors, resulting in a poorly crystalline product. Upon raising the reaction temperature to 70°C , NiHCF precipitated more slowly, only after the precursor concentrations increased above about 5 mM. This slower precipitation at 70°C resulted in a more crystalline precipitate than the rapid precipitation at room temperature (Fig.18b). Precipitation of Prussian Blue from Fe^{3+} and $\text{Fe}(\text{CN})_6^{4-}$ occurs instantly, even at temperatures of 80°C and higher, and only poorly crystalline powders could be prepared using precursor concentrations of 20-40 mM. The crystallinity was somewhat improved by a tenfold reduction in precursor solution concentrations, to 4 mM Fe^{3+} and 2 mM $\text{Fe}(\text{CN})_6^{4-}$ (Fig. 18c). The increases in crystallinity observed for syntheses at either higher temperature or from more dilute precursor solutions show that by delaying co-precipitation until a reaching a non-negligible precursor concentration, highly crystalline Prussian Blue analogues can be obtained.

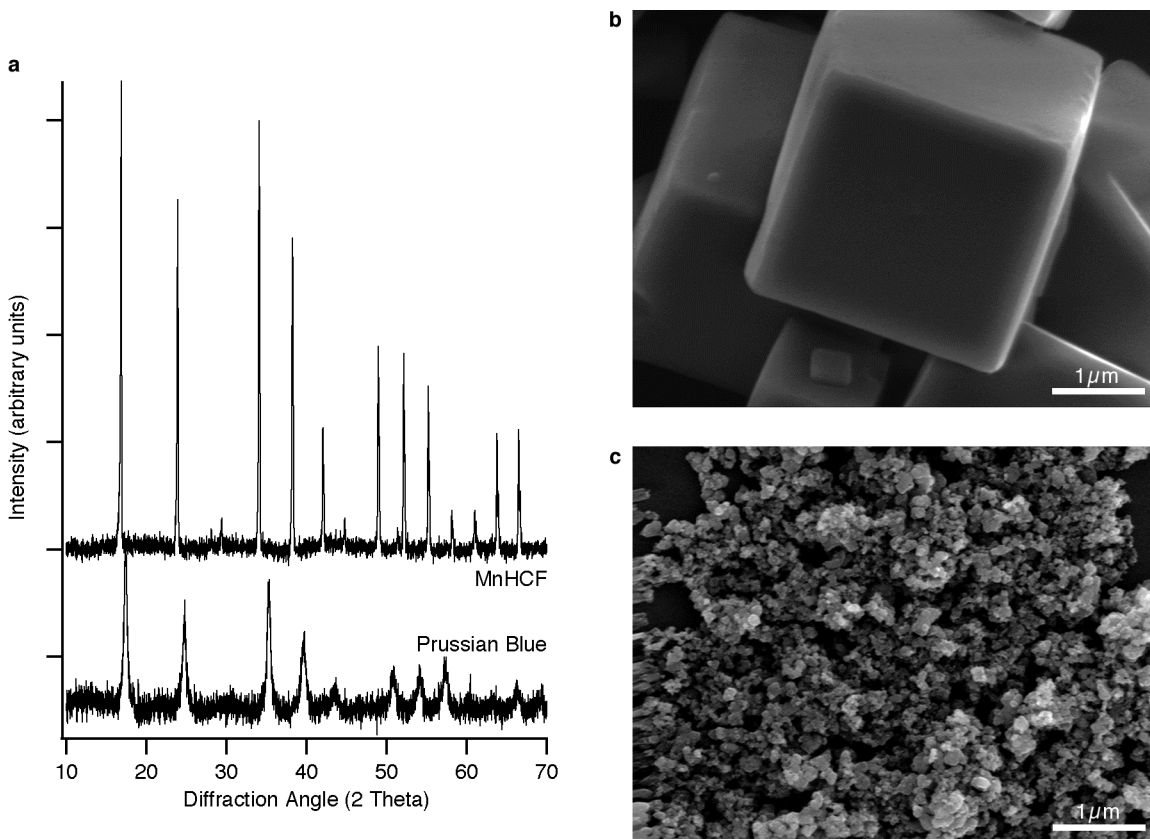


Figure 19: (a) MnHCF synthesized at 70°C is much more crystalline than Prussian Blue synthesized at the same temperature, from precursors that were ten times more dilute. The slow precipitation of MnHCF resulted in large, faceted cubic grains (b), while the rapid precipitation of Prussian Blue resulted in unfaceted nanoparticles of 20-50 nm (c).

An extreme example of the relationship between the precipitation rate of a Prussian Blue analogue and its crystallinity and morphology is manganese hexacyanoferrate (MnHCF). During synthesis, the precursors of Mn^{2+} and $\text{Fe}(\text{CN})_6^{3-}$ were stable at room temperature until reaching a high saturation limit of about 10 mM. Upon further addition of the precursors, MnHCF precipitated slowly, and formed grains much too large to remain suspended in solution. Physical characterization of MnHCF by XRD and SEM revealed that it was far more crystalline than other Prussian Blue analogues synthesized by the co-precipitation method (Fig. 19). Both its strong XRD signal and its sharply faceted morphology show that it is much more crystalline than the CuHCF, NiHCF, or Prussian Blue also synthesized using this method. Highly crystalline Prussian Blue analogues can be synthesized by co-precipitation if the reaction conditions are such that the precursors have a non-negligible saturation limit in the presence of one another.

The co-precipitation synthesis not only provides control over the crystallinity of Prussian Blue analogues, but it is also exceedingly practical. The products are made from low cost, reagent grade chemical precursors that may be procured in large quantities. They reacted in water, at or near room temperature, in only a few minutes. Though the yield from the co-precipitation method was not quantitatively characterized, the vast majority of the hexacyanometalate precursor is incorporated into the final product, and the excess metal salt may be recycled for another synthesis batch. The low cost, speed, and scalability of the co-precipitation synthesis will allow Prussian Blue analogues to be prepared on much larger scales (metric tons of product) than used here (a few grams). This will allow them to be used as battery electrodes in large batteries for stationary storage.

8.3: Methods for Physical and Electrochemical Characterization

After completion of the co-precipitation synthesis method, the solid product was dried in vacuum at room temperature to remove excess water, and then ground by hand. The raw powder product was used for physical characterization. For XRD measurements, about 10 mg of the Prussian Blue analogue was adhered to a glass slide coated with vacuum grease. This resulted in well-packed samples of nearly 1 mm in thickness. In comparison, typical X-ray absorption depths are about 100 μm or less. The large sample excess means that differences in signal intensity between samples are a result of differences in crystallinity, and not sample mass loading.

The open framework structure of Prussian Blue results in a relatively low density of about 1.8 g/cm^3 . In addition, most of the atoms in the framework are C, N, O, or H, none of which scatter X-rays strongly. The result is that even highly crystalline Prussian Blue analogues diffract weakly, when compared to metal alloys and oxides. Strong diffraction signals required scans of about two hours in duration, double the time needed for XRD scans on $\text{LiTi}_2(\text{PO}_4)_3$ (Chapter 6).

Electron microscopy samples were prepared by sonicating the well-ground Prussian Blue analogue powder in methanol before drop casting this solution onto the sample holder.

Elemental analysis of Prussian Blue analogues was performed using inductively coupled plasma mass spectrometry (ICP-MS). Samples were prepared by dissolving about 0.5 mg of sample powder in

concentrated hydrochloric acid, and then diluting to a desired concentration with water.

Along with physical characterization of the raw Prussian blue analogue powders using XRD, SEM, and TEM, electrochemical characterization was performed using slurry electrodes.

Electrodes containing Prussian Blue analogues were prepared by methods similar to those described in Chapter 4 for the preparation of lithium ion electrodes. An active material such as CuHCF or NiHCF was ground by hand with amorphous carbon (Timcal Super P Li), polyvinylidene difluoride (Kynar HSV900), and graphite (Timcal KS6) in a 80:9:9:2 mass ratio until a homogeneous black powder was formed. This black powder was stirred in NMP for at least one hour, and then deposited on carbon cloth current collectors (Fuel Cell Earth, Inc.). These electrodes were dried in vacuum at less than 100° C for at least one hour. Prussian Blue analogues are known to release hydrogen cyanide gas if heated, but CuHCF, NiHCF, Prussian Blue, and a few others will remain stable at temperatures of 80-100° C.

These electrodes were inserted into cells that also contained a Ag/AgCl reference electrode, a counter electrode, and excess electrolyte. For brief measurements such as cyclic voltammetry scans, a platinum counter electrode was used. However, for long-term measurements such as extended galvanostatic cycling, a large, partially charged mass of CuHCF, NiHCF, or Prussian Blue was used as the counter electrode. The purpose of this counter electrode was to act as a reversible source and sink of the insertion ions needed for the reaction of the working electrode. As the working and counter electrode had similar potentials, these cells were not practical batteries, but rather, characterization tools for evaluation of the performance of the working electrode alone. Typical working electrodes were 1 cm², while typical counter electrodes were about 10 cm². The mass loading of working electrodes was between 5 and 10 mg/cm² unless otherwise noted, while the mass loading of counter electrodes was 15-20 mg/cm².

Aqueous electrolytes containing one molar alkali nitrate salts were prepared, and their pH was lowered to 2 using nitric acid. An acidic pH was selected for electrochemical testing because numerous studies of Prussian Blue electrochromic devices found improved cycle life at lower pH. Though the hexacyanoferrate anion is stable in mild acid, exposure of other solids containing cyanide should be avoided due to their tendency to decompose into hydrogen cyanide.

In the case of full cell testing of CuHCF cathodes and an anode with a low reaction potential (Chapter 3.12), flooded cells were also used, but the anode was inserted in place of the large, partially delithiated Prussian Blue analogue counter electrode. It is possible to construct sealed pouch cells containing Prussian Blue electrodes, but their longevity is limited by the slow capillary action of the electrolyte through the CC current collector and out of the pouch. Though the use of a conventional metal current collector would alleviate this problem, it might not remain stable against corrosion in acidic electrolytes, especially at the oxidative potentials at which the hexacyanoferrate cathodes operate.

Chapter 9: The Copper Hexacyanoferrate Cathode

9.1 Physical Properties of Copper Hexacyanoferrate

Though Prussian Blue itself was the first electrode studied during the work for this thesis, it was found to suffer from low coulombic efficiency and poor cycle life. Attention was turned to other Prussian Blue analogues, and the first to receive full electrochemical characterization was CuHCF.¹⁵⁰ The co-precipitation synthesis was found to easily produce highly crystalline CuHCF at room temperature, and quantities of over 5 g could be prepared without difficulty in a single synthesis using equipment of the scale commonly found in academic wet chemistry laboratories. X-ray diffraction (Fig. 18a) of CuHCF found that this material was phase pure and had a FCC structure with a lattice parameter of 10.12 Å, in close agreement to previously reported data. Using elemental analysis by ICP-MS and previously established rules for the hydration of the structure, CuHCF was found to have the chemical formula $K_{0.71}Cu[Fe(CN)_6]_{0.72} \cdot 3.7H_2O$.

Study of the morphology and crystallinity of CuHCF was performed using TEM with help from Dr. Judy Cha and Matthew T. McDowell. The material was found to be comprised of 20-50 nm particles (Fig. 20a), a typical size range for Prussian Blue analogues synthesized by chemical precipitation. Electron diffraction of CuHCF and other Prussian Blue analogues using TEM was difficult because these materials were found to be unstable under the irradiation of the electron beam. Under high magnification, no diffraction spectra were ever observed. However, at low beam current and for large sample areas, diffraction patterns that remained stable for up to one minute were observed (Fig. 20b). The electron diffraction rings observed using TEM matched the high intensity peaks of the X-ray diffraction spectrum.

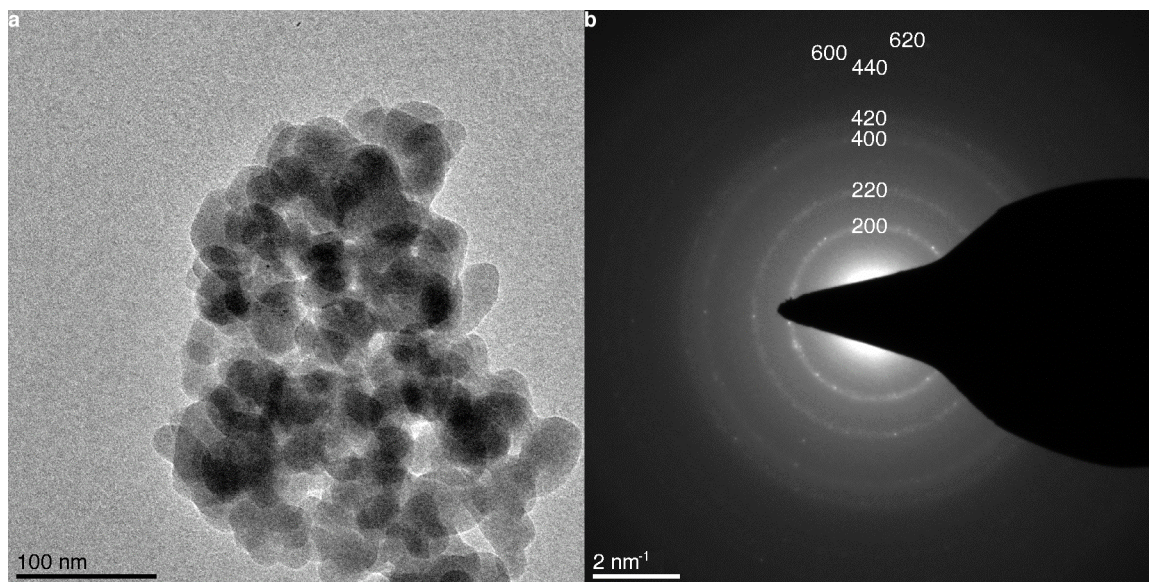


Figure 20: (a) TEM shows that CuHCF is comprised of 20-50 nm grains. A stable TEM diffraction pattern (b) was achieved using low beam currents over large areas. The fully indexed TEM diffraction pattern matches the XRD spectrum of CuHCF (Fig. 17a).

9.2 Electrochemical Properties of Copper Hexacyanoferrate

Electrochemical characterization of CuHCF electrodes with mass loadings of about 10 mg/cm^2 was performed in flooded three-electrode cells containing a $1 \text{ M KNO}_3/0.01 \text{ M HNO}_3$ electrolyte.¹⁵⁰ Galvanostatic cycling, cyclic voltammetry, and impedance spectroscopy were all performed to elucidate the behavior of CuHCF in these conditions. The potential of CuHCF at a half-charged state during K^+ insertion was measured at 0.95 V vs. S.H.E. using both cyclic voltammetry and galvanostatic cycling. This is quite close to the reaction potential previously observed for electrodeposited thin films of this material.^{140, 159} To determine whether potassium ions or protons was the intercalant during this reaction, cyclic voltammetry of CuHCF was performed at both $\text{pH}=2$ and $\text{pH}=5.5$ (Fig. 21). The reaction potential of CuHCF was found to be independent of pH , confirming that potassium ions, but not protons, are intercalated. The S-curve potential profile observed during galvanostatic cycling (Fig. 22a) is characteristic of a single-phase insertion reaction.

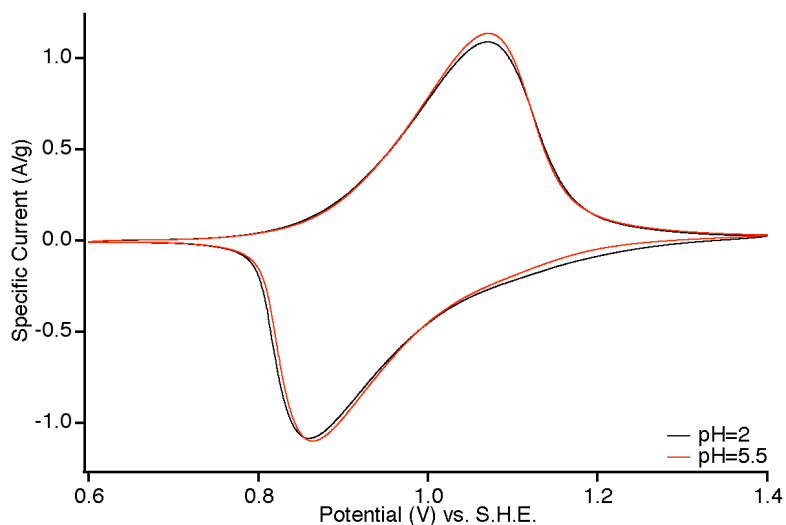


Figure 21: Cyclic voltammetry of CuHCF at a scan rate of 1 mV/s in 2.5 M KNO_3 at $\text{pH}=2$ and $\text{pH}=5.5$. The potential of the reaction does not change with pH , so K^+ is the dominant intercalant.

Galvanostatic cycling of CuHCF was performed between 0.6 and 1.4 V vs. S.H.E. at current densities between 50 mA/g and 5 A/g . As the maximum specific capacity of Prussian Blue analogues is about 60 mAh/g , this value was used to define a 1C rate for all materials in this family. Thus, 50 mA/g is 0.83C , 5 A/g is 83C , and so on. A maximum capacity of 59.14 mAh/g was observed for CuHCF during cycling at $\text{C}/6$ (not shown in Fig. 22). In general, much lower current densities (0.1C or lower) are needed to determine the maximum capacity of a battery electrode. However, the voltage hysteresis of CuHCF during cycling at 0.83C was only 4.4 mV , demonstrating that the electrode was near its equilibrium potential at all times. CuHCF was found to have excellent capacity retention at higher current densities, as it retained 40.1 mAh/g (67% of its maximum capacity) when the current density was increased 100-fold to 83C . The

capacity retention of CuHCF at high current densities compares favorably with recent results on LiFePO_4 and $\text{Li}_4\text{Ti}_5\text{O}_{12}$, two lithium ion insertion electrodes considered to have fast kinetics (Fig. 22b).

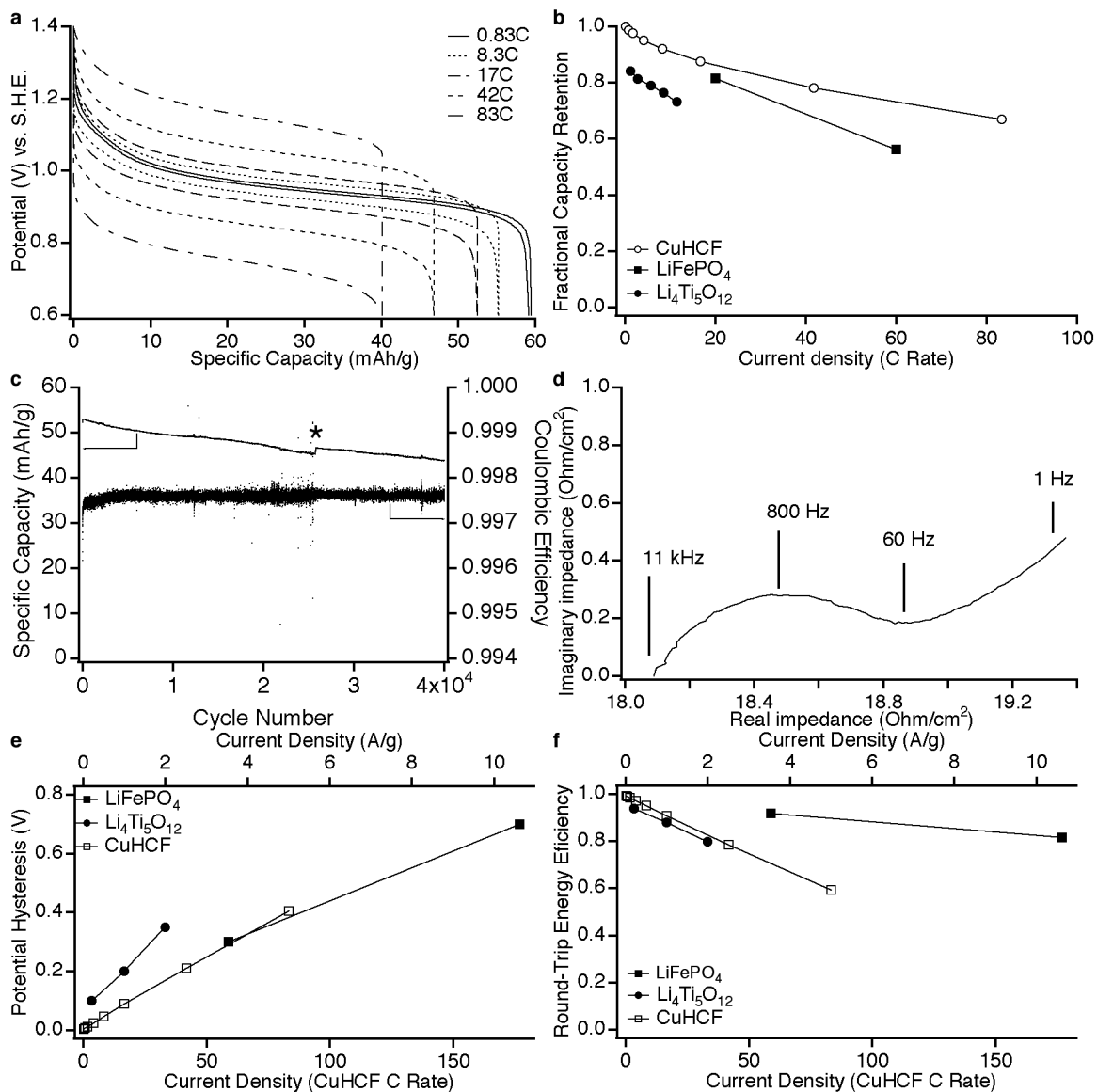


Figure 22: (a) Potential profiles of CuHCF during galvanostatic cycling at various current densities. (b) CuHCF retains 67% of its maximum capacity at a 83C rate. (c) CuHCF retains 83% of its initial discharge capacity after 40,000 cycles. The asterisk denotes the addition of electrolyte to the cell after 25,000 cycles in response to evaporation. (d) Impedance spectroscopy of CuHCF found a charge transfer resistance of about $1 \Omega/\text{cm}^2$. (e) The potential hysteresis increases linearly with current density, and is primarily caused by the electrolyte resistance of the flooded cell. (f) A hypothetical 1 V cell using CuHCF and a reversible anode has energy efficiencies of up to 99%. The data for LiFePO_4 and $\text{Li}_4\text{Ti}_5\text{O}_{12}$ are adapted from Ref. 190-191.

The cycle life of CuHCF was studied by galvanostatic cycling between 0.8 and 1.2 V vs. S.H.E. at a 17C rate (1 A/g). Over that potential range and at that current density, an initial discharge capacity of 52.2 mAh/g was observed. After 10,000 cycles, 94.6% of that initial capacity was retained, after 40,000 cycles 83% was retained. A coulombic efficiency of about 99.8% was observed throughout the course of cycling (Fig. 22c). The cycle life of CuHCF is at least an order of magnitude longer than commercial lead acid, lithium ion, and sodium sulfide batteries as of 2011.^{6-7, 10, 14-15} If the CuHCF cathode is paired with an anode that does not limit cycle life, full cells with longer cycle lives than existing batteries will be possible.

Impedance spectroscopy was performed to gain further information about the reaction of CuHCF with K^+ . In a typical impedance spectroscopy measurement, an alternating current of small amplitude (a few μA) is applied to the sample, and its real and imaginary impedance is measured. These measurements are made for alternating currents with frequencies ranging from over 100 kHz to less than 1 Hz. The results of impedance spectroscopy measurements are typically displayed using a Nyquist Plot, in which the imaginary impedance is plotted along the ordinate axis, and the real impedance is plotted along the abscissa. Details of the interpretation of impedance spectroscopy measurements are discussed elsewhere.

The most important feature of the Nyquist Plot of CuHCF during its reaction with K^+ (Fig. 22d) is its low charge transfer resistance of $1 \Omega/cm^2$. This value is similar to that previously found for CuHCF thin films, but is about 100 times lower than that of common lithium-ion insertion materials such as $LiCoO_2$ and $LiFePO_4$.^{140, 188-189} The high rate performance of CuHCF is not limited by the insertion and removal of K^+ .

Rather, the rate capability of CuHCF was limited by the flooded cell geometry used in these measurements. The potential hysteresis at a half-charged state was found to increase linearly with current density, from 4.4 mV at 0.83C, to 405 mV at 83C. This ohmic behavior was due to the ionic resistance of the electrolyte and the electronic resistance of the current collectors. The potential hystereses measured for CuHCF are lower than those recently found for lithium ion insertion electrodes in pressed cells. About 700 mV of hysteresis were observed during the cycling of $LiFePO_4$ at a 60C rate, and 350 of mV hysteresis were recently seen during the cycling of $Li_4Ti_5O_{12}$ at a 13C rate.¹⁹⁰⁻¹⁹¹ The potential hysteresis of CuHCF and these materials is compared in Fig. 22e.

The round trip energy efficiency of a battery depends on the coulombic efficiency and the hysteresis between the potential profiles during charge and discharge. Energy is the product of voltage and charge, so the exact expression for energy efficiency is the normalized difference between the integrated potential profiles of charging and discharging:

$$E_{\text{Eff}} = \frac{\int V_{\text{Charge}}(q) dq - \int V_{\text{Discharge}}(q) dq}{\int V_{\text{Charge}}(q) dq}$$

Equivalently, the energy efficiency is equal to one minus the circular integral of the hysteresis between the charge and discharge potential profiles:

$$E_{\text{Eff}} = 1 - \oint V_{\text{Charge}}(q) - V_{\text{Discharge}}(q) dq$$

Calculation of energy efficiency requires a full cell, and the measurements of CuHCF were performed using a half-cell setup and a very low voltage difference between the working and counter electrodes. However, as discussed below in Chapter 14, CuHCF may be paired with highly reversible anodes such as activated carbon (AC), which has been shown to have extremely low hysteresis and energy loss. Estimated values for the theoretical energy efficiency of a hypothetical 1 V CuHCF/AC cell are shown in Fig. 22f. At the slowest measured cycling rate of 0.83C, its energy efficiency is about 99%. At a moderate cycling rate of 8.3C, its energy efficiency is still 95%. As is shown below (Chapter 3.12), energy efficiencies of over 90% are indeed possible for full cells containing CuHCF and highly reversible anodes. These energy efficiencies are much higher than those of commercial batteries (discussed in Chapter 1), which are typically between 60% and 90%, and they are comparable those found during recent studies of LiFePO₄ and Li₄Ti₅O₁₂.¹⁹⁰⁻¹⁹¹

9.3 Ex-Situ X-ray Characterization of Copper Hexacyanoferrate Electrodes

The initial physical characterization of CuHCF by XRD and TEM found that the material is comprised of highly crystalline, 20-50 nm nanoparticles. The high crystallinity and small grain size allowed K⁺ to rapidly access all of the electrochemically active hexacyanoferrate groups in the structure. It is uncommon for insertion reaction electrodes to have especially long cycle life, as the strains that occur during ion intercalation can lead to decrepitation. Zero-strain insertion electrodes such as Li₄Ti₅O₁₂, however, can last thousands of deep discharge cycles.^{14, 80} To determine the strain that CuHCF undergoes during cycling, ex situ XRD was performed on electrodes at various charge states.¹⁵⁰ Electrodes were fully charged, then fully discharged, and then partially charged at a 1C rate until enough time to reach a desired charge state had elapsed. For example, a 20% charge at 1C required 12 minutes. After removal from the cell, electrodes were washed with water, but no further treatment was performed. The high crystallinity of CuHCF and the high mass loading of the electrodes made acquisition and analysis of the diffraction spectra of the electrodes straightforward. No new peaks or peak splitting appeared during charging, providing further evidence than electrochemical cycling of CuHCF proceeds by a single-phase insertion mechanism. As illustrated by a shift in the position of the 400 peak, the diffraction spectra were observed to shift to lower angles as the charge state increased (Fig. 23a).

This shift in peak positions corresponds to an increase in lattice parameter with charge state (Fig. 23b). The lattice parameters of the electrodes were calculated using a Treor structure refinement algorithm in the X'Pert Highscore Plus software package. The total change in lattice parameter between the fully discharged and fully charged electrodes was 0.1 Å, so CuHCF undergoes a strain of less than 1% during deep discharge cycling. Though it is not a truly zero-strain material like Li₄Ti₅O₁₂, its small strain during cycling is indicative of the chemical stability of the framework. The lattice parameter varied linearly with charge state, so it is proportional to the fraction of hexacyanoferrate that is oxidized in the structure. The length of the Fe-C bond in hexacyanoferrate is known to increase by 0.05 Å upon oxidation because of a decrease in the strength of the π bonding between Fe and C.^{126, 136, 176-177, 192} As each unit cell two has Fe-C bonds along

the $\langle 100 \rangle$ directions of the unit cell, the observed 0.1 \AA strain is due entirely to the change in the Fe-C bond length. In fact, the lattice parameter decreases as CuHCF is discharged and K^+ is inserted, so K^+ must fit within the A sites. This is consistent with the crystal ionic radius of K^+ , which is about the size of the channel between the A sites on the $\{200\}$ type planes, but smaller than the A sites themselves. The hydrated Stokes radius of K^+ is somewhat larger, and it is possible that K^+ coordinates with the zeolitic water already present in the structure after partially de-solvating upon its initial intercalation.¹⁹³

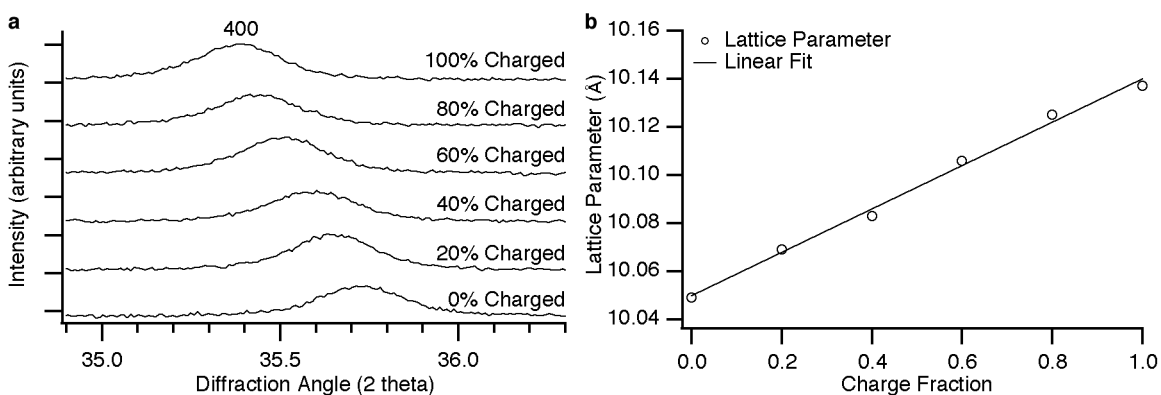


Figure 23: (a) The 400 peak of CuHCF shifts to lower diffraction angles as the charge state increases. This corresponds to a 1% increase in the lattice parameter during charging (b). The lattice strain is linearly proportional to the charge state.

Chapter 10: The Nickel Hexacyanoferrate Cathode

10.1: Motivation for Work on Nickel Hexacyanoferrate

The promising cycle life and rate capability of CuHCF led to the investigation of other Prussian Blue analogues as cathodes in aqueous alkaline ion batteries. The low cost of sodium ion compared to lithium has recently drawn the attention of the battery research community to the prospect of developing sodium ion batteries. Recent research has focus on devices using both organic and aqueous electrolytes, and aqueous sodium ion batteries have recently been commercialized. Though potassium is also much less expensive than lithium, the possibility of using Prussian Blue analogues as electrodes in sodium ion batteries, mixing entropy devices, or desalination systems led to the study of NiHCF. As mentioned in Chapter 7, in the early 1980s, researchers at Princeton led by Andrew Bocarsly demonstrated that electrodeposited thin films of NiHCF could cycle Na^+ for 18,000 cycles.^{139, 141-142} However, thin films Prussian Blue itself was found to have very poor cycle life during Na^+ cycling.⁶⁸ Preliminary measurements on bulk CuHCF electrodes found that its cycle life during Na^+ cycling was much worse than during K^+ cycling. NiHCF appeared to be one of only a few Prussian Blue analogues that are stable during repeated sodium ion intercalation.

10.2 Physical Properties of Nickel Hexacyanoferrate

On this basis, the co-precipitation method was adapted to produce bulk quantities of NiHCF. In this case, Ni^{2+} was used as a precursor instead of Cu^{2+} , and the reaction was performed at 70°C to improve the crystallinity (Fig. 18b).¹⁵¹

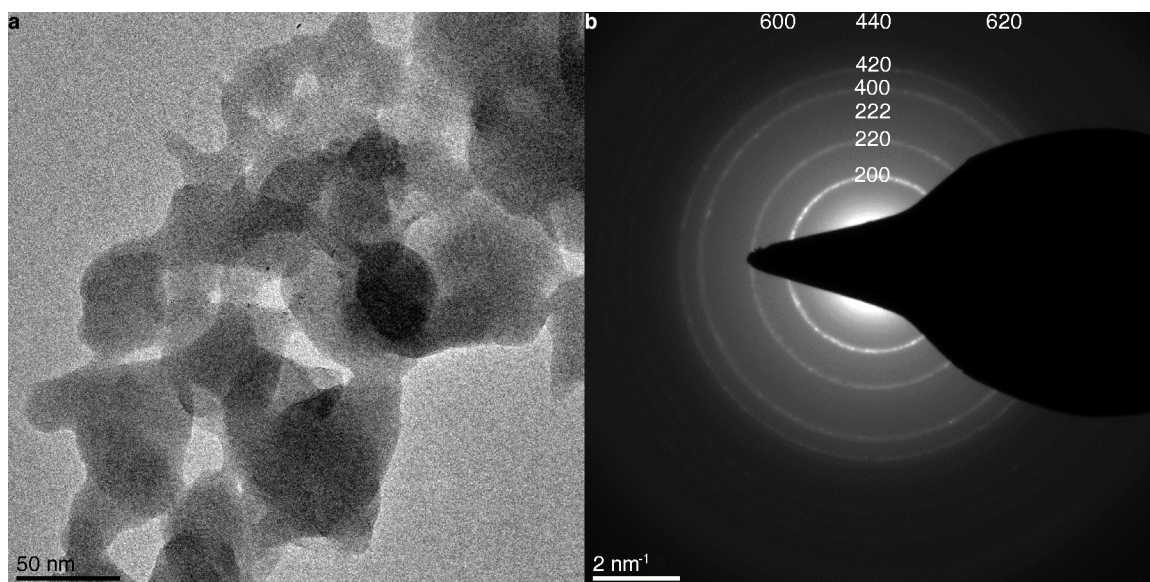


Figure 24: (a) TEM of NiHCF shows nanoparticles about 50 nm in size. (b) The fully indexed TEM electron diffraction pattern of NiHCF matches the spectrum obtained by XRD (Fig. 16a).

Much of the data gathered during physical characterization of NiHCF was presented in Chapter 8 to illustrate aspects of the co-precipitation synthesis method. All other processing steps for physical characterization and electrode preparation of NiHCF in aqueous cells were the same as stated in Chapter 9 for CuHCF electrodes. The XRD spectrum of NiHCF (Fig. 17a, 18b) was found to be phase pure, and the lattice parameter of freshly synthesized NiHCF was found to be 10.2 Å. Using SEM, NiHCF was found to consist of 50-100 nm grains (Fig 17b-c). TEM of NiHCF performed with Matthew T. McDowell confirmed this result (Fig 24a), and the electron diffraction pattern (Fig. 24b) matched the diffraction spectrum acquired using XRD.¹⁵¹

10.3: Electrochemical Properties of Nickel Hexacyanoferrate

Electrochemical characterization of NiHCF was performed using galvanostatic cycling, with the same experimental setup as previously described for the study of CuHCF (Chapter 9).¹⁵¹ A 1 M NaNO₃/0.01 M HNO₃ electrolyte was used during the study of Na⁺ intercalation into NiHCF. The potential profiles of NiHCF during its reaction with Na⁺ and K⁺ are plotted in Fig. 25a and 25b, respectively. The reaction of NiHCF with Na⁺ is centered at 0.59 V vs. SHE, while its reaction with K⁺ is centered at 0.69 V vs. SHE. The latter potential is about 250 mV lower than the reaction potential of CuHCF with K⁺. As discussed in Chapter 7, hexacyanoferrate is electrochemically active in many Prussian Blue analogues, and its reaction potential will generally be higher in materials that contain smaller, higher-valence P-site cations. The crystal ionic radius of Ni²⁺ is nearly 10% larger than that of Cu²⁺, so this general trend holds for NiHCF and CuHCF. Though the reaction potentials of NiHCF with Na⁺ and K⁺ are different, its capacity retention during high rate cycling is virtually identical for the two insertion species. Of the maximum capacity of 59 mAh/g observed for both Na⁺ and K⁺ cycling at C/6, 67% is retained at a 41.C rate (Fig. 25c). Though the high rate performance of NiHCF is somewhat lower than that observed for CuHCF during K⁺ cycling, it is still far better than any previously reported Na⁺ insertion electrode.

The potential hystereses observed during the cycling of NiHCF with K⁺ were smaller than those observed during cycling with Na⁺. At a 0.83C rate, the hysteresis at a half-charge state was 8 mV during K⁺ cycling, and 12.7 mV during cycling with Na⁺. The voltage hystereses during reaction with both insertion species increased linearly with current density, but the rate of increase was greater for Na⁺ insertion. At a 41.7C rate, the half-charge hysteresis was only 106 mV during cycling with K⁺, but 178 mV in the case of Na⁺ cycling. Impedance spectroscopy was not performed on NiHCF, so the mechanism for the lower potential hysteresis during K⁺ cycling has not yet been determined. It is possible that differences in the geometry of the flooded cells accounted for the difference in the hystereses, as their ohmic behavior suggests that the resistance of the electrolyte and current collectors dominated the impedance of the cell.

As in the case of CuHCF, low potential hysteresis during cycling at high current densities will allow NiHCF to achieve high energy efficiency in full cells. The same hypothetical 1 V cell with a reversible anode as described in Chapter 3.8 can achieve 98-99% energy efficiency at a 0.83C rate. At a

much higher 41.7C rate, energy efficiencies of 83% and 90% during Na^+ and K^+ should also be possible.

NiHCF shows perfect reversibility during extended electrochemical cycling. When cycled with Na^+ between 0.4 and 0.8 V vs. S.H.E., zero capacity loss is observed after 5,000 deep discharge cycles at a 8.3C rate (Fig. 25d). In comparison, the recently reported $\text{Na}_4\text{Mn}_9\text{O}_{18}$ electrode was shown to be stable for only 1,000 cycles, and had much lower specific capacity (about 30 mAh/g). During cycling with K^+ , no capacity loss is observed during the first 1,000 cycles, after which capacity is lost at a rate of 1.75% for each additional 1,000 cycles. Coulomb efficiencies of 99.7% to 99.9% were observed during cycling with both Na^+ and K^+ . The reason for the more rapid decrease in capacity during extended cycling of K^+ could not be determined from electrochemical measurements alone.

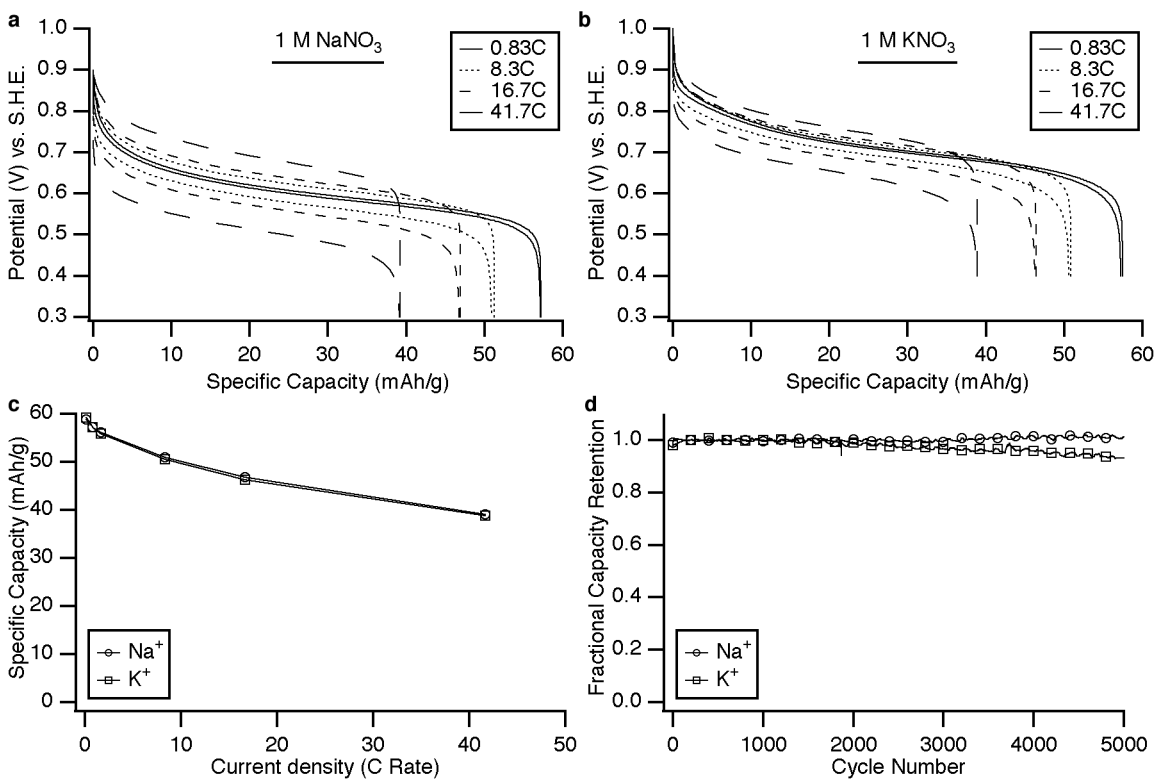


Figure 25: (a) and (b) Galvanostatic cycling of NiHCF at various rates in 1 M NaNO₃ and 1 M KNO₃, respectively. (c) The capacity retention of NiHCF at high current densities is nearly identical during Na^+ and K^+ cycling. (d) NiHCF has zero capacity loss after 5,000 cycles with Na^+ at 8.3C, but after the first 1,000 cycles, loses capacity at a rate of 1.75%/1,000 cycles during cycling with K^+ .

10.4: Ex-situ X-ray Characterization of Nickel Hexacyanoferrate Electrodes

Ex-situ XRD measurements were performed on NiHCF at various charge states during Na^+ and K^+ cycling. NiHCF has poorer crystallinity than CuHCF, even when synthesized at 70° C instead of room temperature, so a more careful procedure for setting the charge state of each electrode was employed in an

effort to conclusively establish the relationship between the lattice parameter of NiHCF and its charge state.

After ten deep-discharge cycles at 5C, NiHCF electrodes were partially charged at 1C. The duration of the final charge was determined by the desired final charge state for each electrode, and the measured specific capacity of each electrode during the initial cycling. An extremely small shift in the diffraction spectrum of NiHCF to lower angles was observed during Na^+ cycling (Fig. 26a). During K^+ cycling, however, a much larger peak shift was observed (Fig. 26b). These peak shifts corresponded to a lattice strain of 0.18% during Na^+ cycling, and 1.1% during K^+ cycling.

NiHCF has poorer crystallinity than CuHCF, and structure refinement using the X'Pert Highscore Plus software package did not yield accurate lattice parameters. Instead, peak positions were found by modeling each peak with Gaussian functions using the Igor Pro software package. These peak positions were converted to interplanar spacings using Bragg's Law, and those in turn were used to find the lattice parameter using simple geometry. The lattice parameters plotted in Fig. 26c are the mean for at least seven diffraction peaks for each sample. The error bars show a single standard deviation spread about each mean lattice parameter. De-intercalation of K^+ results in similar strains in both CuHCF (1%) and NiHCF (1.1%). Lower strains appear to be loosely correlated to cycle life, as the lowest strain was observed during Na^+ cycling of NiHCF, which was found to be completely stable for 5,000 cycles.

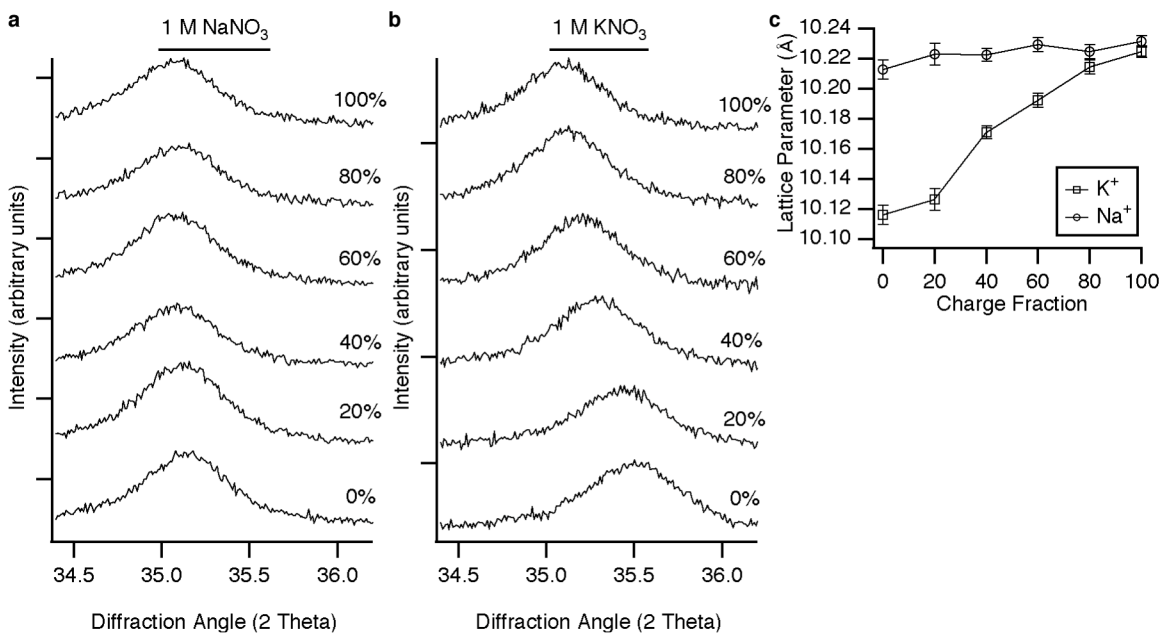


Figure 26: (a) The 400 peak of NiHCF shifts only slightly to lower diffraction angles during charging in Na^+ electrolyte, and a much larger peak shift is observed during charging in K^+ electrolyte (b). This corresponds to a much larger strain during cycling with K^+ than with Na^+ (c).

A comparison of the sizes of the inserted species with the sizes of the A sites and the channels between them can help explain the difference between the strains during Na^+ and K^+ cycling. In aqueous solutions, cations such as Na^+ and K^+ are hydrated, and their hydrated radii are much larger than their crystal ionic

radii. As discussed in Chapter 3.4, the channel radius is about 1.6 Å, and the A site radius is about 2.5 Å. In comparison, the crystal ionic radii of Na⁺ and K⁺ are 1.12 and 1.52 Å, respectively, and their hydrated Stokes radii are 2.76 Å and 1.88 Å, respectively.^{64, 194} During reduction of hexacyanoferrate, the Fe-C bond shortens by 0.05 Å. But, if the effective size of insertion ions occupying the A sites are larger than the size of site, as is the case for hydrated Na⁺, the presence of these ions should limit the negative strain that typically occurs during hexacyanoferrate reduction. This is exactly what is observed, as Na⁺ results in only a 0.18% decrease in lattice parameter, even though a 1% decrease is expected from the Fe-C bond contraction. It must be noted that the hydration state and effective size of the insertion species in the A sites of the Prussian Blue structure remains unknown. Hydrated Na⁺ is much too large to fit through the channels between adjacent A sites, so it is possible that some de-solvation and re-solvation occurs as insertion ions move through the structure. However, the details of this process cannot be determined from electrochemical testing and XRD alone.

Chapter 11: The Effects of the Identity of the Insertion Ion Species

11.1: Historical Background

The vast majority of the studies of the electrochemical properties of Prussian Blue analogues, whether for electrochromic devices or for batteries, used an aqueous KCl electrolyte, and K^+ was inserted into the crystal structure of the electrode. The open framework structure of Prussian Blue does allow other ions to be inserted, most notably Na^+ . In a few isolated instances, efforts to use other insertion ions, including alkali, alkaline earth, and others have been examined.^{68-69, 139, 141} Itaya et al published the most fruitful of these studies in 1982, just after their early demonstration of a Prussian Blue thin film with ultra-long cycle life.⁶⁸ They found that NH_4^+ , K^+ , Cs^+ , and Rb^+ could be cycled at least 1,000 times with only a marginal decrease in the capacity of the electrode. But, the cycling of Li^+ , Na^+ , and Ba^{2+} resulted in rapid destruction of the electrode in 10 cycles or fewer. They noted that the hydrated Stokes radii of the ions capable of reversible intercalation were less than or about equal to the radius of the channel between adjacent A sites in the structure. Ions with smaller crystal ionic radii generally have larger hydrated radii in aqueous solutions due to the formation of a robust hydration shell. Thus, aqueous Li^+ has a larger effective radius than aqueous Na^+ , which has a larger effective radius than aqueous K^+ , and so forth.¹⁹³ The fact that Prussian Blue showed long cycle life only for insertion ions with small hydrated radii suggested that those ions remained at least partially solvated after entering the structure. However, at about the same time, thin films of NiHCF were shown to reversibly cycle Na^+ and Li^+ , which have hydrated Stokes radii much larger than the diameter of the channel between the A sites.^{139, 141} The discord among these early studies, along with the preliminary evidence that NiHCF could operate as a sodium ion battery electrode with long cycle life provoked a more complete examination of the effect of the identity of the insertion species on the behavior of Prussian Blue analogue electrodes during the work for this thesis.¹⁵²

11.2 Effects of Insertion Species on Copper Hexacyanoferrate and Nickel Hexacyanoferrate

Using the same experimental techniques as described in Chapter 9 and 10, the electrochemical properties of CuHCF and NiHCF were examined in aqueous electrolytes containing Li^+ , Na^+ , K^+ , and NH_4^+ .¹⁵² As in previous work, cyclic voltammetry and galvanostatic cycling were performed to determine the reaction potential, rate capability, and cycle life of these electrode materials with each insertion species.

During cyclic voltammetry, CuHCF has a single, sharp reaction with both K^+ and NH_4^+ (Fig. 27a). These reactions are centered at 0.93 V and 1.02 V vs. SHE, respectively. Much more complicated behavior was observed during cyclic voltammetry of CuHCF with Li^+ and Na^+ . Three broad reactions were observed between 0.4 V and 1.2 V, while the strong reaction with Na^+ at 0.77V was followed by a weaker reaction near 1.0 V. Cyclic voltammetry of NiHCF (Fig. 28a) showed that like CuHCF, it had a single sharp reaction with K^+ , centered at 0.69 V. However, unlike CuHCF, NiHCF also had a sharp reaction with Na^+ ,

at 0.59 V, but its reaction with NH_4^+ at 0.75 V was much broader. Finally, NiHCF had a broad reaction with Li^+ that was centered at 0.37 V, but that had a wide potential range, and a second, weaker reaction was observed near 0.7 V. It is clear that though both CuHCF and NiHCF react with K^+ by a single insertion mechanism, they have dramatically different behavior for all other intercalants.

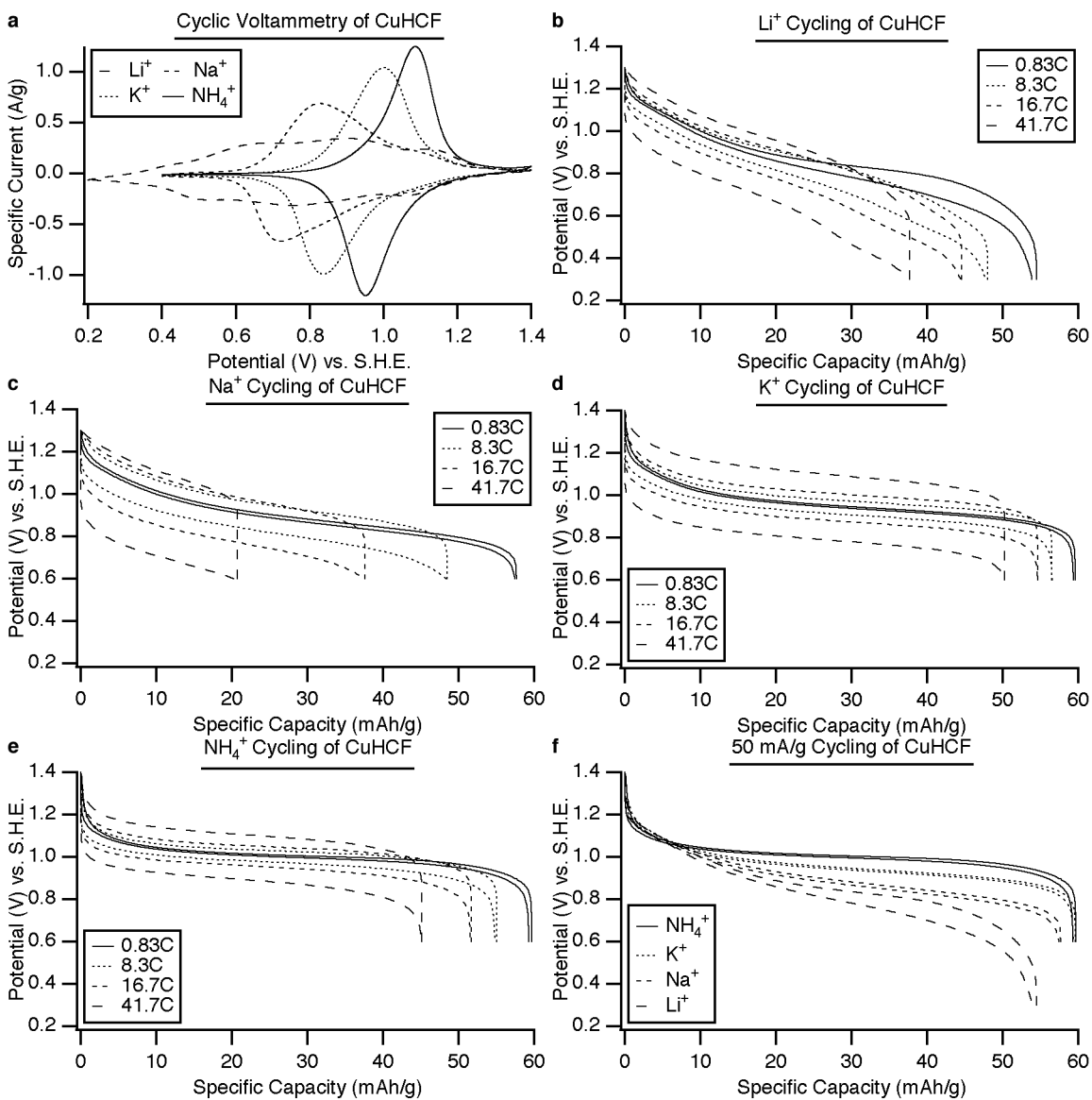


Figure 27: (a) Cyclic voltammety of CuHCF. (b-e) Galvanostatic cycling of CuHCF at various rates with Li^+ , Na^+ , K^+ , and NH_4^+ , respectively. (f) Galvanostatic cycling of CuHCF at 50 mA/g (0.83C) in all four electrolytes.

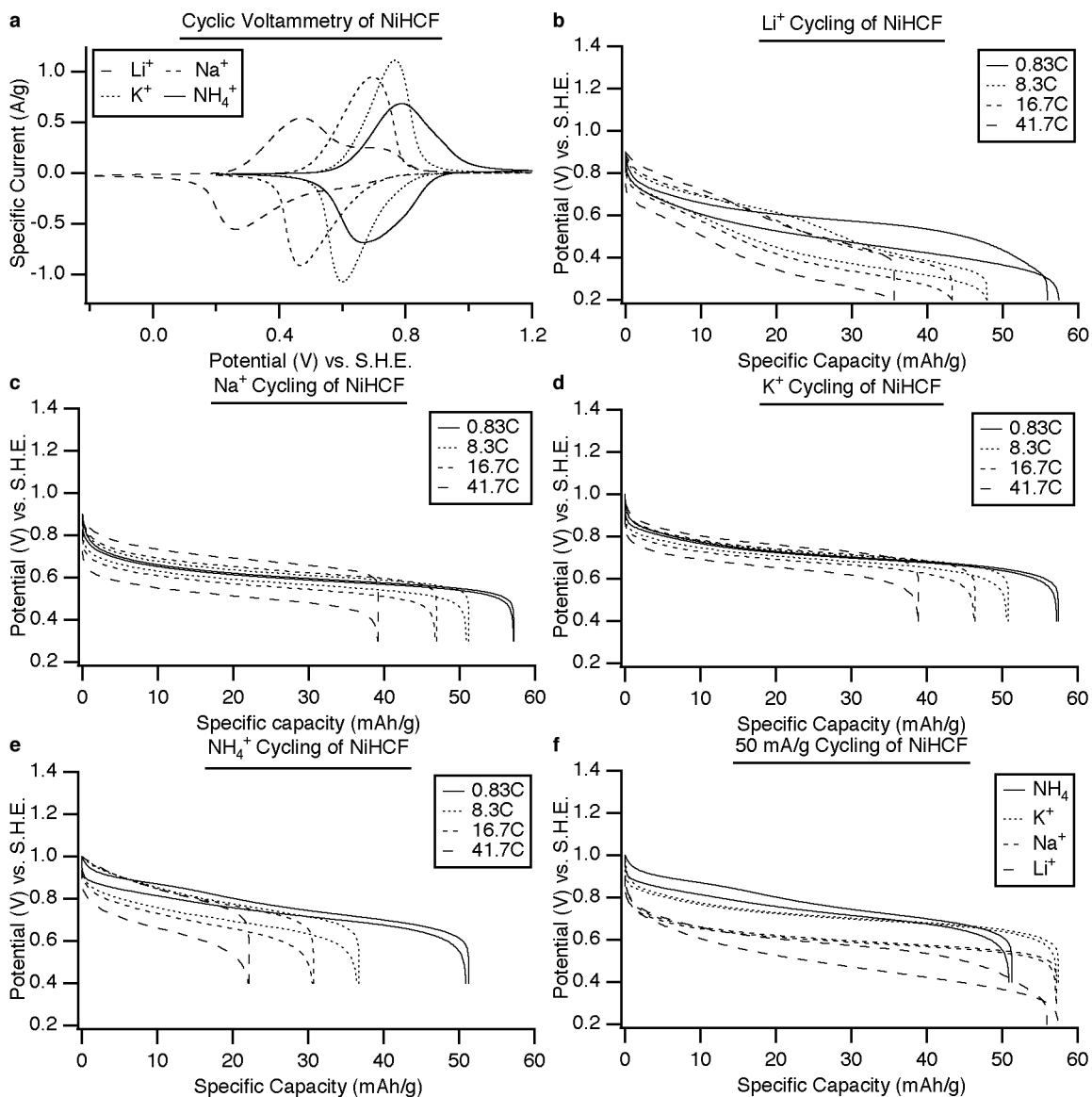


Figure 28: (a) Cyclic voltammety of NiHCF. (b-e) Galvanostatic cycling of NiHCF at various rates with Li⁺, Na⁺, K⁺, and NH₄⁺, respectively. (f) Galvanostatic cycling of NiHCF at 50 mA/g (0.83C) in all four electrolytes.

Cyclic voltammety provided information about the reaction potentials of CuHCF and NiHCF with various insertion species, but it does not represent their behavior as battery electrodes, for batteries typically operate at relatively constant potentials and currents (near a steady state). For this reason, galvanostatic measurements on CuHCF and NiHCF were also performed, over a wide range of current densities between ± 10 mA/g (0.83C) and $\pm 2,500$ mA/g (41.7C, Fig. 27b-e and Fig. 28b-e). Both CuHCF and NiHCF were found to have specific capacities of up to 60 mAh/g, in agreement with previous characterization (Chapter 9-10). During galvanostatic cycling of Li⁺, both CuHCF and NiHCF show complex behavior over a wide potential range. However, they each have a single, S-curve potential profile

during the insertion of both Na^+ and K^+ , indicating that they react with those intercalants by a single-phase solid solution reaction. The same was true for the cycling of NH_4^+ with CuHCF, though its reaction with NiHCF showed a shoulder indicative of a second reaction at about 0.9 V vs. SHE. At a 0.83C cycling rate, CuHCF and NiHCF fully reacted with Na^+ , K^+ , and NH_4^+ in narrow potential ranges of only about 0.3-0.4 V. A much wider potential range was needed for their reaction with Li^+ , for it spanned 0.7 V for CuHCF and 0.5 V for NiHCF. These results are consistent with previous work showing that NiHCF thin films had sharper reactions with K^+ and Na^+ than with Li^+ . On the other hand, films of Prussian Blue were found to react more sharply with K^+ than with NH_4^+ during reduction to Everitt's Salt, contrary to the result observed here for CuHCF.

Both cyclic voltammetry and galvanostatic cycling showed that for both CuHCF and NiHCF, the reaction potential increases for heavier insertion ions that have smaller hydrated radii (Fig. 27a, f, 28a, f, and 29e). During galvanostatic cycling, the potential of CuHCF at a half-charge state during reaction with NH_4^+ , K^+ , Na^+ , and Li^+ was 1.0 V, 0.95 V, 0.88 V, and 0.82 V vs. SHE, respectively. The same trend of higher reaction potentials for heavier insertion species was observed for NiHCF, which reacted with NH_4^+ , K^+ , Na^+ , and Li^+ at 0.75, 0.70, 0.59, and 0.53 V, respectively. If the insertion ions do indeed remain at least partially solvated while inside the structure, this trend to higher potentials for smaller ions is intuitive. The potential of an electrochemical reaction is related to the Gibbs Free Energy of the analogous chemical reaction by the expression $\Delta G = -nFV$. Insertion species much too large for an interstitial site will exert stress on the surrounding atoms in the structure, making the free energy of the reaction less negative, which lowers the reaction potential. McCargar and Neff presented more detailed discussion of the thermodynamics of the insertion of various intercalants, and they also observed the same trend to higher potentials for heavier intercalants for Prussian Blue as is seen here for CuHCF and NiHCF. Previous study of several alkali insertion ions in NiHCF films found behavior similar to that observed here. However, vanadium hexacyanoferrate films were found to have nearly the same reaction potentials during cycling of Li^+ , K^+ , and NH_4^+ . This last result shows that the trend of higher reaction potentials for smaller, heavier intercalants that is observed for CuHCF, NiHCF, and Prussian Blue may not be valid for other Prussian Blue analogues.

Both CuHCF and NiHCF were found to retain much of their discharge capacities during high rate cycling (Fig. 29a-b). CuHCF was found to have poor capacity retention during high rate cycling of Na^+ , as it retained only 34% of its maximum capacity when cycled at a 41.3C rate. In comparison, it retained 84% of its maximum capacity during K^+ cycling at 41.3C. At the same rate, specific capacities of 75% and 65% were observed during cycling of NH_4^+ and Li^+ , respectively. It is unclear why the rate capability of CuHCF during cycling with Na^+ was so poor in comparison to its performance with other insertion ions. Different high rate behavior was observed for NiHCF. Though it retained 66% of its capacity at 41.3C during the cycling of either Na^+ or K^+ , it retained only 39% and 58% during its reactions with NH_4^+ and Li^+ , respectively. It appears that Li^+ can be easily cycled in CuHCF, but not in NiHCF; the opposite is true for Na^+ , which cycles well in NiHCF, but not in CuHCF. The differences in the high rate behavior of CuHCF

and NiHCF are not understood at this time. They have lattice parameters that differ by less than 1%, so the channels and interstices in the structures of the two materials are similar.

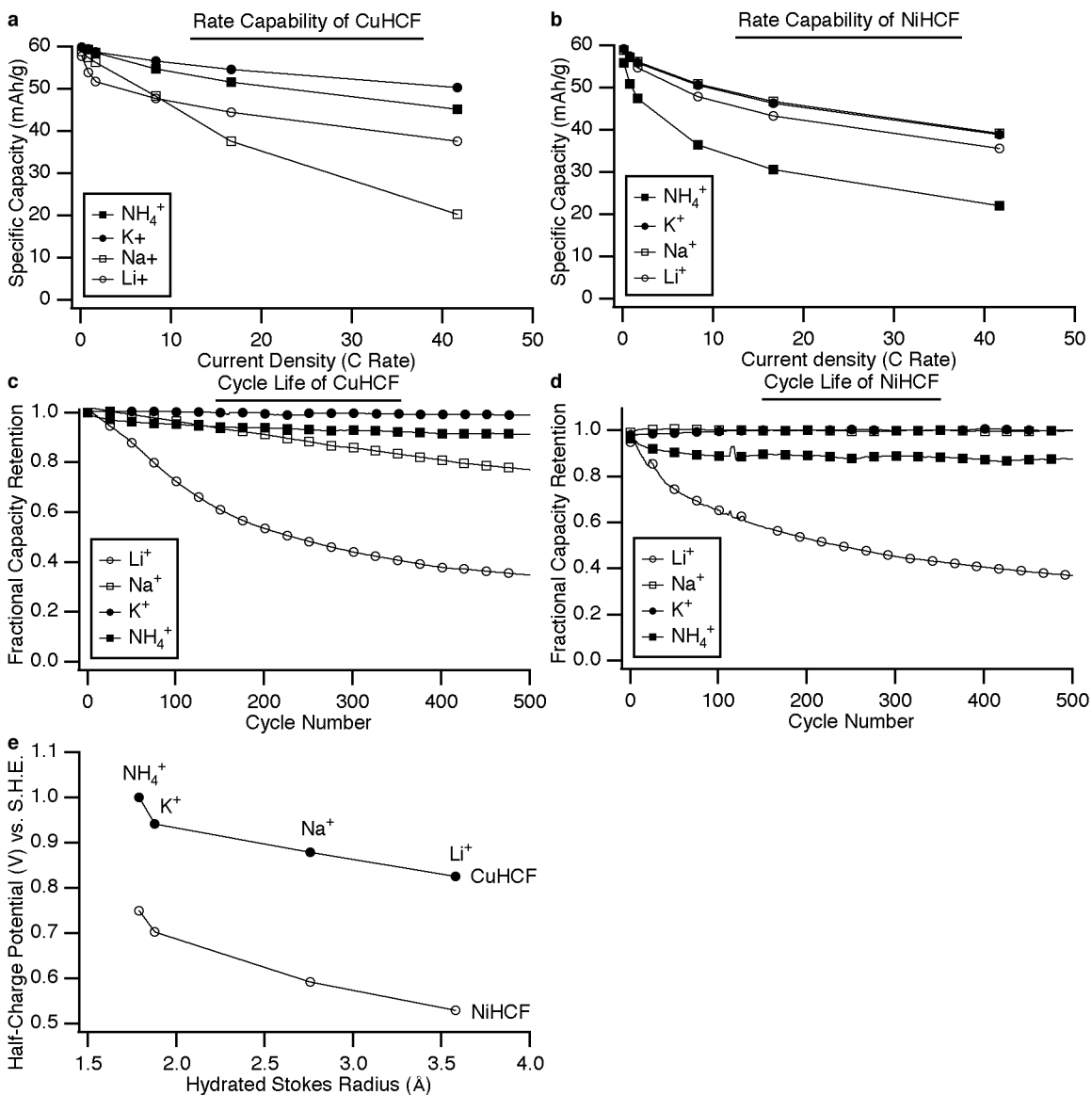


Figure 29: (a-b) Capacity retention of CuHCF and NiHCF, respectively, with Li⁺, Na⁺, K⁺, and NH₄⁺. (c-d) Cycle life of CuHCF and NiHCF, respectively, in the same electrolytes. (e) Reaction potentials of CuHCF and NiHCF as a function of the hydrated radius of the intercalant.

Extended cycling of both CuHCF and NiHCF was performed for all four insertion ions, at a 8.3C rate. CuHCF was especially durable during reaction with K⁺, for it retained 99% of its capacity after 500 deep discharge cycles (Fig. 29c). It was less stable during cycling with NH₄⁺, Na⁺, and Li⁺, retaining 91%, 77%, and 35%, respectively, of its initial specific discharge capacity after 500 cycles. NiHCF had zero measurable capacity loss after 500 cycles of either K⁺ or Na⁺ (Fig. 29d). Its durability during cycling with

NH_4^+ was similar to that of CuHCF, for it retained 88% of its initial capacity after 500 cycles. But, it suffered severe capacity loss during reaction with Li^+ . The electrolyte was found to have turned bright yellow, indicating that Li^+ insertion caused some of the hexacyanoferrate in NiHCF to dissolve. The mechanism for capacity fading was therefore related to the loss of electrode mass to dissolution, at least in the case of Li^+ cycling. The solubility of CuHCF and NiHCF may depend on the insertion species. For cases in which extremely stable cycling was observed, such as the reaction of CuHCF with K^+ , any trace solubility is masked by the presence of the counter electrode, the large mass of which can partially dissolve to reach the solubility limit of the material. But, in the case of Li^+ insertion, the working electrodes became much more unstable, and enough hexacyanoferrate was present in the electrolyte to make it bright yellow. No such color change was observed during cycling with K^+ , Na^+ , or NH_4^+ . Thus, CuHCF and NiHCF are stable enough for use as electrodes for those insertion species, but not for lithium..

The hydrated Stokes radius of Li^+ is about 3.6 Å, much larger than the radius of the A site in the Prussian Blue structure.¹⁹³ Because Li^+ has such a small crystal ionic radius, water coordinates to it quite tightly. Unless substantial de-solvation occurs, the Li^+ inserted into the Prussian Blue structure will exert tensile stress on the bonds in the framework around the A site. Partial dissolution of CuHCF and NiHCF during cycling with Li^+ may be readily explained by the instability induced by the misfit of large, hydrated Li^+ into the smaller A sites. Instability of the framework structure upon the insertion of a large, misfitting intercalant also corroborates the trend noted above: lower reaction potentials are observed for larger inserted cations (Fig. 29e).

11.3 Final Comments on Insertion Ion Radii

In the above discussion, it was assumed that the insertion ions were hydrated, and therefore, their aqueous Stokes radii, rather than their crystal ionic radii, are applicable. In reality, these insertion ions may not pass through the channels in the Prussian Blue structure with complete hydration shells. As an example, consider K^+ insertion: the radius of the channel between adjacent A sites is 1.6 Å, nearly the same as the crystal ionic radius of K^+ , so it cannot retain its hydration shell while passing through the channel. However, the crystal ionic radius of K^+ is much smaller than the radius of the A site itself (2.51 Å), so K^+ likely coordinates with the zeolitic water already present in the structure.

When the study on the effects of different insertion ions on CuHCF and NiHCF was performed, the convention of treating the insertion ions as partially hydrated, with the same effective radius as their aqueous Stokes radius was adopted. This convention was originally used by Itaya and colleagues in a 1982 paper in which they showed that thin films of Prussian Blue could react reversibly only with insertion species with aqueous Stokes radii smaller than the channel radius.⁶⁸

The Stokes radii presented in this thesis are not the commonly cited textbook values because for some insertion species, they are anomalously small. For instance, the most commonly reported aqueous Stokes radius for K^+ is 1.25 Å, only about 80% of its crystal ionic radius!¹⁹³ This is a non-physical result that comes from the way in which Stokes radii are calculated. They are found by using the drag force on a

sphere in a viscous fluid (Stokes Law) and the Einstein relation for the diffusion of particles. Though valid for particles and macroscopic objects in solution, this method obviously does not result in accurate size estimates for individual ions.

As discussed in a seminal 1991 paper by Pau et al, the drag force on individual ions in solution is not a simple extrapolation of those on macroscopic spherical objects.¹⁹³ In that paper, the authors present a derivation of the drag force on ions using more appropriate boundary conditions. The result is that the aqueous Stokes radii they calculate are larger than the previously reported values by a factor of 3/2. Though it remains unclear whether these new values have physical relevance, at the very least, they are not smaller than the crystal ionic radii of bare, unsolvated cations.

For this reason, the more recently reported, values for the Stokes radii are used when discussing the sizes of insertion ions in the Prussian Blue structure, and the data in Fig. 29e are shown with respect to those values.

In summary, it is likely that intercalated ions inside the Prussian Blue structure have at least a partial hydration shell while they occupy the A sites, but during their transport through the channels from one A site to the next, some de-solvation may occur. The purpose of this section of this chapter was to clarify this point and to explain the origin of the values used for the aqueous Stokes radii of the insertion ions.

Chapter 12: Tuning the Reaction Potential of Prussian Blue Analogues

12.1 Synthesis of Copper-Nickel Hexacyanoferrate Solid Solutions

Discussion of Prussian Blue analogues has so far considered only “pure” phases, in which a single species occupies each site in the framework structure. For instance, Cu^{2+} occupies the P sites in CuHCF, while Ni^{2+} occupies them in NiHCF. The framework structure of Prussian Blue accommodates a vast assortment of constituent elements at either the P or R sites, and furthermore, a single species need not occupy all of one type of site. Simultaneous, partial occupancy of the A, P, and R sites has been previously demonstrated in cadmium-iron hexacyanoferrate, nickel-iron hexacyanoferrate (NiFeHCF), and copper-nickel hexacyanoferrate-hexacyanocobaltate.¹⁶⁶⁻¹⁶⁹ As discussed above, pure CuHCF has a higher electrochemical potential than pure NiHCF. It is interesting to consider the properties of an intermediate CuNiHCF composition: does it have a single electrochemical reaction potential in between those of the pure materials, or does it have two reaction potentials, one near that of CuHCF, and the other near that of NiHCF? A more fundamental formulation of this question is: in a mixed Prussian Blue analogue such as CuNiHCF, is there a single, mixed phase containing both Cu and Ni at the P sites, or are there two pure CuHCF and NiHCF phases that are intimately mixed?

In an effort to answer this question, CuNiHCF was synthesized using the standard procedure described in Chapter 3.6. In this particular case, the metal salt precursor solution contained desired quantities of both $\text{Cu}(\text{NO}_3)_2$ and $\text{Ni}(\text{NO}_3)_2$. For example, equal amounts of $\text{Cu}(\text{NO}_3)_2$ and $\text{Ni}(\text{NO}_3)_2$ were included in the precursor solution if a product containing a 1:1 ratio of Cu and Ni was desired. Previous syntheses of CuHCF were performed at room temperature, but those of NiHCF were performed at over 70° C. In this study, all syntheses, including that of pure CuHCF, were performed at 70° C. All other processing steps for material and electrode preparation were the same as described above. ICP-MS of the CuNiHCF samples found that Cu was incorporated preferentially (Table 2). This result is somewhat counterintuitive, as pure NiHCF precipitates more readily than does pure CuHCF.

Table 2: Cu:Ni Contents of Precursor Solutions and Their CuNiHCF Products

Precursor Cu:Ni (Prepared)	CuNiHCF Cu:Ni (ICP-MS)
1:0	1:0
75:25	77:23
50:50	56:44
25:75	29:71
0:1	0:1

12.2 Physical Characterization of Copper-Nickel Hexacyanoferrate Solid Solutions

Physical characterization of CuNiHCF using TEM determined that all of the materials were comprised of polydisperse, 20-50 nm particles with good crystallinity. CuHCF, NiHCF, and intermediate CuNiHCF materials could not be distinguished from TEM imaging or diffraction spectra alone. However, energy dispersive X-ray spectroscopy (EDS) could distinguish the various materials. For example, CuHCF was found to contain Cu and Fe, but not Ni; NiHCF was found to contain Ni and Fe, but not Cu, and CuNiHCF was found to contain Cu, Ni, and Fe (Fig. 30). This result matched that of the ICP-MS chemical analysis.

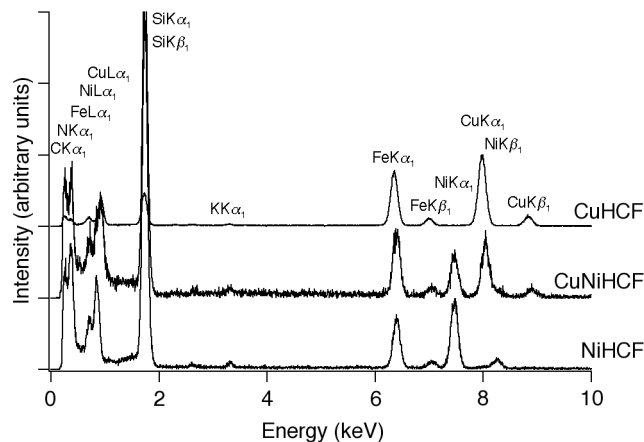


Figure 30: Wide-area TEM EDS of CuHCF, NiHCF, and CuNiHCF. Only Cu and Fe are observed in CuHCF, only Ni and Fe are observed in NiHCF, but Cu, Ni, and Fe are all observed in intermediate CuNiHCF compositions.

Physical characterization of CuNiHCF compositions was also performed using XRD. All samples were found to be phase pure and had the FCC Prussian Blue framework structure (Fig. 31a). A shift in the positions of diffraction peaks to higher angles with increasing Cu content was observed (Fig. 31b), which corresponds to a decrease in lattice parameter (Fig. 31c). Pure CuHCF has a lattice parameter that is about 0.7% smaller than that of pure NiHCF. The consistent decrease in lattice parameter with increasing Cu content is indicative of a single phase, in which Cu and Ni both occupy the same sites in the structure. Linear changes in lattice parameter with composition are consistent with Vegard's Law, and are commonly observed in alloys of metals and of semiconductors. The change in lattice parameter with Cu content was not perfectly linear, however. The lattice parameters of Prussian Blue analogues also depend on their charge states. CuHCF has such a high reaction potential that it is spontaneously partially reduced during synthesis. On the other hand, NiHCF has a lower reaction potential, and is stable in water even when fully oxidized. Though the change in lattice parameter with Cu content is not truly linear, the general trend is indicative of a single phase containing both Cu and Ni. Further evidence for this interpretation of the diffraction data is the lack of peak broadening or doublets. A mixture of pure CuHCF and pure NiHCF would result in diffraction spectra in which the low angle peaks are broadened, and at higher angles,

doublets would be resolved. This effect was not observed during diffraction measurements of CuNiHCF, which provides additional evidence of the single-phase nature of these materials.

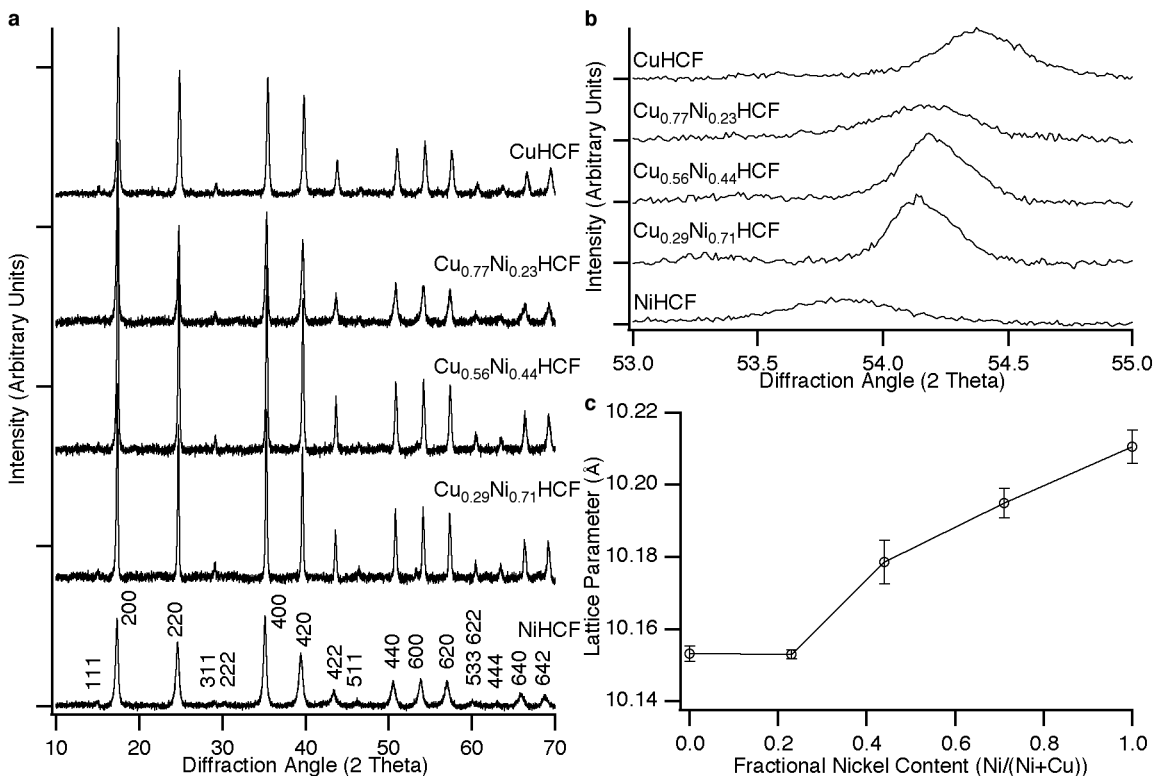


Figure 31: (a) Diffraction spectra of CuNiHCF. (b) A shift in peak positions to lower angles with increasing Ni content was observed, as illustrated by the shift of the 600 peak. (c) The observed peak shifts correspond to an increase in lattice parameter with increasing Ni content. The calculation of the lattice parameter for each sample was performed by Gaussian fitting of 10 high-angle peaks using the Igor Pro software package. The error bars represent one standard deviation from the average lattice parameter found from those peaks.

Previous studies of mixed-composition Prussian Blue analogues commonly relied on a combination of XRD and electrochemical characterization to determine whether or not the mixed composition resulted in a solid solution with multiple species at the P or R sites, or placement of one transition metal species on the P sites, and another on the A sites.¹⁶⁶⁻¹⁶⁹ For example, the lattice parameters of NiFeHCF were found to follow Vegard's law, suggesting that Ni and Fe each partially occupied the P sites.¹⁶⁶ In contrast, more complicated behavior, including the partial occupancy of the A sites by transition metals was observed for some compositions of iron-cadmium and iron-palladium hexacyanoferrates using sophisticated characterization techniques such as Mössbauer spectroscopy and electron spin resonance.¹⁶⁷⁻¹⁶⁸

In no previous study, however, was the homogeneity of a Prussian Blue analogue directly imaged. To conclusively establish whether CuNiHCF contains a mixture of CuHCF and NiHCF, or if it is a single

phase, scanning transmission electron microscopy energy dispersive X-ray spectroscopy (STEM-EDS) mapping was performed on individual CuNiHCF (Cu:Ni = 0.56:0.44) nanoparticles (Fig 32). Cu, Ni, and Fe were found to be distributed homogeneously throughout each nanoparticle, further confirming that CuNiHCF is indeed a single phase that contains Cu and Ni, rather than a mixture of pure phases of CuHCF and NiHCF.

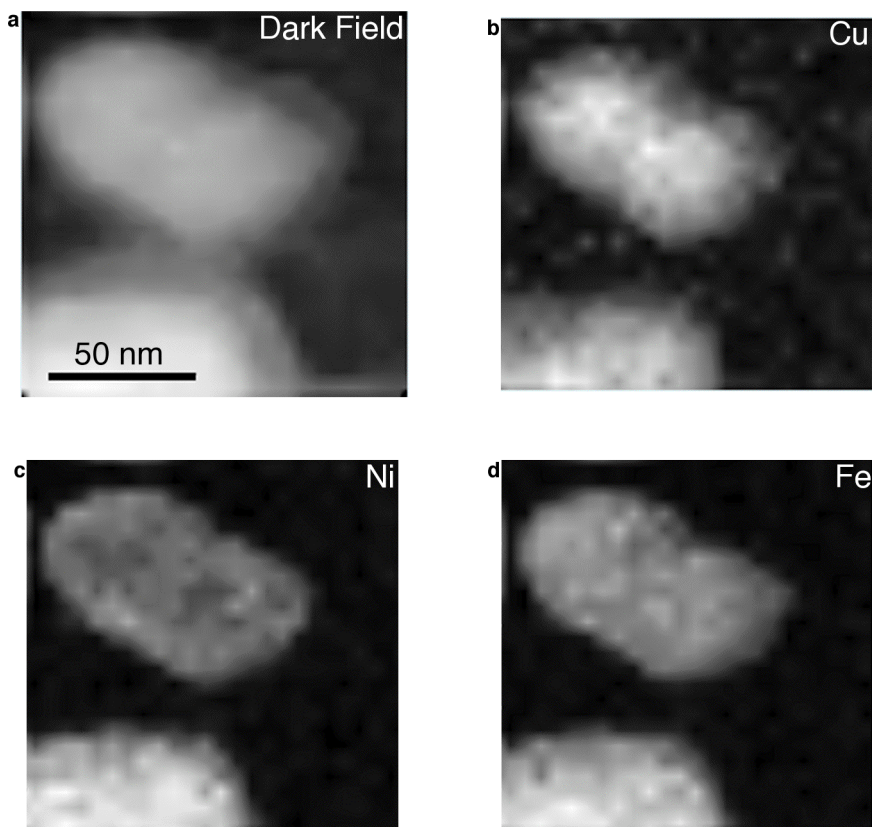


Figure 32: (a) Dark field scanning TEM shows that CuNiHCF is comprised of 50 nm nanoparticles. STEM-EDS mapping reveals that Cu (b), Ni (c), and Fe (d) are all distributed uniformly.

12.3 Electrochemical Characterization of Copper-Nickel Hexacyanoferrate

The electrochemical potentials of Prussian Blue analogues that contain electrochemically active hexacyanoferrate have been shown to depend on the P-site species. Materials that contain P-site transition metal cations with higher ratios of charge to crystal ionic radius typically have higher reaction potentials. Measurement of the electrochemical potentials of CuNiHCF samples with different compositions can therefore provide information not only about the homogeneity of the materials, but also, about which lattice sites Cu and Ni occupy. Galvanostatic cycling was performed on CuNiHCF in electrolytes containing either K^+ or Na^+ at 50 mA/g (Fig. 33a-b). The reaction potentials of CuNiHCF was found to vary nearly linearly with composition, from high potentials for pure CuHCF to low potentials for pure NiHCF (Fig 33c). This

result, along with the results of XRD and STEM-EDS further confirms that CuNiHCF is a single phase of mixed composition, and that Cu and Ni form a substitutional alloy on the P sites in the framework.

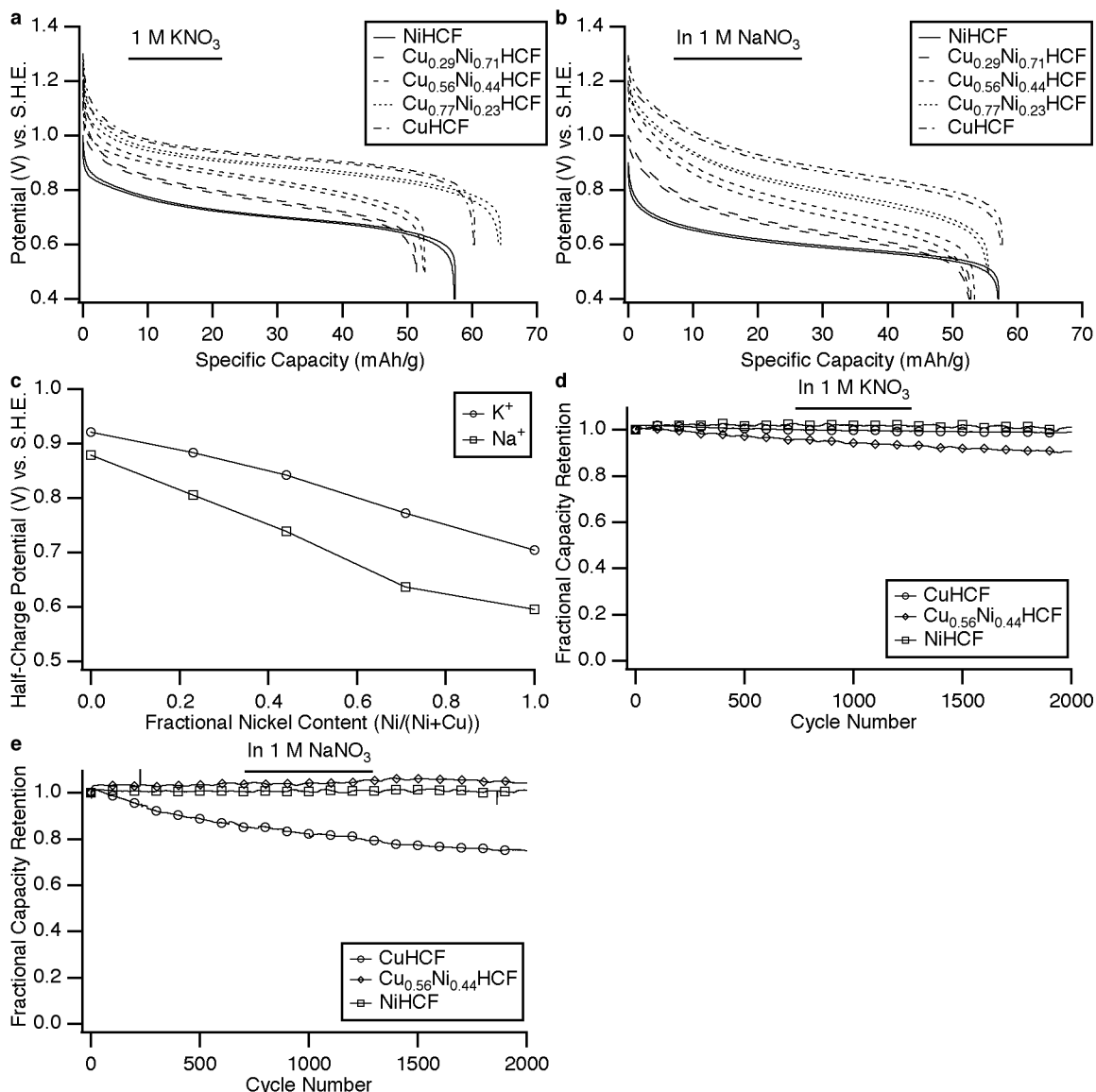


Figure 33: Galvanostatic cycling of CuNiHCF showed a shift in the potential profiles to lower potentials as the Ni content was increased, during both K⁺ (a) and Na⁺ (b) cycling. (c) A linear decrease in reaction potential is observed as Ni content increases. (d) CuHCF and NiHCF have zero capacity loss after 2,000 cycles of K⁺, but CuNiHCF loses about 10% of its capacity. (e) In Na⁺ electrolyte, NiHCF and CuNiHCF are stable, but CuHCF loses 25% of its initial capacity.

Extended cycling of CuNiHCF was performed at 8.3C (Fig. 33d-e). No consistent trends between chemical composition and cycle life were observed for cycling in either K⁺ or Na⁺ electrolytes. During K⁺ cycling, CuHCF and NiHCF had zero capacity loss after 2,000 cycles, while CuNiHCF (Cu:Ni = 0.56:0.44)

gradually lost about 10% of its capacity. During Na⁺ cycling, NiHCF and CuNiHCF had zero capacity loss, but CuHCF lost about 25% of its capacity. The instability of the cycling of CuHCF with Na⁺ was previously observed. It is not clear why CuNiHCF slowly loses capacity during K⁺ cycling, but remains completely stable when reacting with Na⁺. It is likely that the trace solubility of these Prussian Blue analogues depends on their compositions, but no clear trends can yet be established.

12.4 Synthesis and Physical Characterization of Metal-Iron Hexacyanoferrate Solid Solutions

Similar physical and electrochemical characterization was also performed on three other mixed Prussian Blue analogues: copper/iron hexacyanoferrate (CuFeHCF), NiFeHCF, and manganese/iron hexacyanoferrate (MnFeHCF). Physical characterization using XRD found that all three of these materials obeyed Vegard's Law, and their lattice parameters changed approximately linearly with composition (Fig 34). One exception was the limiting case of a high Fe content in NiFeHCF. The reaction potential of pure NiHCF is low enough that it is stable in its oxidized form. Therefore, Berlin Green, and not Prussian Blue, is the pure-Fe member of the NiFeHCF family. Attempts to synthesize crystalline, phase pure Berlin Green by the bulk co-precipitation method were unsuccessful. Prussian Blue was instead included in Fig. 34, but because it contains fully reduced ferrocyanide, its lattice parameter is too small to continue the Vegard's Law trend for NiFeHCF. The known lattice parameter of BG is also included in Fig. 34, and it is consistent with the rest of the data for the NiFeHCF system.¹⁹² This discrepancy did not arise in the cases of CuFeHCF and MnFeHCF because their reaction potentials are high enough to result in spontaneous partial reduction during synthesis. As in the case of CuNiHCF, no XRD peak broadening or doublets were observed for any of these materials. Therefore, it is likely that all three of these materials form homogeneous solid solution phases with a substitutional alloy of multiple transition metal cations randomly distributed on the P sites in the open framework structure.

The morphology of CuFeHCF, NiFeHCF, and MnFeHCF was also found to vary with composition (Fig. 35-36). The most extreme case is the MnFeHCF system, which was previously mentioned in Chapter 8. Pure MnHCF precipitates very slowly, allowing large, faceted grains to nucleate and grow (Fig. 35a). The addition of increasing amounts of Fe³⁺ results in smaller grain sizes, though the MnFeHCF nanoparticles remain faceted (Fig. 35b-d). In the case of MnFeHCF with a Mn:Fe ratio of 75:25, a combination of large, ~1 μm faceted grains and <100 nm nanoparticles is observed. This is an intuitive result, as some of the Fe³⁺ present in solution can rapidly react with Fe(CN)₆³⁻ to form Prussian Blue, while the Mn²⁺ and the remaining Fe³⁺ precipitate more slowly, resulting in large, faceted grains of MnFeHCF. Increasing the amount of Fe³⁺ present during synthesis of MnFeHCF results in smaller grain sizes. In the limiting case of Prussian Blue, precipitation results in nanoparticles smaller than 100 nm, and no larger, faceted grains.

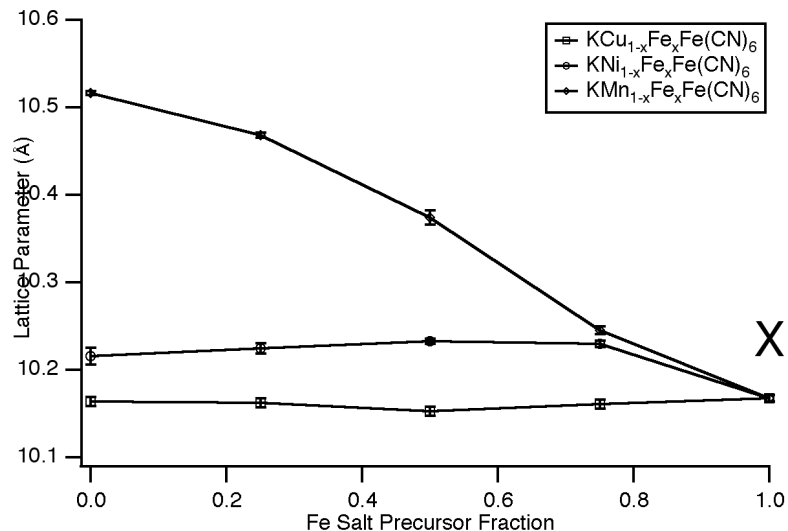


Figure 34: X-ray diffraction of CuFeHCF, NiFeHCF, and MnFeHCF shows that all three materials follow a general Vegard's Law trend, as their lattice parameters almost linearly change with composition. The X denotes the known lattice parameter for Berlin Green (Ref. 192). NiFeHCF is fully oxidized during synthesis, so the limiting case of Ni:Fe = 0:1 is Berlin Green. Error bars are one standard deviation about the calculated lattice parameter for each material.

Composition also influenced morphology in the CuFeHCF system. Pure CuHCF is comprised of 20-50 nm nanoparticles, and despite their high crystallinity, they are not faceted (Fig. 35f). Samples containing both Cu and Fe in ratios of 72:25 and 50:50 are made up of grains that are both larger (200-500 nm) and faceted (Fig. 35g-h). But, further addition of Fe results in material comprised primarily of small nanoparticles, with a few larger grains (Fig. 35i). This result suggests that the presence of both Cu and Fe, without a large excess of Fe, favors the growth of larger grains, rather than the rapid nucleation of small nanoparticles.

In the case of the NiFeHCF system, the addition of Fe dramatically increased the grain size. While pure NiHCF is comprised of 20-50 nm nanoparticles (Fig. 36a), NiFeHCF samples synthesized with Ni:Fe ratios of 75:25, 50:50, and 25:75 are made up of particles of 1 μm or more. Unlike the CuFeHCF and MnFeHCF systems, intermediate compositions of NiFeHCF did not result in faceting. The large particle size of NiFeHCF suggests that the synthesis conditions favored particle growth, rather than the nucleation of new particles. The lack of faceting suggests that particle growth occurred rapidly.

Finally, it must be noted that in the case of MnFeHCF, CuFeHCF, and NiFeHCF, elemental analysis by ICP-MS and other techniques cannot distinguish between P-site and R-site Fe. However, a combination of elemental analysis and Moss Bauer spectroscopy, which is sensitive to the different spin states of the nitrogen and carbon-coordinated Fe would allow determination of the composition of these materials.

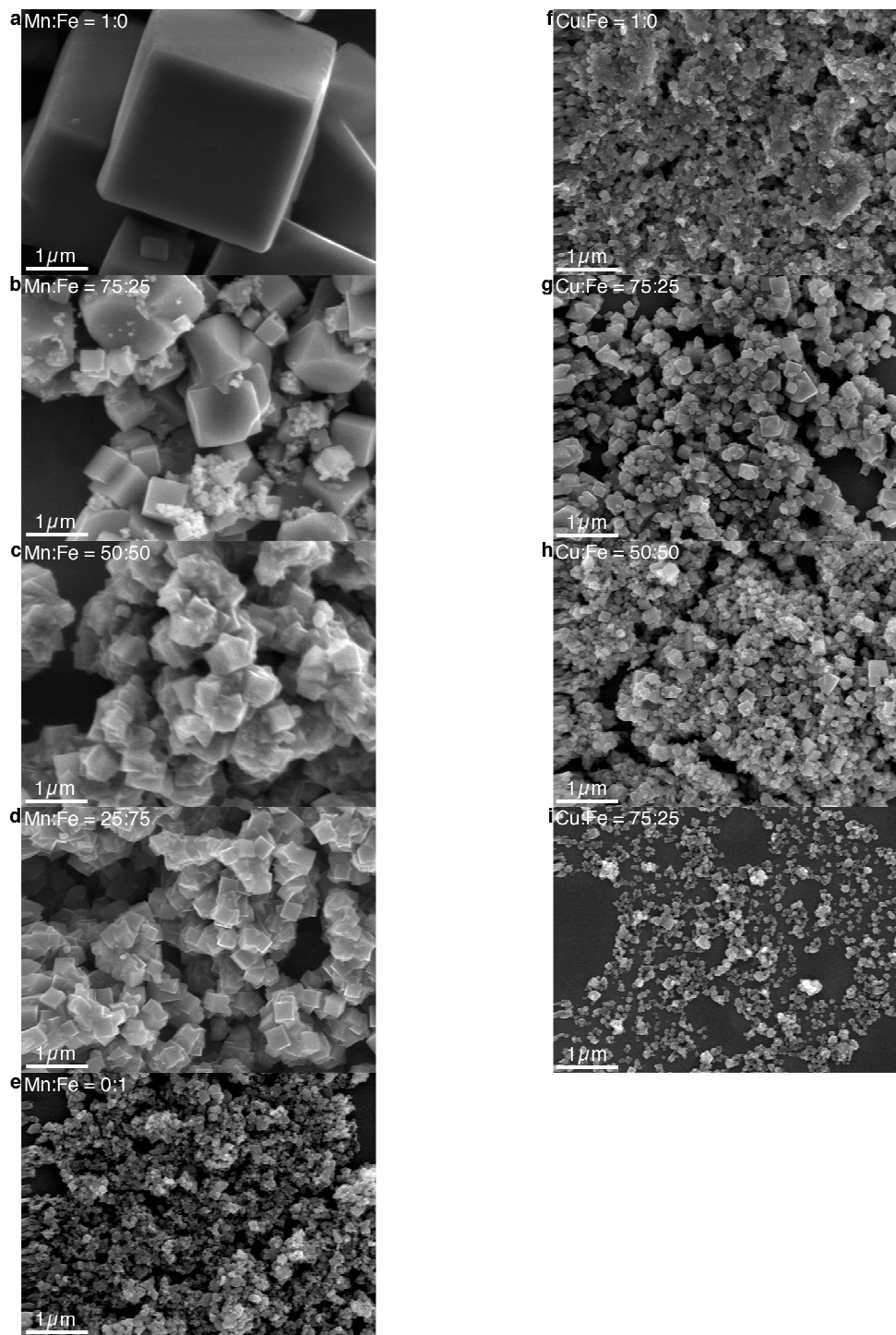


Figure 35: (a-e) SEM of MnFeHCF synthesized from metal salt precursor solutions containing the indicated ratios of Mn to Fe. (f-i) SEM of CuFeHCF synthesized from precursor solutions containing the indicated ratios of Cu to Fe.

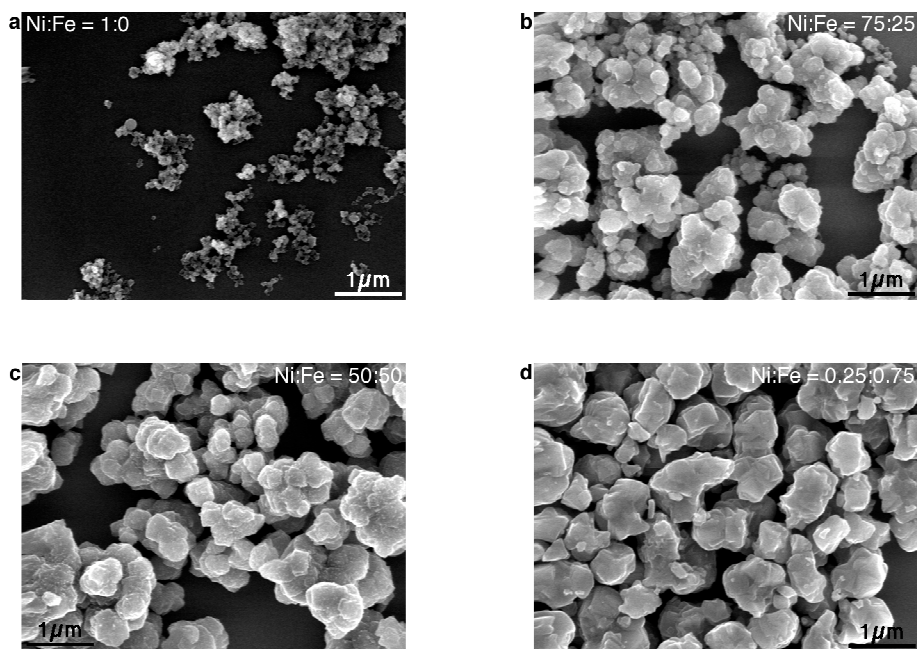


Figure 36: (a-d) SEM of NiFeHCF synthesized from metal salt precursor solutions containing the indicated ratios of Ni to Fe.

12.5 Electrochemical Characterization of Metal-Iron Hexacyanoferrates

Electrochemical characterization of MnFeHCF, CuFeHCF, and NiFeHCF by galvanostatic cycling at 50 mA/g was also performed in both K^+ and Na^+ electrolytes using the techniques described in Chapter 3.6. The non-negligible solubility of MnFeHCF resulted in complex electrochemical behavior and extremely low coulombic efficiency (Fig. 37a-b). The capacity of every MnFeHCF electrode faded rapidly, and the electrolytes turned bright yellow, indicating the presence of dissolved $Fe(CN)_6^{3-}$. Two reaction potentials were observed when MnFeHCF was cycled with either K^+ or Na^+ . This suggests that either the hexacyanoferrate in the structure has two different bonding environments, or that the P site Mn is electrochemically active. In any case, the solubility of MnFeHCF precludes its use as a practical battery electrode, and further examination of its properties was not conducted.

CuFeHCF and NiFeHCF were found to have much more comprehensible electrochemical performance. Both materials have a single S-shaped potential profile at all compositions, indicating that their electrochemical cycling proceeds by the same single-phase insertion mechanism observed for pure CuHCF and NiHCF (Fig. 37c-f). Though some variation was observed in the specific capacity, the potential profiles of CuFeHCF varied little with composition. On the other hand, NiFeHCF showed a dramatic increase in its reaction potential as Fe was added. In addition, NiFeHCF suffered from increased voltage hysteresis with increasing Fe content, suggesting that the kinetics of electrochemical cycling became slower as more Fe was incorporated into the lattice. The low specific capacities observed at some intermediate compositions of CuFeHCF and NiFeHCF cannot be explained at this time. Specific capacity values were not found to follow any trend with composition.

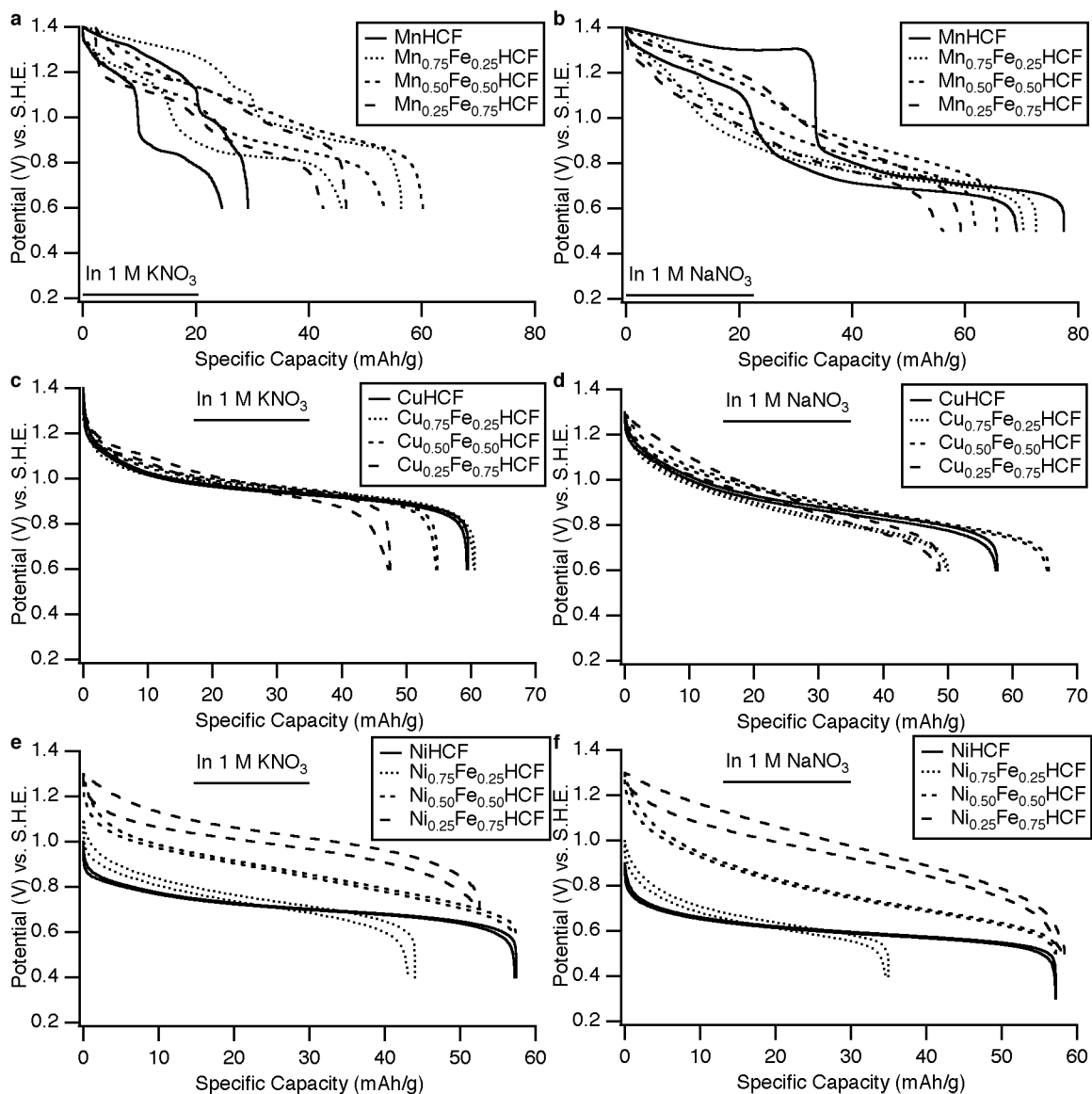


Figure 37: (a-f) The potential profiles of MnFeHCF, CuFeHCF, and NiFeHCF, during their reactions with K⁺ and Na⁺, respectively.

The reaction potentials of CuFeHCF with both K⁺ and Na⁺ increased slightly with increasing Fe content (Fig. 38). This is consistent with the behavior of the CuNiHCF system, as the known reaction potential for the oxidation of Prussian Blue to Berlin Green in 1 M K⁺ is about 1.17 V vs. S.H.E., significantly higher than the 0.95 V reaction potential of pure CuHCF. The increase in the reaction potentials of NiFeHCF is much more dramatic. In this case, the reaction potential of pure NiHCF is much lower than that of Berlin Green, so the addition of Fe to the structure increases the reaction potential substantially.

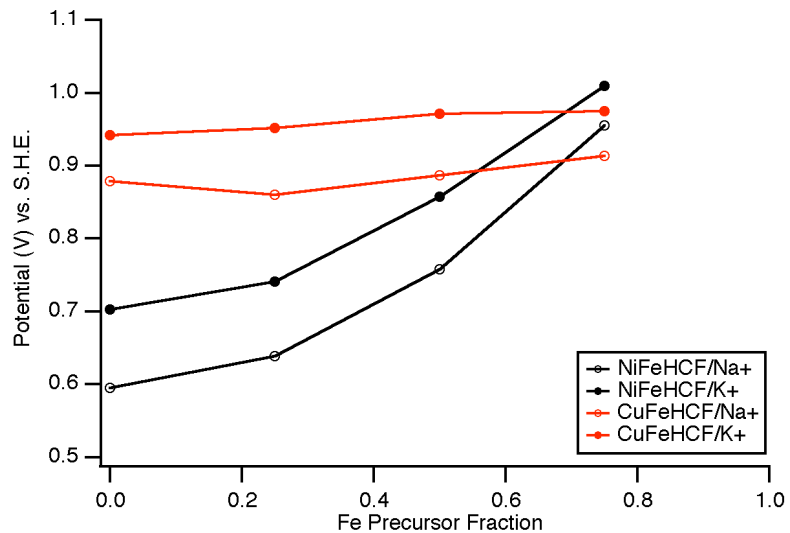


Figure 38: The reaction potentials of CuFeHCF with K^+ and Na^+ increase only slightly as the Fe content of the material increases. In contrast, the reaction potentials of NiFeHCF with K^+ and Na^+ rise dramatically as Fe added to the structure.

Chapter 13: Prussian Blue Analogue Anodes for Aqueous Batteries

13.1 The Need for a Prussian Blue Analogue Anode

CuHCF, NiHCF, and the other materials discussed thus far all rely on the electrochemical activity of the hexacyanoferrate group. They all react with K^+ above 0.7 V vs. S.H.E., making them useful as cathodes in aqueous batteries. However, real devices require both a cathode and an anode. No known anode material for any kind of aqueous battery has cycle life, power, or efficiency that compares to the Prussian Blue analogue cathodes, so using any known anode material would severely limit the performance of any cell containing a Prussian Blue analogue cathode. For this reason, considerable effort was made to identify Prussian Blue analogues with low reaction potentials with the goal of eventually producing a cell that pairs this anode with a CuHCF or NiHCF cathode.

Of the hexacyanoferrate-based Prussian Blue analogues, only a few are known to have low reaction potentials. This is because the hexacyanoferrate group itself reacts at high potential, so any low potential electrochemical activity must come from the P site cation. The P site Fe^{3+} in Prussian Blue may be reduced to Fe^{2+} , but the reaction potential for this process is 0.45 V vs. S.H.E., far too high for a practical anode.³⁵ Though some studies have used Prussian Blue as an anode, this resulted in batteries with discharge voltages of only 0.5-0.7 V, too low to be practical.³⁸⁻⁴⁶

13.2 Synthesis and Characterization of Titanium Hexacyanoferrate

Another hexacyanoferrate material with P site electrochemical activity is titanium hexacyanoferrate (TiHCF), in which P site oxytitanium ($Ti^{IV}O)^{2+}$ is reduced to Ti^{3+} at 0.2 V vs. S.H.E.^{157, 179, 194} Pairing TiHCF with a CuHCF cathode, for example, would result in a cell with an average discharge voltage of 0.75 V, which may be enough for its practical use. TiHCF is an atypical Prussian Blue analogue because of the complex nature of aqueous titanium chemistry. It was found to have a sharp reaction during proton insertion, while most of the hexacyanoferrate materials do not. Also, the oxidation of P site Ti^{3+} results in the formation of an $(Ti^{IV}O)^{2+}$ cation, not just Ti^{4+} . The latter species is unstable in water and acid, and forms strong bonds to oxygen (typically resulting in TiO_2). Thus, zeolitic water and any defects in the framework that allow water to coordinate to the P sites results in the formation of $(Ti^{IV}O)^{2+}$. Indeed, the synthesis of electrochemically active TiHCF was found to require a $(Ti^{IV}O)^{2+}$ precursor, as will be shown below.

The use of titanium led to considerable complications to the synthesis of TiHCF. The co-precipitation syntheses discussed in Chapter 8 were performed in neutral water. However, no titanium species are stable in neutral water, as they rapidly hydrolyze to form TiO_2 . Synthesis of TiHCF must therefore be done in strong acid. Furthermore, the Ti^{3+} and $(Ti^{IV}O)^{2+}$ complexes that are acid-stable can still react with dissolved O_2 , so TiHCF must be synthesized in an inert atmosphere. Previous work on TiHCF studied only

electrodeposited thin films that are not useful for batteries. Three methods were developed to produce bulk quantities of TiHCF, only one of which yielded an electrochemically active material.

The first synthesis method for TiHCF used a $(\text{Ti}^{\text{IV}}\text{O})^{2+}$ precursor. To make it, concentrated, de-aerated H_2SO_4 was added to TiCl_4 under inert atmosphere under constant stirring. This results in both the immediate formation of bright yellow TiOSO_4 , but also the rapid evolution of large quantities of HCl vapor. Therefore, proper containment of the reaction and extreme caution on the part of the researcher must be exercised. Upon successful production of the TiOSO_4 precursor, water was slowly added to dilute the H_2SO_4 to a 5:1 volume ratio. This resulted in a solution of about 100 mM TiOSO_4 and 3 M H_2SO_4 . The $(\text{Ti}^{\text{IV}}\text{O})^{2+}$ present in this solution was extremely sensitive to oxygen, so the standard co-precipitation method could not be used to synthesize the final TiHCF product. Rather, a de-aerated solution of 50 mM $\text{K}_4\text{Fe}(\text{CN})_6$ was added directly to the TiOSO_4 solution. A vermilion powder promptly precipitated. This product was filtered, washed with water, and dried in a N_2 glove bag.

The safety concerns related to the formation of $(\text{Ti}^{\text{IV}}\text{O})^{2+}$ from TiCl_4 resulted in the development of a second synthesis method for TiHCF. Some Ti^{3+} salts are stable in acidic conditions, even though they rapidly hydrolyze to TiO_2 in neutral water. Using the co-precipitation method, 20 mM $\text{Ti}_2(\text{SO}_4)_3$ in dilute H_2SO_4 was reacted with a second solution containing 10 mM $\text{K}_3\text{Fe}(\text{CN})_6$ by simultaneous, dropwise addition into dilute acid under constant stirring in an inert atmosphere. As the oxidation potential of Ti^{3+} to $(\text{Ti}^{\text{IV}}\text{O})^{2+}$ is about 0.2 V vs. S.H.E., lower than the reduction potential of $\text{Fe}(\text{CN})_6^{3-}$ to $\text{Fe}(\text{CN})_6^{4-}$ (0.355 V), addition of the two precursors resulted in the oxidation of Ti^{3+} and the reduction of $\text{Fe}(\text{CN})_6^{3-}$. This reaction resulted in the precipitation of a red product, which was filtered, washed with water, and dried in N_2 . The color of this product was the same as that of the powder synthesized from a TiOSO_4 precursor, suggesting that they both contain $(\text{Ti}^{\text{IV}}\text{O})^{2+}$, rather than any Ti^{3+} .

Finally, TiHCF containing Ti^{3+} was also synthesized. The same co-precipitation procedure as before was used, except in this case, a $\text{K}_4\text{Fe}(\text{CN})_6$ precursor containing reduced hexacyanoferrate was chosen. As both the titanium and hexacyanoferrate were in their reduced states, no oxidation of either species occurred. A dingy yellow powder rapidly precipitated when the two precursors were combined. This product, presumably of the composition $\text{K}_x\text{Ti}_y\text{Fe}(\text{CN})_6$, was filtered, washed, and dried in an inert atmosphere.

The preparation and electrochemical characterization of electrodes containing these materials was performed in N_2 , but all other methods were the same as those described in Chapter 8-10. X-ray diffraction was performed on the TiHCF powders. Regardless of the oxidation state of titanium in the materials, they were found to have the FCC structure observed for other hexacyanoferrate-based Prussian Blue analogues (Fig. 39a).

Electrochemical characterization of TiHCF was performed using cyclic voltammetry. Only the material synthesized by the co-precipitation method that used $\text{Fe}(\text{CN})_6^{3-}$ to oxidize Ti^{3+} to $(\text{Ti}^{\text{IV}}\text{O})^{2+}$ showed any electrochemical activity. Its reaction potential at 0.3 V vs. S.H.E. is higher than the previously reported value for thin films of this material by about 0.1 V (Fig. 39b). The cyclic voltammetry scan shown here was performed in electrolyte containing both 1 M K^+ and 1 M H^+ . The undesirable fading in the current

response of the material was found to be even faster in less acidic electrolytes. This result showed that though TiHCF could in principle be used as an anode in an aqueous battery, its chemical instability and rather high reaction potential make it an impractical anode. It is possible that the failure to measure electrochemical activity for TiHCF synthesized by the other two methods was due to its decomposition to TiO_2 in the presence of air.

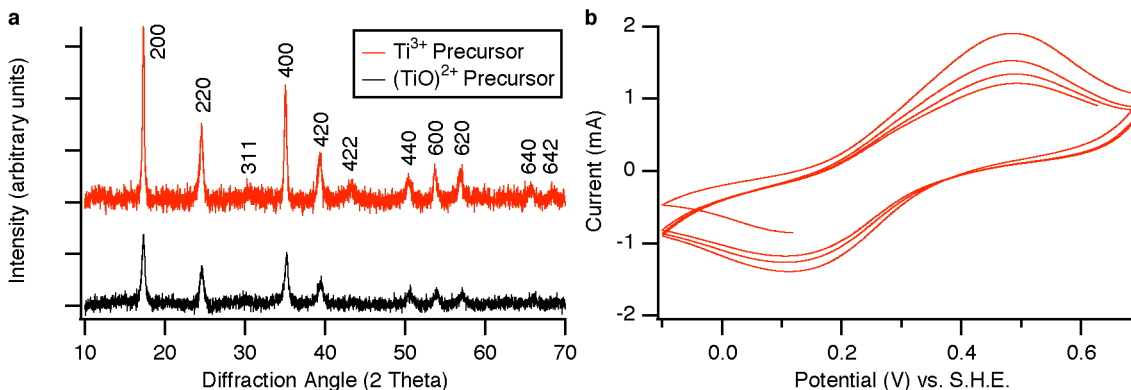


Figure 39: (a) XRD of TiHCF found that regardless of the titanium precursor used during synthesis, the product had the correct crystal structure. (b) Cyclic voltammetry of TiHCF synthesized from Ti^{3+} and $\text{Fe}(\text{CN})_6^{3-}$. The scan was performed in 1 M KNO_3 /1 M HNO_3 at 1 mV/s. Rapid capacity fading was observed, showing that the material was chemically unstable.

13.3 Other Hexacyanometalates

Only a few of the hexacyanoferrate-based Prussian Blue analogues have low reaction potentials, so they generally cannot be used as anodes. Many other Prussian Blue analogues that do not contain hexacyanoferrate also exist, and some of these do have reaction potentials that make them suitable for use as anodes. These materials contain other hexacyanometalates, such as $\text{Ti}(\text{CN})_6$, $\text{V}(\text{CN})_6$, $\text{Mn}(\text{CN})_6$, $\text{Cr}(\text{CN})_6$, $\text{Co}(\text{CN})_6$, $\text{Ni}(\text{CN})_6$, $\text{Ir}(\text{CN})_6$, $\text{Ru}(\text{CN})_6$, or $\text{Pt}(\text{CN})_6$.^{100, 120-122, 126-127, 156, 159, 182-185} Those containing Ti, V, and Mn, among others, have received particular attention from physicists due to their magnetic ordering temperatures of 300 K or more.¹⁸²⁻¹⁸⁶ Hexacyanometalates of Ir, Ru, and Pt are extraordinarily expensive, and though Prussian Blue analogues containing these received some study for their electrochromic properties, their high cost prohibits their use in battery electrodes.^{40, 138} The $\text{Co}(\text{CN})_6^{3-}$ anion is extremely stable, but its electrochemical activity has never been conclusively documented, and is believed to be too low to be observed in aqueous solutions without rapid hydrogen evolution. $\text{V}(\text{CN})_6$, $\text{Ti}(\text{CN})_6$, and $\text{Ni}(\text{CN})_6$ are unstable in water (the last two to such an extent that their existence remains somewhat apocryphal).¹⁹⁶⁻²⁰⁰ However, some Prussian Blue analogues that contain either $\text{Mn}(\text{CN})_6$ or $\text{Cr}(\text{CN})_6$ have reaction potentials that make them attractive for use as anodes. In his first study of a battery containing Prussian Blue, Neff also noted that a “manganese blue” of the formula $\text{KFeMn}(\text{CN})_6$ had a reaction potential near 0 V vs. S.H.E., and was therefore a promising anode.³⁸ Much later, limited study of the electrochemical properties of Prussian Blue analogues containing $\text{Cr}(\text{CN})_6$ and $\text{Mn}(\text{CN})_6$ was conducted

by Sholz and Dostal, starting in 1995.^{159, 178, 201} More recently, other researchers have studied various Prussian Blue analogues containing $\text{Cr}(\text{CN})_6$.²⁰²⁻²⁰³

13.4 Synthesis and Characterization of Iron Hexacyanomanganate

Iron hexacyanomanganate (FeHCMn) appears to be a particularly desirable anode material. Its low reaction potential of about 0.05 V vs. S.H.E. is ideal for an anode that operates in acidic electrolytes, and pairing CuHCF with FeHCMn would result in a battery with an average voltage of 0.9 V. In addition, the Fe and Mn precursors are abundant, inexpensive, and commercially available in large quantities. For these reasons, FeHCMn was studied as a possible anode for aqueous batteries. It was synthesized using the coprecipitation method from de-aerated precursor solutions that contained $\text{K}_3\text{Mn}(\text{CN})_6$ or FeSO_4 . A bright blue precipitate formed. This precipitate was filtered, washed with water, and dried in N_2 . The same electrode preparation steps were used as previously described.

Cyclic voltammetry of FeHCMn electrodes was performed in 1 M KNO_3 at neutral pH (Fig 40). The open circuit potential was found to be over 0.6 V (Fig. 40a). A reversible reaction was observed at 0 V vs. S.H.E., in agreement with previously published data. The capacity faded rapidly when FeHCMn was cycled between -0.3 V and 0.2 V. Cycling over a more narrow potential range between -0.1 V and 0.1 V slowed the capacity fading somewhat (Fig. 40b). No electrochemical testing was performed in acidic solutions because the cyanide ligand is much more labile in $\text{Mn}(\text{CN})_6$ than in $\text{Fe}(\text{CN})_6$, so FeHCMn would likely have decomposed in acid, releasing HCN.

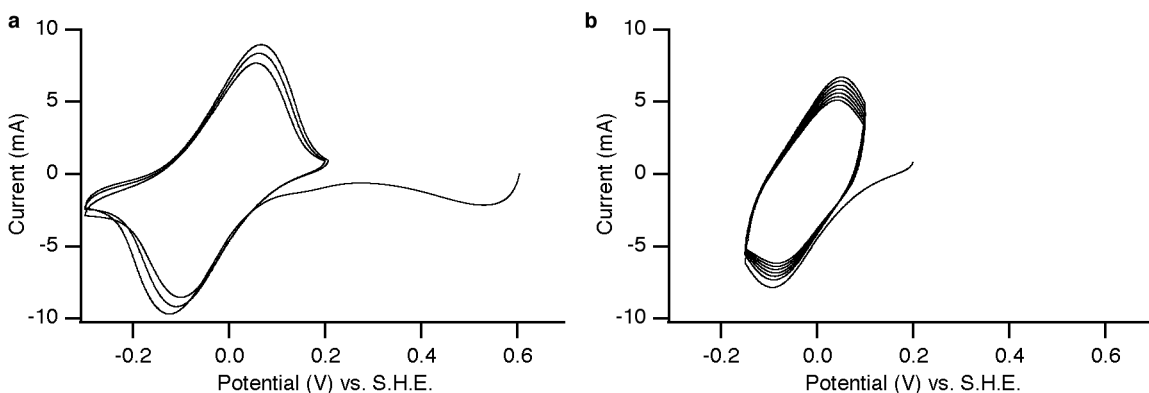


Figure 40: (a) The initial cyclic voltammetry of a FeHCMn electrode in neutral 1 M KNO_3 . The electrode has a high open circuit potential of 0.6 V vs. S.H.E., a sharp reaction potential at 0 V, and its capacity fades quickly. (b) Immediately subsequent to the scan in (a), the potential limits were narrowed to -0.1 V and 0.1 V. The rate of capacity fading decreases marginally.

The high open circuit potential, rapid capacity loss, and blue color of FeHCMn can all be attributed to the chemical instability of the hexacyanomanganate complex. Exposure of $\text{Mn}^{\text{III}}(\text{CN})_6^{3-}$ to water results in disproportionation to Mn^{2+} and $\text{Mn}^{\text{IV}}(\text{CN})_6^{2-}$.²⁰⁴⁻²⁰⁵ These two ions may slowly react in solution, producing the Prussian Blue analogue manganese hexacyanomanganate (MnHCMn). Unfortunately, the stability of

the hexacyanomanganate complex does not improve upon its successful incorporation into the FeHCMn structure. Using Moss Bauer spectroscopy, Reguera, et al conclusively showed that some of the cyanide ligands in the FeHCMn framework will spontaneously isomerizes.²⁰⁶ FeHCMn converts first to an intermediate compound in which some of the cyanide linkers are oriented such that Fe, rather than Mn, is carbon-coordinated. But, given sufficient time, the cyanide ligands will fully isomerizes, and the material becomes MnHCF.²⁰⁶ This process occurs spontaneously at room temperature.

This cyanide isomerization explains the high open circuit potential of the FeHCMn synthesized during this work: along with $\text{Mn}(\text{CN})_6$, it also contained some carbon-coordinated Fe^{3+} that had a reaction potential near those of the hexacyanoferrate Prussian Blue analogues. The capacity loss of FeHCMn occurred because this isomerization process continued, and nitrogen-coordinated Mn^{2+} is not electrochemically active in the framework of MnHCF. Finally, pure, anhydrous FeHCMn can be synthesized with minimal isomerization in organic solvents, but its dark green color turns to blue when it is exposed to water and partially hydrolyzed.¹⁸⁴ Though FeHCMn has a reaction potential that makes it an excellent anode for aqueous batteries, its chemical instability prevents its practical use.

Other hexacyanomanganate Prussian Blue analogues including MnHCMn and chromium hexacyanomanganate have also been studied for their electrochemical and magnetic properties. During this thesis, some preliminary electrochemical measurements were performed on chromium hexacyanomanganate and manganese hexacyanomanganate. Unfortunately, they also suffer from poor chemical stability. The extreme lability of CN in the hexacyanomanganate complex makes it unlikely that any of them will be stable enough to last thousands of charge/discharge cycles if used as battery electrodes.

13.5 Synthesis and Characterization of Chromium Hexacyanochromate

The hexacyanochromate complex also has a low reaction potential, and it is known to be more stable than hexacyanomanganate. A few studies have found that hexacyanochromate-based Prussian Blue analogues are electrochemically active between -1.1 V and -0.5 V vs. S.H.E.^{159, 178, 201-203, 207} Though these reaction potentials are too low for use in acidic electrolytes, they are suitable for neutral ones. Chromium hexacyanochromate (CrHCCr) was previously found to have a reaction potential of -0.56 V vs. S.H.E., the highest of any member of this family.¹⁵⁹ A bulk synthesis method was developed to produce CrHCCr for use in battery electrodes.

Large quantities of the hexacyanochromate precursor needed to produce CrHCCr were not readily available at a reasonable cost, so it was synthesized in collaboration with Christina Li. An aqueous solution of 17 mL of 0.5 M chromium acetate basic and 1 M acetic acid was added to 55 mL of 3 M KCN at 90° C and stirred for two hours. This formed a dark orange solution. Filtration of this solution resulted in a dark green precipitate and a bright yellow filtrate. About 50 mL of methanol was added to the filtrate (to favor precipitation of $\text{K}_3\text{Cr}(\text{CN})_6$, and it was refrigerated overnight. Repeated rotary evaporation of the solvent and addition of pure methanol caused a yellow solid to precipitate. This material was filtered and dried in vacuum. Chemical analysis of this product was not performed, but it was presumed to be $\text{K}_3\text{Cr}(\text{CN})_6$.

Using the freshly synthesized $\text{K}_3\text{Cr}(\text{CN})_6$ precursor, CrHCCr was then synthesized. A de-aerated aqueous solution containing 0.9 mmol of $\text{K}_3\text{Cr}(\text{CN})_6$ was injected into a flask that contained CrCl_2 in an argon atmosphere. The solution immediately turned dark green. It was stirred for one hour at room temperature, and then filtered in air. A dark gray precipitate was obtained, while the filtrate was colorless. This material was dried overnight in vacuum, resulting in a gray powder. The color of this material matched the previously reported gray color of CrHCCr. Electrodes containing CrHCCr were prepared using the techniques previously described.

Physical and electrochemical characterization of CrHCCr was performed using XRD and cyclic voltammetry, respectively (Fig. 41). The material was found to be phase pure, with a lattice parameter of 10.42 Å, in agreement with a previously reported value.¹²¹ Cyclic voltammetry of CrHCCr in neutral M KCl found that it has a reaction potential of -0.55 V vs. S.H.E., close to the previously reported potential.¹⁵⁹ Rapid capacity fading (not shown in Fig. 41b) during cycling was observed. In addition, the low reaction potential of CrHCCr is beyond the useful stability range of the electrolyte. This is apparent in Fig. 41b, in which a large, irreversible background current is present at low potentials along with the reversible reaction of CrHCCr. Though the reaction potential of CrHCCr is too low for its practical use as an anode in neutral or acidic aqueous solutions, it is possible that other hexacyanochromate-based Prussian Blue analogues have higher reaction potentials. That said, the relatively high cost of chromium makes them less attractive for large-scale energy storage than the hexacyanoferrate-based materials.

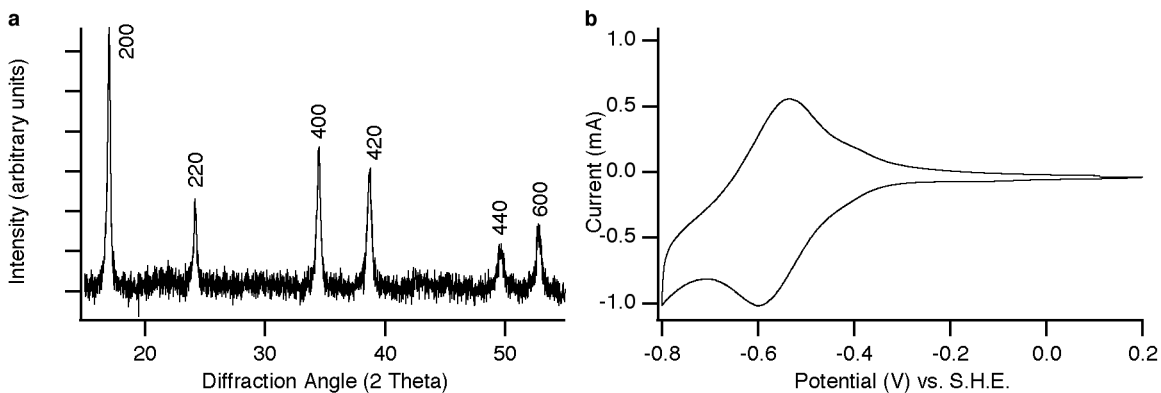


Figure 41: (a) XRD of CrHCCr found that the material had the Prussian Blue crystal structure with a lattice parameter of 10.42 Å. (b) Cyclic voltammetry of CrHCCr at 1 mV/s in 1 M KCl found that it has a reaction potential of -0.55 V vs. S.H.E..

Conclusions About Prussian Blue Analogue Anodes

In summary, several Prussian Blue analogues with low reaction potentials were synthesized and their electrochemical behavior was studied in aqueous electrolytes. TiHCF is one of only a few hexacyanoferrate-based Prussian Blue analogues in which the P site cation is electrochemically active at low potentials. FeHCMn was found to have a reaction potential near S.H.E., ideal for an anode in acidic electrolytes. CrHCCr was successfully synthesized from in-house $K_3Cr(CN)_6$, but its reaction potential is too low to be used in aqueous devices of mildly acidic or even neutral pH. Unfortunately, all three of these materials also proved to be chemically unstable. Any anode paired with the CuHCF or NiHCF cathodes must be extremely stable, and capable of thousands of deep-discharge cycles.

The modest performance of Prussian Blue analogue anodes resulted in the exploration of other families of materials. The possibility that a stable Prussian Blue analogue with a reaction potential near or below S.H.E. exists will remain an open question.

Chapter 14: Full Cell Devices Using Prussian Blue Analogues

14.1 Introduction to the Activated Carbon/Conducting Polymer Hybrid Anode

The failure to develop a viable Prussian Blue analogue anode material led to a broadened evaluation of possible materials for use as anodes in devices with CuHCF or NiHCF cathodes. The use of those cathodes places stringent conditions on any anode: it must be chemically stable in mildly acidic electrolytes, must have a reaction potential near or just below SHE, and preferably react with either K^+ or Na^+ , as the Prussian Blue analogues are sensitive to the presence of other ions such as Li^+ . Furthermore, an interesting anode paired with CuHCF or NiHCF must have extremely long cycle life, and be capable of high efficiency cycling at high current densities. No well-developed battery materials meet all of these criteria. However, activated carbon (AC), which is commonly used in electrical double layer capacitors (EDLC), does have all of these properties under certain circumstances.

Like other EDLC electrodes, AC stores charge on its surface.¹⁸ Application of a potential results in the formation of a double layer of charge at the interface between the electrode and the electrolyte. The amount of charge stored on the electrode depends on its surface area and it varies linearly with the applied potential. Because only the surface of EDLC electrodes participates in charging, these electrodes typically have specific capacities that are much lower than those of batteries. For example, commercially available AC has a reversible specific capacity of less than 10 mAh/g unless it is charged to very high potentials. To achieve appreciable capacity in narrow potential ranges, a much larger surface area, and therefore, electrode mass, is necessary. As the power of a battery scales with the square of its voltage, large decreases in voltage during discharge are unfavorable. Thus, when using an EDLC electrode in a battery, it must be very large so that enough discharge capacity is available with only a small change in the potential.

The high open circuit potential of AC further complicates its use as an anode in aqueous batteries. Electronegative, oxygenated groups on the surface of AC result in open circuit potentials of about 0.4 V vs. S.H.E.¹⁵⁴ If a small EDLC anode mass is used, it can be charged to very low potentials, resulting in a high full cell voltage. But, only a small fraction of the total charge of the device will be available at useful voltages. If a large mass of AC is used, then its potential will vary less, but the high open circuit potential will result in a battery that has a low full cell voltage at all times. For this reason, the high open circuit potential prevents most AC from being used as a battery anode in aqueous electrolytes.

In 2011, Dr. Mauro Pasta developed a new type of anode that combines AC with other materials in an attempt to produce an anode suitable for combination with the CuHCF cathode.¹⁵⁴ Like other EDLC electrodes, AC is not electrochemically active, and it stores charge only on its surface. As it is extremely conductive, its potential will equilibrate with all other materials with which it is in contact. Therefore, the addition of an electrochemically active species with a well-defined electrochemical potential to an electrode containing AC will fix the potential of that entire electrode, including the AC, at that of the active additive.

The example first demonstrated by Dr. Pasta was the addition of polypyrrole (PPy) to an AC electrode. The reaction potential of PPy in aqueous solutions is about -0.1 V vs. SHE. The addition of PPy in its reduced state to a AC electrode resulted in an open circuit potential that was equal to the reaction potential of PPy. These AC/PPy electrodes contained AC, PPy, and PVDF binder in a 80:10:10 mass ratio.

If cycled between high and low potentials through the reaction potential of pure PPy, these AC/PPy have some faradaic capacity due to the oxidation and reduction of the PPy. However, they are typically charged to even lower potentials relative to the open circuit condition, so only AC contributes to their capacity. These AC/PPy electrodes therefore have the long cycle life, high power, and high energy efficiency of the pure AC electrodes used in EDLCs. Further details of the AC/PPy electrode and the general concept of using an electrochemically active additive to control the potential of a capacitive electrode will be discussed in a future publication.

14.2 Controlling the Initial Charge State of Copper Hexacyanoferrate

Some of the development needed to adapt the CuHCF cathode for use in real batteries was completed during the development of the CuHCF vs. AC/PPy cell. For instance, freshly synthesized CuHCF has an intermediate charge state (typically 50-80% charged) when produced by the co-precipitation method. This is because the first-formed solid contains fully oxidized $\text{Fe}^{\text{III}}(\text{CN})_6^{3-}$. As shown in Fig. 22a, the equilibrium potential of fully oxidized CuHCF is over 1.2 V vs. SHE. This potential is much greater than the potential for hydrolysis of water to oxygen at neutral pH. As a result, CuHCF is partially reduced and water is oxidized to oxygen. This process proceeds until the potential of the CuHCF is low enough that water is not spontaneously hydrolyzed at the surface of a CuHCF particle. If CuHCF is removed from solution immediately following its precipitation, it will have a charge state of nearly 80%, but if it is processed several hours later, its initial state may be as low as 50% charged as its reduction by water continues.

For the half-cell measurements performed during the characterization of CuHCF alone, its initial charge state was not of interest. However, in real batteries, the initial charge states of the two electrodes must be matched to avoid squandering a portion of the capacity of one of the electrodes. The AC/PPy anode developed by Dr. Pasta, as well as many others, have initial states of full discharge. A chemical reduction method compatible with the co-precipitation synthesis procedure was developed for Prussian Blue analogues so that electrodes containing them would have a fully discharged initial state.

Immediately after the complete addition of the two precursor solutions during the co-precipitation synthesis of CuHCF, an aqueous solution of sodium thiosulfate ($\text{Na}_2\text{S}_2\text{O}_3$) was added. As more $\text{Na}_2\text{S}_2\text{O}_3$ was added, the color of the CuHCF colloid changed from goldenrod to a dark burgundy, the same color known for CuHCF synthesized from $\text{Fe}^{\text{II}}(\text{CN})_6^{4-}$. Though the latter precursor would yield fully reduced CuHCF in a fully reduced state, its use was found to result in extremely rapid precipitation, poor crystallinity, and inferior electrochemical performance. In contrast, CuHCF reduced by $\text{Na}_2\text{S}_2\text{O}_3$ was found to have the same electrochemical properties as CuHCF never exposed to a reducing agent.

The fractional initial charge state of CuHCF may be controlled by the amount of $\text{Na}_2\text{S}_2\text{O}_3$ added during

synthesis (Fig. 42a). Fractional initial charge state is defined as the capacity of the first charge, divided by the capacity of the second charge from a fully discharged state. As freshly precipitated CuHCF is about 80% charged, the addition of $\text{Na}_2\text{S}_2\text{O}_3$ in a 0.8:1 ratio results in the full reduction of CuHCF. Addition of less $\text{Na}_2\text{S}_2\text{O}_3$ results in a fractional charge state. Thus, the initial charge state of CuHCF may be selected as necessary to match the charge state of an anode. In addition, it is not necessary to perform chemical reduction on raw CuHCF powder, and it can instead be performed on fully prepared electrodes.

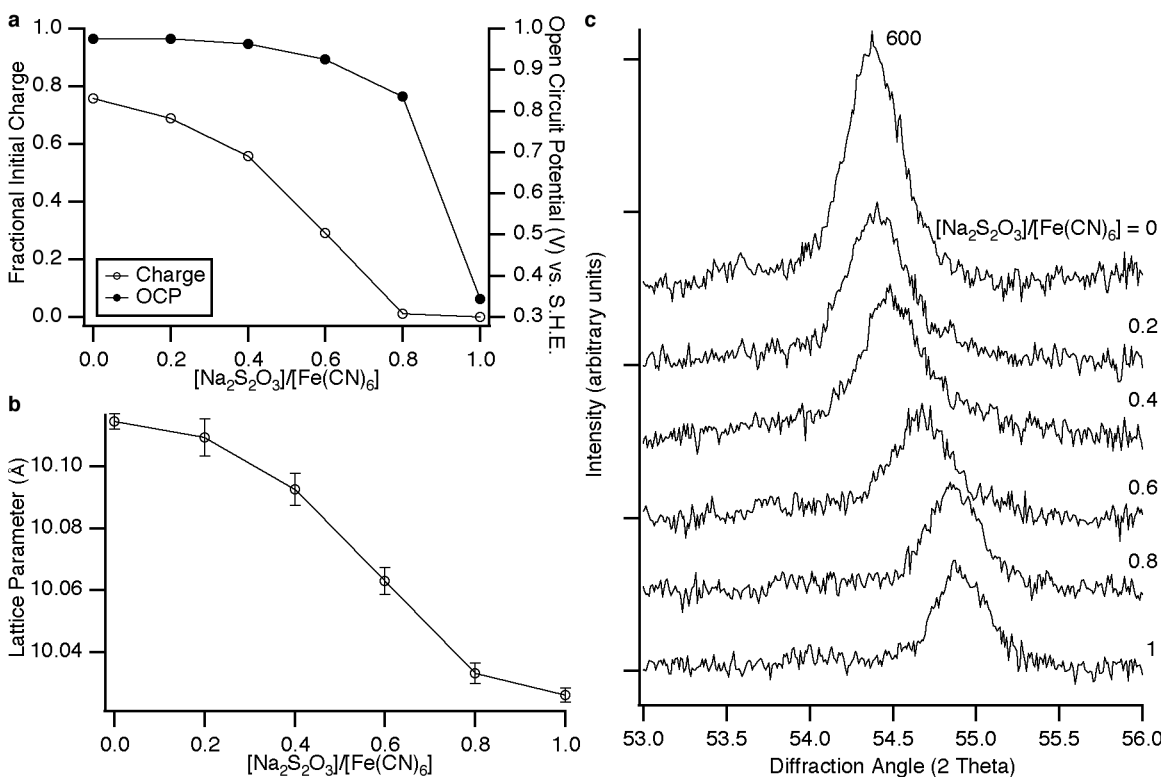


Figure 42: (a) The fractional initial charge of CuHCF electrodes decreased if more $\text{Na}_2\text{S}_2\text{O}_3$ was added after precipitation. The open circuit potential decreased slowly as $\text{Na}_2\text{S}_2\text{O}_3$ was added until CuHCF was fully reduced, after which it dropped by over 0.5 V to 0.34 V, the reduction potential of metallic copper. This suggests that excess $\text{Na}_2\text{S}_2\text{O}_3$ reduces the excess Cu^{2+} present during the synthesis. (b) The lattice parameter of CuHCF decreased about 1% upon chemical reduction. The error bars are one standard deviation about the average lattice parameter calculated from 10 peaks for each sample. (c) The shift in the 600 peak to higher diffraction angles as $\text{Na}_2\text{S}_2\text{O}_3$ shows the effects of the decrease in lattice parameter.

During the reduction of CuHCF by $\text{Na}_2\text{S}_2\text{O}_3$, both K^+ and Na^+ are present in solution. The dominant intercalant during chemical reduction is K^+ , and not Na^+ . Upon the complete addition of the $\text{K}_3\text{Fe}(\text{CN})_6$ precursor to the reaction flask, K^+ is present in a 3:1 molar ratio to CuHCF. In contrast, the concentration of Na^+ is much lower during the initial addition of $\text{Na}_2\text{S}_2\text{O}_3$, and even upon full reduction of CuHCF, it is

present in only a 1.6:1 molar ratio. Furthermore, CuHCF reacts with K^+ at a much higher potential than with Na^+ . When it is reduced from an even higher potential, a driving force for K^+ insertion will exist before one for the insertion of Na^+ develops. Finally, the lattice parameter of CuHCF was found to decrease by 0.9% during chemical discharge (Fig. 42b-c), a result comparable to the strain observed during electrochemical cycling (Fig. 23).

Regardless of the anode with which CuHCF and other Prussian Blue cathodes are paired, the initial charge states of both electrodes must be matched. Chemical reduction using $Na_2S_2O_3$ during synthesis provides a fast, scalable method to set the charge state of CuHCF to a desired value.

14.3 Electrochemical Performance of Full Cells

Figure 43 summarizes the performance of a full cell containing a CuHCF cathode, a AC/PPy anode, and an acidic 1 M KH_2PO_4 buffer solution. The data presented here were collected for cycling at a 10C rate (500 mA/g CuHCF). So that the entire capacity of each charge/discharge cycle was available at a steady, high voltage, the cell was cycled over the middle 80% of the capacity of the CuHCF cathode. This results in a cell with a specific capacity of 45 mAh/g CuHCF available between 1.4 and 0.9 V, with an average discharge voltage of about 1.1 V. This resulted in a specific energy for the full cell of just over 5 Wh/kg. In comparison, deep discharge of a commercial lead acid cell results in a specific energy of about 22 Wh/kg, but during the shallow depth of discharge needed for long cycle life, only 10-15 Wh/kg is achieved. Because of the high cycling rate, the CuHCF vs. AC/PPy cell was capable of over 50 W/kg, twice the specific power of a lead acid cell.

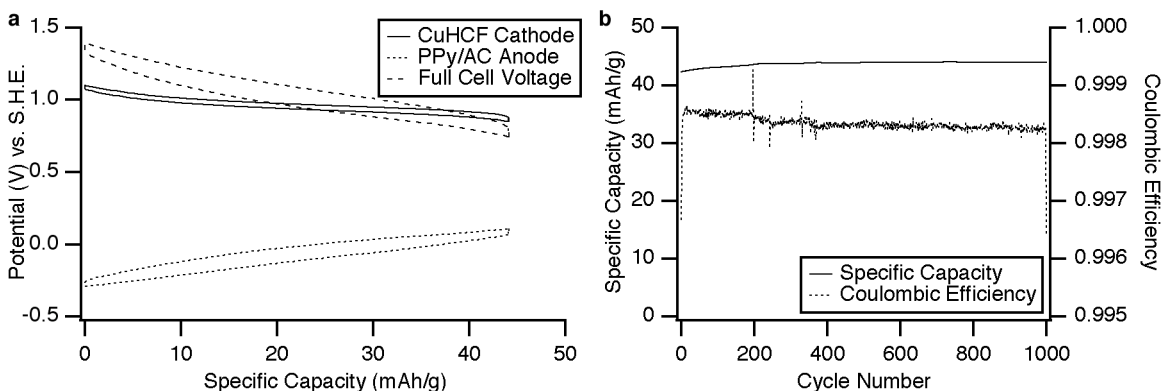


Figure 43: (a) The potential profiles of CuHCF and AC/PPy, and the full cell voltage during 10C cycling in acidic 1 M KH_2PO_4 . (b) Zero capacity loss is observed after 1,000 cycles, and the coulombic efficiency is over 99.8%.

The CuHCF vs. AC/PPy full cell shows remarkable stability during extended cycling. Zero capacity loss is observed for 1,000 deep discharge cycles at a 10C rate, and the coulombic efficiency is over 99.8% for the duration of cycling. At this cycling rate, the energy efficiency was 92%. This high rate energy efficiency is greater than that of any current commercial battery technology. It is expected that continued

development will result in even longer cycle lives, making the CuHCF vs. AC/PPy a viable choice for stationary storage applications. In particular, its long cycle life, high power, and high energy efficiency make it useful for the short-term, transient applications discussed in Chapter 1.

Chapter 15: High Voltage Cells Using Prussian Blue Analogues

15.1 Introduction and History

The work on Prussian Blue analogues focused on their behavior as electrodes in aqueous batteries because of the cost and safety advantages of such cells. However, the behavior of Prussian Blue analogues in organic electrolytes is somewhat of a curiosity. Though Vernon Neff is generally credited with the first demonstration of a Prussian Blue battery in 1985, in fact, study of Prussian Blue electrodes began much earlier. In 1979, Messina and Perichon studied the behavior of silver hexacyanoferrate as a lithium-ion insertion cathode, and the following year, they demonstrated that Prussian Blue could be used as a lithium ion cathode with long cycle life in organic cells.³⁶⁻³⁷ In the latter study, they showed that Prussian Blue retained 53% of its initial discharge capacity after 250 deep discharge cycles, making it the longest-lived high voltage lithium ion cathode known at that time. In more recent years, other Prussian Blue analogues including MnHCF have received study as positive electrodes in organic electrolyte lithium-ion cells.⁴⁶ Excellent cycle life was observed, but the relatively low specific capacity of Prussian Blue analogues in comparison to LiCoO_2 , LiMn_2O_4 , and LiFePO_4 makes them rather impractical for devices that require high specific energy.

Also remarkable was the demonstration of the only organic electrolyte potassium ion batteries. Eftekhari first demonstrated that Prussian Blue could be cycled against metallic potassium in an organic electrolyte for over 500 deep discharge cycles with little capacity loss.²⁰²⁻²⁰³ Unfortunately, these cells relied on thin film electrodes containing only a few μg of Prussian Blue, and the combination of a flammable organic electrolyte and metallic potassium anode make a breathtakingly dangerous device.

15.2 Electrochemical Performance of Copper Hexacyanoferrate in Organic Electrolytes

The behavior of Prussian Blue analogues in organic cells was studied in collaboration with Sandeep Peddada. Working electrodes containing CuHCF were prepared by the standard method, except that stainless steel current collectors were used. Sealed pouch cells containing one of these working electrodes, an alkali metal anode, an organic electrolyte, and a plastic separator were assembled. In the case of the organic lithium-ion cell, commercially available electrolyte containing a 1:1 mixture of ethylene carbonate and diethyl carbonate, and 1 M LiPF_6 was used. Organic Na^+ and K^+ electrolytes were prepared in-house by adding anhydrous, ultra high purity NaClO_4 or KClO_4 to pure ethylene carbonate. In the former case, 1 M NaClO_4 was dissolved, but in the latter, the solubility limit of KClO_4 was found to be about 0.1-0.2 M. Finally, potassium is much softer than lithium or sodium, is not commercially available as a foil, and sticks to many metal surfaces. Potassium electrodes must therefore be prepared with caution.

Cyclic voltammetry of CuHCF was performed in organic Li^+ , Na^+ , and K^+ cells (Fig. 44a). CuHCF was found to have no electrochemical activity in an organic K^+ electrolyte. However, it was found to have

reversible electrochemical reactions with Li^+ and Na^+ . Its reaction with Li^+ occurred at 3.3 V vs. Li^+/Li , while its reaction with Na^+ occurred at 2.9 V vs. Na^+/Na , or equivalently, 3.2 V vs. Li^+/Li . The reaction of CuHCF with Na^+ was much sharper than its reaction with Li^+ . Irreversible capacity during sweeps to lower potentials was observed below 2.5 V in the Na^+ cell. This was likely a byproduct of contamination of the sodium anode or the electrolyte.

Galvanostatic cycling of CuHCF was performed at a C/6 rate (10 mA/g) in organic Li^+ and Na^+ cells. The material was found to have a specific capacity of about 65 mAh/g during Na^+ cycling, but only about 45 mAh/g during Li^+ cycling. The reason for this large discrepancy between the observed specific capacities is unknown. As in the case of cyclic voltammetry measurements, the reaction potentials with Li^+ and Na^+ were quite similar. The voltage hysteresis between charge and discharge was over 200 mV, orders of magnitude larger than the ~ 10 mV hysteresis observed for similar current densities in aqueous cells. Neither the coulombic efficiency nor the cycle life of CuHCF in organic cells was impressive. Rapid fading of the specific capacity occurred in only 20 cycles, and the efficiency was only about 95%. It is possible that the CuHCF structure is less stable to electrochemical cycling in anhydrous conditions.

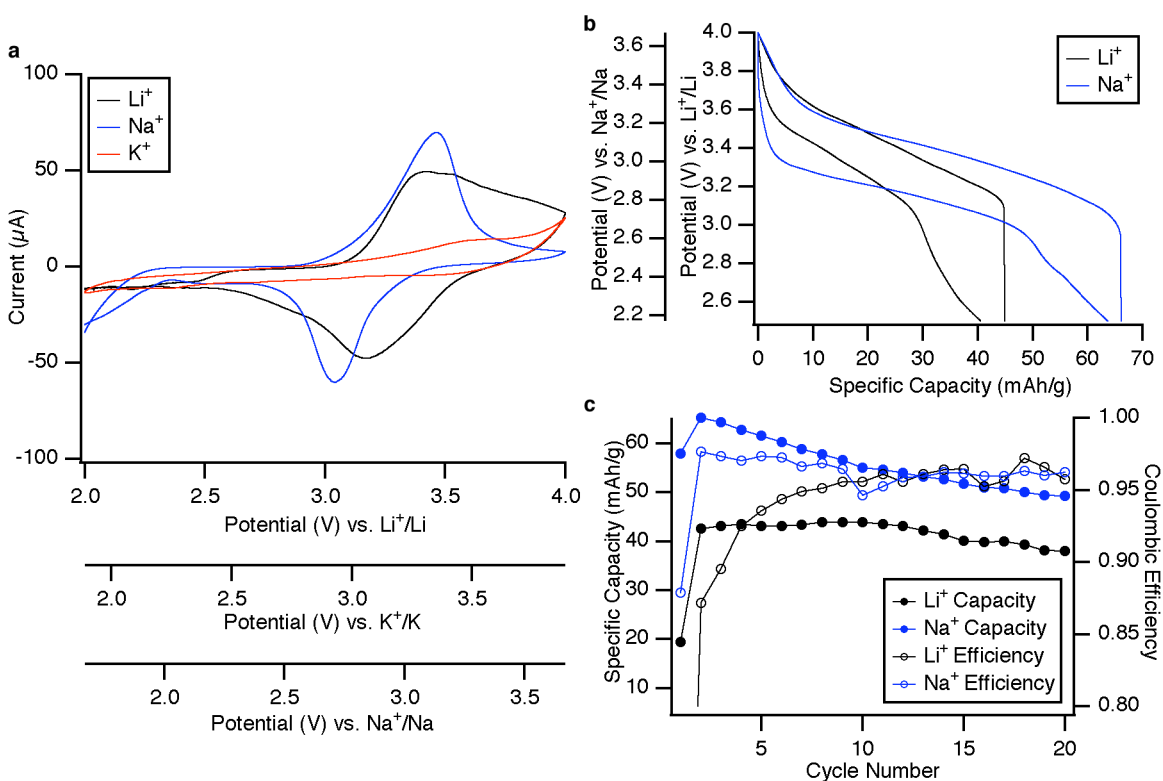


Figure 44: (a) Cyclic voltammetry of CuHCF at 1 mV/s in organic Li^+ , Na^+ , and K^+ cells. (b) Galvanostatic cycling of CuHCF in organic Li^+ and Na^+ at a C/6 rate. (c) The specific capacity and coulombic efficiency of CuHCF during galvanostatic cycling in organic cells at a C/6 rate.

Further characterization of Prussian Blue analogues in organic cells was not performed, as these preliminary results showed much worse performance than that observed in aqueous cells. In addition, the relatively low specific capacity of these materials makes them rather impractical for high voltage cells, the purpose of which is to provide as much energy as possible. Should the recent interest of the battery research community in organic electrolyte sodium ion batteries continue to grow, future study of Prussian Blue analogues in that type of cells may become more common.

Chapter 16: Summary and Final Comments on Prussian Blue Analogues

In this work, the physical and electrochemical properties of two Prussian Blue analogues, CuHCF and NiHCF, were studied in detail. It was found that they have extraordinary electrochemical performance, and when used as battery electrodes, have longer cycle life, higher rate capability, and higher energy efficiency than any commercialized battery electrode materials. Their synthesis from inexpensive, earth-abundant precursors is fast and scalable, and they operate in nonflammable, inexpensive aqueous electrolytes.

It is worthwhile to also consider the negative aspects of the use of these materials in batteries. First, they cannot be plausibly used to power portable electronic devices, as their specific capacities are low, and they operate in low voltage, aqueous cells. This results in both low specific energy and energy density. Second, it is unclear if their long cycle life can be maintained at more neutral pH values. It is challenging to avoid corrosion for long periods of time in acidic electrolytes. The use of carbon current collectors helps to alleviate this problem. Development of an anode suitable for use with the CuHCF and NiHCF cathodes may require less acidic electrolytes than those explored thus far.

Third, a major caveat that was largely unaddressed throughout the discussion of the performance of CuHCF and NiHCF is the trace solubility of these materials. In effect, they are ionic solids comprised of a $\text{Fe}(\text{CN})_6^{3-}$ anion and either Cu^{2+} or Ni^{2+} cations. Their synthesis in aqueous solution was successful because their components were supersaturated, but at all times, they are in equilibrium with a small amount of dissolved hexacyanoferrate and metal cations. Prussian Blue analogues are known to be less soluble in acids, and for this reason, mildly acidic electrolytes were used during electrochemical tests. In addition, the long cycle lives reported for half-cells were possible in part because of the large counter electrodes that were present. As they made up most of the mass of CuHCF or NiHCF in the cell, their presence allowed the electrolyte to reach saturation of $\text{Fe}(\text{CN})_6^{3-}$, Cu^{2+} , or Ni^{2+} without substantial dissolution of the working electrodes. The full cells discussed in Chapter 3.14 did not contain excess CuHCF and were nevertheless stable for over 1,000 cycles at a 10C rate. However, a method for stabilizing CuHCF against any dissolution must be developed before these devices can be successfully commercialized.

It is also worthwhile to consider future research directions related to Prussian Blue analogues. Among these is the open question about how and why the electrochemical properties of Prussian Blue analogues change depending on what species is intercalated. For instance, why is NiHCF stable for thousands of cycles of Na^+ intercalation, but cannot withstand cycling of Li^+ , even though the hydrated radii of both ions are much larger than the size of the channels between the A sites? Moreover, why is NiHCF stable during Na^+ cycling, but CuHCF is not? Some preliminary evidence of reversible insertion of Group II divalent cations also exists, and their hydrated radii are even larger. The behavior of Prussian Blue analogue electrodes cannot be fully understood until the fundamental question of how the different insertion ions move through the structure is answered.

Despite some performance limitations, the use of Prussian Blue analogues as battery electrodes is a rich, nascent field. Many fundamental scientific and engineering questions remain unaddressed, but their study will help enable the use of these materials in real batteries.

A number of open questions relating to the implementation of Prussian Blue analogues in real batteries must also be addressed. The possibility of changes in morphology or crystallinity during production of kilograms or metric tonnes of these materials, rather than just grams, is unknown. Likewise, the parameters of the co-precipitation method have not been optimized, either. And questions of electrode mass loading and composition, and cell geometry remain unanswered.

It is to be expected that the very positive results of the work presented in this dissertation will lead to further research on this family of interesting electrode materials.

References:

1. *EPRI-DOE Handbook of Energy Storage for Transmission and Distribution Applications*. EPRI, Palo Alto, CA, and the U.S. Department of Energy, Washington, DC: 2003. 1001834.
2. *Wind Power Integration: Smoothing Short-term Power Fluctuations*. EPRI, Palo Alto, CA: 2005. 1008852.
3. *Market Driven Distributed Energy Storage Requirements for Load Management Applications*. EPRI, Palo Alto, CA: 2007. 1014668.
4. Eyer, J. *Electric Utility Transmission and Distribution Upgrade Deferral Benefits from Modular Electricity Storage*. Sandia National Laboratories, Albuquerque, NM, and Livermore, CA: 2009. SAND2009-4070.
5. *2009 Integrated Energy Policy Report*, Final Commission Report. California Energy Commission, Sacramento, CA: 2009. CEC-100-2009-003-CMF.
6. *Electricity Energy Storage Technology Options*. EPRI, Palo Alto, CA: 2010. 1020676.
7. Eyer, J. *Energy Storage for the Electricity Grid: Benefits and Market Potential Assessment Guide*. Sandia National Laboratories, Albuquerque, NM, and Livermore, CA: 2010. SAND2010-0815.
8. *Functional Requirements for Electric Energy Storage Applications on the Power System Grid*. EPRI, Palo Alto, CA: 2011. 1021936.
9. *Benefit Analysis of Energy Storage: Case Study with Sacramento Municipal Utility District*. EPRI, Palo Alto, CA: 2011. 1023591.
10. Abele, A., et al. *2020 Strategic Analysis of Energy Storage in California*. California Energy Commission, Sacramento, CA: 2011. CEC-500-2011-047.
11. Loose, V. W. *Quantifying the Value of Hydropower in the Electric Grid: Role of Hydropower in Existing Markets*. Sandia National Laboratories, Albuquerque, NM, and Livermore, CA: 2011. SAND2011-1009.
12. *Impacts of Wind Generation Integration*. EPRI, Palo Alto, CA: 2011. 1023166.
13. LaCommare, K. H., and Eto, J. H. *Understanding the Cost of Power Interruptions to U.S. Electricity Consumers*. Lawrence Berkeley National Laboratory, Berkeley, CA, and the U.S. Department of Energy, Washington, DC: 2004. LBNL-55718.
14. Yang, Z., Zhang, J., Kintner-Meyer, M. C. W., Lu, X., Choi, D., Lemmon, J. P., Liu, J. Electrochemical Energy Storage for Green Grid. *Chem. Rev.*, **111**, 3577-3613 (2011).
15. Soloveichik, G. L. Battery Technologies for Large-Scale Energy Storage. In *Annu. Rev. Chem. Biomol. Eng. Vol. 2*; Prausnitz, J., Ed; Annual Reviews: Palo Alto, CA, 2011; 503-527.
16. Grid-Scale Rampable Intermittent Dispatchable Storage (GRIDS). Funding Opportunity Announcement, U.S. Department of Energy, Washington DC: 2010. DE-FOA-0000290.
17. J. P. Barton, and D. G. Infield. Energy Storage and Its Use With Intermittent Renewable Energy. *IEEE Trans. Energy Conversion*. 19, 441 (2004).
18. Conway, B. E. Transition from “Supercapacitor” to “Battery” Behavior in Electrochemical Energy Storage. *J. Electrochem. Soc.*, **138**, 1539 (1991).
19. “NGK Fire Incident and Response.” NGK Insulators, Ltd., October 28, 2011. <http://www.ngk.co.jp/english/news/2011/1028_01.html>
20. Balakrishnan, P. G., Ramesh, R., and Prem Kumar, T. Safety mechanisms in lithium-ion batteries. *J. Power Sources*, **155**, 401 (2006).
21. Brodd, R. Battery/Cell Manufacturing Cost Study. IMLB Conference Oral Presentation, June, 2010.
22. Gores, H. J., and Barthel, J. M. G. Nonaqueous electrolyte solutions: New materials for devices and processes based on recent applied research. *Pure & Appl. Chem.*, **67**, 919 (1995).
23. Kondo, K., et al. Conductivity and Solvation of Li⁺ Ions in LiPF₆ in Propylene Carbonate Solutions. *J. Phys. Chem. B*, **104**, 5040 (2000).
24. Ruffo, R., et al. Electrochemical Characterization of LiCoO₂ as rechargeable electrode in aqueous LiNO₃ electrolyte. *Solid State Ionics*, **192**, 289 (2011).
25. Li, W., Dahn, J. R., and Wainwright, D. S. Rechargeable Lithium Batteries with Aqueous Electrolytes. *Science*, **264**, 1115 (1994).

26. Chen, S., et al. Improved performances of mechanical-activated LiMn₂O₄/MWNTs cathode for aqueous rechargeable lithium batteries. *J. Appl. Electrochem.*, **39**, 1943 (2009).
27. Luo, J.-Y., Cui, W.-J., He, P., and Xia, Y.-Y. Raising the cycling stability of aqueous lithium-ion batteries by eliminating oxygen in the electrolyte. *Nature Chem.*, **2**, 760 (2010).
28. Athouël, L., et al. Variation of the MnO₂ Birnessite Structure upon Charge/Discharge in an Electrochemical Supercapacitor Electrode in Aqueous Na₂SO₄ Electrolyte. *J. Phys. Chem. C*, **112**, 7270 (2008).
29. Qu, Q. T., et al. A new cheap asymmetric aqueous supercapacitor: Activated carbon// NaMnO₂. *J. Power Sources*, **194**, 1222 (2009).
30. Whitacre, J. F., Tevar, A., and Sharma, S. Na₄Mn₉O₁₈ as a positive electrode material for an aqueous sodium-ion energy storage device. *Electrochem. Comm.*, **12**, 463 (2010).
31. Tevar, A. D., and Whitacre, J. F. Relating Synthesis Conditions and Electrochemical Performance for the Sodium Intercalation Compound Na₄Mn₉O₁₈ in Aqueous Electrolyte. *J. Electrochem. Soc.*, **157**, A870 (2010).
32. Chevrie, V. L., and Ceder, G. Challenges for Na-ion Negative Electrodes. *J. Electrochem. Soc.*, **158**, A1011 (2011).
33. Ong, S. P., et al. Voltage, stability, and diffusion barrier differences between sodium-ion and lithium-ion intercalation materials. *Energy & Envir. Sci.*, **1** (2011).
34. Park, S. I., Gocheva, I., Okada, S., and Yamaki, J. Electrochemical Properties of NaTi₂(PO₄)₃ Anode for Rechargeable Aqueous Sodium-Ion Batteries. *J. Electrochem. Soc.*, **158**, A1067 (2011).
35. Neff, V. D. Electrochemical Oxidation and Reduction of Thin Films of Prussian Blue. *J. Electrochem. Soc.*, **125**, 886 (1978).
36. Messina, R., Perichon, J., and Broussely, M. Mécanismes de la réduction électrochimique en milieu non aqueux de matériaux cathodiques utilisés dans les piles au lithium. IV. Réduction d'électrodes membranaires d'hexacyanoferrates (II et III) d'argent dans le mélange carbonate de propylène-1,2-diméthoxyéthane. *J. Appl. Electrochem.*, **9**, 677 (1979).
37. Messina, R., and Perichon, J. Mécanisme de la réduction électrochimique en milieu non aqueux de matériaux cathodiques utilisés dans les piles au lithium. V. Utilisation des hexacyanoferrates de fer (II et III) comme matériaux cathodiques réversibles. *J. Appl. Electrochem.*, **10**, 655 (1980).
38. Neff, V. D. Some Performance Characteristics of a Prussian Blue Battery. *J. Electrochem. Soc.*, **132**, 1382 (1985).
39. Honda, K. and Hayashi, H. Prussian Blue Containing Nafion Composite Film as Rechargeable Battery. *J. Electrochem. Soc.*, **134**, 1339 (1987).
40. Grabner, E. W., and Kalwellis-Mohn, S. Hexacyanoferrate layers as electrodes for secondary cells. *J. Appl. Electrochem.*, **17**, 653 (1987).
41. Kaneko, M., and Okada, T. A secondary battery composed of multilayer Prussian Blue and its reaction characteristics. *J. Electroanal. Chem.*, **255**, 45 (1988).
42. Kalwellis-Mohn, S., and Grabner, E. W. A Secondary Cell Based on Thin Film Layers of Zeolite-Like Nickel Hexacyanometallates. *Electrochim. Acta.*, **34**, 1265 (1989).
43. Jayalakshmi, M., and Scholz, F. Charge-discharge characteristics of a solid-state Prussian blue secondary cell. *J. Power Sources*, **87**, 212 (2000).
44. Jayalakshmi, M., and Sholz, F. Performance characteristics of zinc hexacyanoferrate/Prussian blue and copper hexacyanoferrate/Prussian blue solid state secondary cells. *J. Power Sources*, **91**, 217 (2000).
45. Tung, T.-S., Chen, L.-C., and Ho, K.-C. An indium hexacyanoferrate-tungsten oxide electrochromic battery with a hybrid K⁺/H⁺-conducting polymer electrolyte. *Solid State Ionics*, **165**, 257 (2003).
46. Okubo, M., et al. Switching Redox-Active Sites by Valence Tautomerism in Prussian Blue Analogues A_xMn_y[Fe(CN)₆]_nH₂O (A:K, Rb): Robust Frameworks for Reversible Li Storage. *J. Phys. Chem. Lett.*, **1**, 2063 (2010).
47. Fergus, J. W. Recent developments in cathode materials for lithium ion batteries. *J. Power Sources*, **195**, 939 (2010).
48. Li, W., McKinnon, W. R., and Dahn, J. R. Lithium Intercalation from Aqueous Solutions. *J. Electrochem Soc.*, **141**, 2310 (1994).
49. Zhang, M., and Dahn, J. R. Electrochemical Lithium Intercalation of VO₂(B) in Aqueous Electrolytes. *J. Electrochem. Soc.*, **143**, 2730 (1996).

50. Wang, G., et al. An Aqueous Rechargeable Lithium Battery with Good Cycling Performance. *Angew. Chem. Int. Ed.*, **46**, 295 (2007).
51. Wang, G. J., et al. Characteristics of an aqueous rechargeable lithium battery (ARLB). *Electrochim. Acta*, **52**, 4911 (2007).
52. Wang, H. et al. Electrochemical properties of TiP_2O_7 and $\text{LiTi}_2(\text{PO}_4)_3$ as anode material for lithium ion battery with aqueous solution electrolyte. *Electrochim. Acta*, **52**, 3280 (2007).
53. Luo, J.-Y., and Xia, Y.-Y. Aqueous Lithium-ion Battery $\text{LiTi}_2(\text{PO}_4)_3/\text{LiMn}_2\text{O}_4$ with High Power and Energy Densities as well as Superior Cycling Stability. *Adv. Func. Mat.*, **17**, 3877 (2007).
54. Liu, X.-H., et al. Electrochemical properties of rechargeable aqueous lithium ion batteries with an olivine-type cathode and a Nasicon-type anode. *J. Power Sources*, **189**, 706 (2009).
55. Wang, G. X., et al. Secondary aqueous lithium-ion batteries with spinel anodes and cathodes. *J. Power Sources*, **74**, 198 (1998).
56. Wang, G. J., et al. An aqueous rechargeable lithium battery based on doping and intercalation mechanisms. *J. Solid State Electrochem.*, **14**, 865 (2010).
57. Ruffo, R., Wessells, C., Huggins, R. A., and Cui, Y. Electrochemical behavior of LiCoO_2 as aqueous lithium-ion battery electrodes. *Electrochem. Comm.*, **11**, 247 (2009).
58. Mermilliod, N., and Tanguy, J. A Study of Chemically Synthesized Polypyrrole as Electrode Material for Battery Applications. *J. Electrochem. Soc.*, **133**, 1073 (1986).
59. Osaka, T., Naoi, K., and Ogano, S. Effect of Polymerization Anion on Electrochemical Properties of Polypyrrole and on $\text{Li}/\text{LiClO}_4/\text{Polypyrrole}$ Battery Performance. *J. Electrochem. Soc.*, **135**, 1071 (1988).
60. Manjunatha, H., Suresh, G. S., and Venkatesha, T. V. Electrode materials for aqueous rechargeable lithium batteries. *J. Solid State Electrochem.*, **15**, 431 (2011).
61. Bohnke, O., and Robert, G. Electrochemical lithium incorporation in WO_3 and MoO_3 thin films. *Solid State Ionics*, **6**, 115 (1982).
62. Granqvist, C. G. *Handbook of inorganic electrochromic materials*. Elsevier, New York: 1995.
63. Padhi, A. K., et al. Effect of Structure on the $\text{Fe}^{3+}/\text{Fe}^{2+}$ Redox Couple in Iron Phosphates. *J. Electrochem. Soc.*, **144**, 1609 (1997).
64. Shannon, R. D., Revised Effective Ionic Radii and Systematic Studies of Interatomic Distances in Halides and Chalcogenides. *Acta Cryst.*, **A32**, 751 (1976).
65. Tsuji, M., Komarneni, S., Tamaura, Y., and Abe, M. Cation Exchange Properties of a Layered Manganic Acid. *Mat. Res. Bull.*, **27**, 741 (1992).
66. Feng, Q., Kanoh, H., Miyai, Y., and Ooi, K. Hydrothermal Synthesis of Lithium and Sodium Manganese Oxides and Their Metal Ion Extraction/Insertion Reactions. *Chem. Mater.*, **7**, 1226 (1995).
67. Jayalakshmi, M., Mohan Rao, M., and Scholz, F. Electrochemical Behavior of Solid Lithium Manganate (LiMn_2O_4) in Aqueous Neutral Electrolyte Solutions. *Langmuir*, **19**, 8403 (2003).
68. Itaya, K., Ataka, T., and Toshima, S. Spectroelectrochemistry and Electrochemical Preparation Method of Prussian Blue Modified Electrodes. *J. Am. Chem. Soc.*, **104**, 4767 (1982).
69. Chen, S.-M., Preparation, characterization, and electrocatalytic oxidation properties of iron, cobalt, nickel, and indium hexacyanoferrate. *J. Electroanal. Chem.*, **521**, 29 (2002).
70. Oi, T. Electrochromic Materials. *Ann. Rev. Mater. Sci.*, **16**, 185 (1986).
71. Bard, A. J. *Electrochemical Methods: Fundamentals and Applications*. New York: Wiley, 2001.
72. Wessells, C., Ruffo, R., Huggins, R. A., and Cui, Y. Investigations of the Electrochemical stability of Aqueous Electrolytes for Lithium Battery Applications. *Electrochem. Solid State Lett.*, **13**, A59 (2010).
73. Mizushima, K., Jones, P. C., Wiseman, P. J., and Goodenough, J. B. Li_xCoO_2 ($0 < x \leq 1$): A New Cathode Material For Batteries Of High Energy Density. *Mat. Res. Bull.*, **15**, 783 (1980).
74. Orman, H. J., and Wiseman, P. J. Cobalt(III) Lithium Oxide, CoLiO_2 : Structure Refinement by Powder Neutron Diffraction. *Acta Cryst.*, **C40**, 12 (1984).
75. Huggins, R. A. *Advanced Batteries: Materials Science Aspects*. New York: Springer, 2009.
76. Padhi, A. K., Nanjundaswamy, K. S., and Goodenough, J. B. Phospho-olivines as a Positive-Electrode Materials for Rechargeable Lithium Batteries. *J. Electrochem. Soc.*, **144**, 1188.
77. Laffont, L., et al. Study of the $\text{LiFePO}_4/\text{FePO}_4$ Two-Phase System by High-Resolution Electron Energy Loss Spectroscopy. *Chem. Mat.*, **18**, 5520 (2006).

78. Dreyer, W., et al. The thermodynamic origin of hysteresis in insertion batteries. *Nature Mat.*, **9**, 448 (2010).
79. Li, G., Azuma, H., and Tohda, M. LiMnPO₄ as the Cathode for Lithium Batteries. *Electrochem. Solid State Lett.*, **5**, A135 (2002).
80. Colbow, K. M., Dahn, J. R., and Haering, R. R. Structure and Electrochemistry of the Spinel Oxides LiTi₂O₄ and Li_{4/3}Ti_{5/3}O₄. *J. Power Sources*, **26**, 397 (1989).
81. Hong, H. Y-P. Crystal Structures and Crystal Symmetry in the System Na_{1+x}Zr₂Si_xP_{3-x}O₁₂. *Mat. Res. Bull.*, **11**, 173 (1976).
82. Goodenough, J. B., Hong, H. Y-P., and Kafalas, J. A. Fast Na⁺ - Ion Transport in Skeleton Structures. *Mat. Res. Bull.*, **11**, 203 (1976).
83. Nanjundaswamy, K. S., et al. Synthesis, redox potential evaluation and electrochemical characteristics of NASICON-related-3D framework compounds. *Solid State Ionics*, **92**, 1 (1996).
84. Yaroslavtsev, A. B., and Stenina, I. A. Complex Phosphates with the NASICON Structure (M_xA₂(PO₄)₃). *Russ. J. Inorg. Chem.*, **51**, S97 (2006).
85. Delmas, C., and Nadiri, A. The Nasicon-Type Titanium Phosphates ATi₂(PO₄)₃ (A=Li, Na) As Electrode Materials. *Solid State Ionics*, **28-30**, 419 (1988).
86. Nuspl, G., et al. Lithium ion migration pathways in LiTi₂(PO₄)₃ and related materials. *J. Appl. Phys.*, **86**, 5484 (1999).
87. Kobayashi, Y., et al. Densification of LiTi₂(PO₄)₃-based solid electrolytes by spark-plasma sintering. *J. Power Sources*, **81-82**, 853 (1999).
88. Chang, C.-M., Lee, Y. I., and Hong, S.-H. Spark Plasma Sintering of LiTi₂(PO₄)₃-Based Solid Electrolytes. *J. Am. Ceram. Soc.*, **88**, 1803 (2005).
89. Porcher, W., et al. Is LiFePO₄ Stable in Water? *Electrochem. Solid-State Lett.*, **11**, A4 (2008).
90. Mariappan, C. R., et al. Synthesis of nanostructured LiTi₂(PO₄)₃ powder by a Pechini-type polymerizable complex method. *J. Solid State Chem.*, **179**, 450 (2006).
91. Wessells, C., et al. Synthesis and Electrochemical Performance of a Lithium Titanium Phosphate Anode for Aqueous Lithium-Ion Batteries. *J. Electrochem. Soc.*, **158**, A352 (2011).
92. Wessells, C., Huggins, R. A., and Cui, Y. Recent results on aqueous electrolyte cells. *J. Power Sources*, **196**, 2884 (2011).
93. Itaya, K., et al. Prussian-blue-modified electrodes: An application for a stable electrochromic display service. *J. Appl. Phys.*, **53**, 804 (1982).
94. Stilwell, D. E., Park, K. H., and Miles, M. H. Electrochemical studies of the factors influencing the cycle stability of Prussian Blue films. *J. Appl. Electrochem.*, **22**, 325 (1992).
95. Stahl, G. E. *Experimenta, Observationes, Animadversiones CCC Numero, Chymicae et Physicae*. Berlin, 1731, pp. 281-283.
96. Bartoll, J., et al. The Early Use of Prussian Blue in Paintings. 9th International Conference on NDT of Art. Jerusalem, Israel, May 25-30, 2008.
97. Rafalska-Lasocha, A., and Podulka, K. XRPD investigations of "Prussian Blue" artists' pigment. *Powder Diffraction*, **26**, 39 (2011).
98. Macquer, P.-J. Examen chymique de bleu de Prusse. *Mémoires de Mathématique et de Physique Tirés des Registres de l'Académie Royale des Sciences, De l'Anné M. DCCLII*, Paris, 1756, pp. 60-77.
99. Skraup, Z. H. Zur Kenntniss der Eisencyanoverbindungen. *J. Liebigs Annalen der Chemie*, **189**, 368 (1877).
100. Watts, H. *A Dictionary of Chemistry and the Allied Branches of Other Sciences, Third Supplement, Part I*, London: Longmans, Green, and Co., 1879, pp. 610-616.
101. Robin, M. B. The Color and Electronic Configurations of Prussian Blue. *Inorg. Chem.*, **1m** 337 (1962).
102. Robin, M. B., and Day, P. Mixed Valence Chemistry—A Survey and Classification. *Adv. Inorg. Chem. Radiochem.*, **10**, 247 (1967).
103. Fluck, E., Kerler, W., and Neuwirth, W. The Mössbauer Effect and its Significance in Chemistry. *Angew. Chemie. Int. Ed.*, **2**, 277 (1963).
104. Holtzman, H. Alkali Resistance of the Iron Blues. *Indust. Engr. Chem.*, **37**, 8556 (1945).
105. Kegglin, J. F., and Miles, F. D. Structures and Formulae of the Prussian Blues and Related Compounds. *Nature*, **137**, 577 (1936).
106. Rigamonti, R. Structure of ferrocyanides. *Gazzetta Chimica Italiana*, **68**, 803 (1938).

107. Weiser, H. B., Milligan, W. O., and Bates, J. B. X-ray Diffraction Studies on Heavy-Metal Iron-Cyanides. *J. Phys. Chem.*, **46**, 99 (1942).
108. Freise, F. Zur Permselectivität und Semipermeabilität der Kupferferrocyanidmembran. *Z. physic. Chem.*, **15**, 48 (1958).
109. Madshus, K., and Stromme, A. Increased Excretion of ¹³⁷Cs in Humans by Prussian Blue. *Zeit. Natur. Chemie Biochemie BioPhys. Bio. Verwandten Gebiete*, **B 23**, 391 (1968).
110. Bozorgza, A. Decorporation of Radiocesium by means of Different Hexacyanoferrates(II). *Strahlentherapie*, **142**, 734 (1971).
111. Jain, A. K., Singh, R. P., and Bala, C. Ion-Exchange Behavior of Copper Ferricyanide. *J. Radioanal. Chem.*, **75**, 85 (1982).
112. Tani, Y., Eun, H., and Umezawa, Y. A cation selective electrode based on copper(II) and nickel(II) hexacyanoferrates: dual response mechanisms, selective uptake or adsorption of analyte cations. *Electrochim. Acta*, **43**, 3431 (1998).
113. Zadronecki, M., et al. High Affinity of Thallium Ions to Copper Hexacyanoferrate Films. *J. Electrochem. Soc.*, **148**, E348 (2001).
114. Korshunov, I. A., and Lebedeva, Z. M. Isotopic Exchange of Iron Atoms in Prussian Blue. *J. Inorg. Chem. USSR*, **1**, 227 (1956).
115. Volkhin, V. V., and Kolesova, S. A. Molecular Sorption of Rubidium Nitrite by Nickel Hexacyanoferrate(II). *Russ. J. Phys. Chem.*, **43**, 1025 (1969).
116. Kolesova, S. A., Zatonka, T. P., and Volkhin, V. V. Separating Salts of Alkaline Elements Through Chromatography in Ferrocyanides. *Zhurnal Prikladnoi Khimii*, **44**, 1415 (1971).
117. Barbezat, S., and Trillat, J.-J. X-ray study of the thermal decomposition of Prussian blue. *J. Res. Centre Nat. Res. Sci*, **4**, 184 (1952).
118. Kohn, M. New Observations on the Solubility of Prussian Blue. *Anal. Chimica Acta*, **11**, 18 (1954).
119. Nasiruddin, K., Malik, W. U., and Bhattacharya, A. K. Studies on the Sol-Gel Transformation of the Ferrocyanides and Ferricyanides of Some Metals. 1. Gel Formation of Prussian and Turnbull Blues. *J. Phys. Chem.*, **59**, 488 (1955).
120. Ferrari, A., Tani, M. E., and Morisi, E. The crystal structure of iridiohexacyanides of divalent cations. *Acta Cryst.*, **14**, 695 (1961).
121. Ferrari, A., Tani, M. E., and Morisi, E. The crystal structure of hexacyanochromate(III) of divalent cations. *Acta Cryst.*, **15**, 90 (1962).
122. Ferrari, A., Tani, M. E., and Morisi, E. The crystal structure of hexacyanomanganates(III) of bivalent cations. *Acta Cryst.*, **17**, 311 (1964).
123. Champion, A. R., and Drickame, H. G. Effect of Pressure on Moss Bauer Resonance in Potassium Ferrocyanide, Potassium Ferricyanide, and Insoluble Prussian Blue. *J. Chem. Phys.*, **47**, 2591 (1967).
124. Ito, A., Suenaga, M., and Ono, K. Moss Bauer Study of Soluble Prussian Blue, Insoluble Prussian Blue, and Turnbull's Blue. *J. Chem. Phys.*, **48**, 3597 (1968).
125. Brown, D. B., Shriver, D. F., and Schwartz, L. H. Solid-State Reactions of Iron(II) Hexacyanochromate(III). *Inorg. Chem.*, **7**, 77 (1968).
126. Brown, D. B., and Shriver, D. F. Structures and Solid-State Reactions of Prussian Blue Analogues Containing Chromium, Manganese, Iron, and Cobalt. *Inorg. Chem.*, **8**, 37 (1969).
127. Shriver, D. F., and Brown, D. B. The Environment of Interstitial Ions in a Prussian Blue Analog, Co₃[Co(CN)₆]₂. *Inorg. Chem.*, **8**, 42 (1969).
128. Bellomo, A. Formation of Copper(II), Zinc(II), Silver(I), and Lead(II) Ferrocyanides. *Talanta*, **17**, 1109 (1970).
129. Wilde, R. E., Ghosh, S. N., and Marshall, B. J. The Prussian Blues. *Inorg. Chem.*, **9**, 2512 (1970).
130. Ludi, A., Güdel, H. U., and Rugg, M. Structural Chemistry of Prussian Blue Analogues – A Single-Crystal Study of Manganese(II) Hexacyanocobaltate(III), Mn₃[Co(CN)₆]₂·xH₂O. *Inorg. Chem.*, **9**, 2224 (1970).
131. Wertheim, G. K., and Rosencwa, A. Characterization of Inequivalent Iron Sites in Prussian Blue by Photoelectron Spectroscopy. *J. Chem. Phys.*, **54**, 3235 (1971).
132. Armand, M. B., Whittingham, M. S., and Huggins, R. A. The Iron Cyanide Bronzes. *Mat. Res. Bull.*, **7**, 101 (1972).

133. Ludi, A., and Güdel, H. U. Structural Chemistry of Polynuclear Transition Metal Cyanides. *Structure and Bonding*, **14**, 1 (1973).
134. Inoue, H., and Yanagisawa, S. Bonding nature and semiconductivity of Prussian blue and related compounds. *J. Inorg. Nucl. Chem.*, **36**, 1409 (1974).
135. Hara, Y., and Minomura, S. Changes of the electronic states of a mixed-valence compound at high pressures-insoluble Prussian blue, $\text{Fe}_4[\text{Fe}(\text{CN})_6]_3$. *J. Chem. Phys.*, **61**, 5339 (1974).
136. Buser, H. J., Schqarzenbach, D., Petter, W., and Ludi, A. The Crystal Structure of Prussian Blue: $\text{Fe}_4[\text{Fe}(\text{CN})_6]_3 \cdot x\text{H}_2\text{O}$. *Inorg. Chem.*, **16**, 2704 (1977).
137. Herren, F., Fischer, P., Ludi, A., and Halg, W. Neutron Diffraction Study of Prussian Blue, $\text{Fe}_4[\text{Fe}(\text{CN})_6]_3 \cdot x\text{H}_2\text{O}$. Location of Water Molecules and Long-Range Magnetic Order. *Inorg. Chem.*, **19**, 956 (1980).
138. Rajan, K. P., and Neff, V. D. Electrochromism in the Mixed-Valence Hexacyanides. 2. Kinetics of the Reduction of Ruthenium Purple and Prussian Blue. *J. Phys. Chem.*, **86**, 4361 (1982).
139. Bocarsly, A. B., and Sinha, S. Effects of Surface Structure on Electrode Charge Transfer Properties: Induction of Ion Selectivity at the Chemically Derivatized Interface. *J. Electroanal. Chem.*, **140**, 167 (1982).
140. Siperko, L. M., and Kuwana, T. Electrochemical and Spectroscopic Studies of Metal Hexacyanometalate Films. 1. Cupric Hexacyanoferrate. *J. Electrochem. Soc.*, **130**, 396 (1983).
141. Sinha, S., Humphrey, B. D., and Bocarsly, A. B. Reaction of Nickel Electrode Surfaces with Anionic Metal-Cyanide Complexes: Formation of Precipitated Surfaces. *Inorg. Chem.*, **23**, 203 (1984).
142. Humphrey, B. D., Sinha, S., and Bocarsly, A. B. Diffuse Reflectance Spectroelectrochemistry as a Probe of the Chemically Derivatized Electrode Interface. The Derivatized Nickel Electrode. *J. Phys. Chem.*, **88**, 736 (1984).
143. Itaya, K., Uchida, I., and Neff, V. D. Electrochemistry of Polynuclear Transition Metal Cyanides: Prussian Blue and Its Analogues. *Acc. Chem. Res.*, **19**, 162 (1986).
144. Siperko, L. M., and Kuwana, T., Electrochemical and Spectroscopic Studies of Metal Hexacyanometalate Films-III. Equilibrium and Kinetic Studies of Cupric Hexacyanoferrate. *Electrochim. Acta.*, **32**, 765 (1987).
145. McCargar, J. W., and Neff, V. D. Thermodynamics of Mixed-Valence Intercalation Reactions: The Electrochemical Reduction of Prussian Blue. *J. Phys. Chem.*, **92**, 3598 (1988).
146. Habib, M. A., Maheswari, S. P., and Carpenter, M. K. A tungsten-trioxide/Prussian blue complementary electrochromic cell with a polymer electrolyte. *J. Appl. Electrochem.*, **21**, 203 (1991).
147. Duek, E. A. R., De Paoli, M.-A., and Mastragostino, M. An Electrochromic Device Based on Polyaniline and Prussian Blue. *Adv. Mat.*, **4**, 287 (1992).
148. Duek, E. A. R., De Paoli, M.-A., and Mastragostino, M. A Solid-State Electrochromic Device based on Polyaniline, Prussian Blue and an Elastomeric Electrolyte. *Adv. Mat.*, **5**, 650 (1993).
149. Ho, K.-C. Cycling and at-rest stabilities of a complementary electrochromic device based on tungsten oxide and Prussian blue thin films. *Electrochim. Acta*, **44**, 3227 (1999).
150. Wessells, C. D., Huggins, R. A., and Cui, Y. Copper hexacyanoferrate battery electrodes with long cycle life and high power. *Nature Comm.*, **2**, 550 (2011).
151. Wessells, C. D., Peddada, S. V., Huggins, R. A., and Cui, Y. Nickel Hexacyanoferrate Nanoparticle Electrodes For Aqueous Sodium and Potassium Ion Batteries. *Nano Lett.*, **11**, 5421 (2011).
152. Wessells, C. D., Peddada, S. V., McDowell, M. T., Huggins, R. A., and Cui, Y. The Effect of Insertion Species on Nanostructured Open Framework Hexacyanoferrate Battery Electrodes. *J. Electrochem. Soc.*, **159**, A98 (2012).
153. Wessells, C. D., McDowell, M. T., Peddada, S. V., Pasta, M., Huggins, R. A., and Cui, Y. Tunable Reaction Potentials in Open Framework Nanoparticle Battery Electrodes for Grid-Scale Energy Storage. *ACS Nano*, **6**, 1688 (2012).
154. Pasta, M., Wessells, C. D., Huggins, R. A., and Cui, Y. A High Rate, Long Cycle Life Aqueous Electrolyte Battery for Grid Scale Energy Storage. In press, 2012.
155. Sato, O. Electrochromism and electrochemical magnetism in Ni-Fe Prussian Blue. *J. Solid State Chem.*, **11**, 773 (2007).

156. Griffith, W. P. Cyanide Complexes of the Early Transition Metals (Groups IVa-VIIa). *Coord. Chem. Rev.*, **17**, 177 (1975).
157. Maer, Jr., K., Beasley, M. L., Collins, R. L., and Milligan, W. O. The Structure of Titanium-Iron Cyanide Complexes. *J. Am. Chem. Soc.*, **90**, 3201 (1968).
158. Shaojun, D., and Fengbin, L. Researches on Chemically Modified Electrodes Part XV. Preparation and Electrochromism of the Vanadium Hexacyanoferrate Film Modified Electrode. *J. Electroanal. Chem.*, **210**, 31 (1986).
159. Scholz, F., and Dostal, A. The Formal Potentials of Solid Metal Hexacyanometalates. *Angew. Chem. Int. Ed. Engl.*, **34**, 2685 (1995).
160. Joseph, J., Gomathi, H., and Rao, G. P. Modification of carbon electrodes with zinc hexacyanoferrate. *J. Electroanal. Chem.*, **431**, 231 (1997).
161. de Tacconi, N. R., and Rajeshwar, K. Metal Hexacyanoferrates: Electrosynthesis, in Situ Characterization, and Applications. *Chem. Mater.*, **15**, 3046 (2003).
162. Wu, P., and Cai, C. The solid state electrochemistry of samarium (III) hexacyanoferrate (II). *J. Solid State Electrochem.*, **8**, 538 (2004).
163. Razmi, H., and Heidari, H. Preparation, Electrochemistry, and Electrocatalytic Activity of Lead Pentacyanonitrosylferrate Film Immobilized on Carbon Ceramic Electrode. *Electroanalysis*, **20**, 2370 (2008).
164. Ayrault, S., Loos-Neskovic, C., Fedoroff, M., and Garnier, E. Copper Hexacyanoferrates: Preparation, Composition, and Structure. *Talanta*, **41**, 1435 (1994).
165. Ayrault, S., et al. Compositions and structures of copper hexacyanoferrates(II) and (III): experimental results. *Talanta*, **42**, 1581 (1995).
166. Reddy, S. J., Dostal, A., and Scholz, F. Solid state electrochemical studies of mixed nickel-iron hexacyanoferrates with the help of abrasive stripping voltammetry. *J. Electroanal. Chem.*, **403**, 209 (1996).
167. Zakharchuk, N. F., et al. Solid state electrochemistry, X-ray powder diffraction, magnetic susceptibility, electron spin resonance, Mössbauer and diffuse reflectance spectroscopy of mixed iron(III)-cadmium(II) hexacyanoferrates. *J. Solid State Electrochem.*, **3**, 264 (1999).
168. Kulesza, P. J., et al. Electrochemical preparation and characterization of electrodes modified with mixed hexacyanoferrates of nickel and palladium. *J. Electroanal. Chem.*, **487**, 57 (2000).
169. Widmann, A., et al. Structure, Insertion Electrochemistry, and Magnetic Properties of a New Type of Substitutional Solid Solutions of Copper, Nickel, and Iron Hexacyanoferrates/Hexacyanocobaltates. *Inorg. Chem.*, **41**, 5706 (2002).
170. Soria, D. B., Gentil, L. A., and Aymonino, P. J. Crystal structure and infrared and electronic spectra of some divalent first series transition metal pentacyanonitrosylmanganates (I). *J. Cryst. Spect. Res.*, **18**, 133 (1988).
171. Vertelman, E. J., et al. The Influence of Defects on the Electron-Transfer and Magnetic Properties of $\text{Rb}_x\text{Mn}[\text{Fe}(\text{CN})_6]_y \cdot z\text{H}_2\text{O}$. *Chem. Mater.*, **18**, 1951 (2006).
172. Bleuzen, A., et al. Thermally Induced Electron Transfer in a CsCoFe Prussian Blue Derivative: The Specific Role of the Alkali-Metal Ion. *Angew. Chem. Int. Ed.*, **43**, 3728 (2004).
173. Flambard, A., Köhler, F. H., and Lescouézec, R. Revisiting Prussian Blue Analogues with Solid-State MAS NMR Spectroscopy: Spin Density and Local Structure in $[\text{Cd}\{\text{Fe}(\text{CN})_6\}_2] \cdot 15\text{H}_2\text{O}$. *Angew. Chem. Int. Ed.*, **48**, 1673 (2009).
174. Kaye, S. S., and Long, J. R. The role of vacancies in the hydrogen storage properties of Prussian blue analogues. *Catalysis Today*, **120**, 311 (2007).
175. Itaya, K., Ataka, T., Toshima, S., and Shinohara, T. Electrochemistry of Prussian Blue. An in Situ Mössbauer Effect Measurement. *J. Phys. Chem.*, **86**, 2415 (1982).
176. Ikeshoji, T., and Iwasaki, T. In Situ X-ray Diffraction Measurement of a Prussian Blue Modified Electrode. *Inorg. Chem.*, **27**, 1123.
177. Dostal, A., Kauschka, G., Reddy, S. J., and Scholz, F. Lattice contractions and expansions accompanying the electrochemical conversions of Prussian blue and the reversible and irreversible insertion of rubidium and thallium ions. *J. Electroanal. Chem.*, **406**, 155 (1996).
178. Soto, M. B., and Scholz, F. The thermodynamics of the insertion electrochemistry of solid metal hexacyanometalates. *J. Electroanal. Chem.*, **521**, 183 (2002).
179. Jiang, M., Zhou, X., and Zhao, Z. Preparation and characterization of mixed-valent titanium hexacyanoferrate film modified glassy carbon electrode. *J. Electroanal. Chem.*, **292**, 289 (1990).

180. Roberts, L. Radiation Accident Grips Goiânia. *Science*, **238**, 1028 (1987).
181. *The Radiological Accident in Goiânia*. Vienna: International Atomic Energy Agency, 1988.
182. Klenze, R., Kanellakopoulos, B., Trageser, G., and Eysel, H. H. Manganese hexacyanomanganate: Magnetic interactions via cyanide in a mixed valence Prussian blue type compound. *J. Chem. Phys.*, **72**, 5819 (1980).
183. Entley, W. R., and Girolami, G. S. High-Temperature Molecular Magnets Based on Cyanovanadate Building Blocks; Spontaneous Magnetization at 230 K.
184. Buschmann, W. E., Ensling, J., Gütlich, P., and Miller, J. S. Electron Transfer, Linkage Isomerization, Bulk Magnetic Order, and Spin-Glass Behavior in the Iron Hexacyanomanganate Prussian Blue Analogue. *J. Chem. Euro.*, **5**, 3019 (1999).
185. Holmes, S. M., and Girolami, G. S. Sol-Gel Synthesis of $KV^{II}[Cr^{III}(CN)_6] \cdot 2H_2O$: A Crystalline Molecule-based Magnet with a Magnetic Ordering Temperature above 100° C. *J. Am. Chem. Soc.*, **121**, 5593 (1999).
186. Kaye, S. S., and Long, J. R. Hydrogen Storage in the Dehydrated Prussian Blue Analogues $M_3[Co(CN)_6]_2$ (M = Mn, Fe, Co, Ni, Cu, Zn). *J. Am. Chem. Soc.*, **127**, 6506 (2005).
187. Thallapally, P. K., et al. Prussian Blue Analogues for CO₂ and SO₂ Capture and Separation Applications. *Inorg. Chem.*, **49**, 4909 (2010).
188. Barsoukov, E., et al. Comparison of kinetic properties of LiCoO₂ and LiTi_{0.05}Mg_{0.05}Ni_{0.7}Co_{0.2}O₂ by impedance spectroscopy. *Solid State Ionics*, **161**, 19 (2003).
189. Schmidt, J. P., et al. Studies on LiFePO₄ as cathode material using impedance spectroscopy. *J. Power Sources*, **196**, 5342 (2011).
190. Ceder, G., and Kang, B. Response to “unsupported claims of ultrafast charging of Li-ion batteries.” *J. Power Sources*, **194**, 1024 (2009).
191. Lai, C., Dou, Y. Y., Li, X., and Gao, X. P. Improvement of the high rate capability of hierarchical structured Li₄Ti₅O₁₂ induced by the pseudocapacitive effect. *J. Power Sources*, **195**, 3676 (2010).
192. Yang, J., et al. Large-scale Synthesis of Berlin Green Fe[Fe(CN)₆] Microcubic Crystals. *Cryst. Growth. Des.*, **6**, 2438 (2006).
193. Pau, C. F., Berg, J. O., and McMillan, W. G. Application of Stokes’ Law to Ions in Aqueous Solution. *J. Phys. Chem.*, **94**, 2671 (1990).
194. Gaur, J. R. Ferrocyanide Complex of Titanium (III). *Z. Anorg. Allg. Chemie.*, **324**, 304 (1963).
195. Bennett, B. G., and Nicholls, D. The Complex Cyanides of Vanadium. *J. Chem. Soc. A.*, 1204 (1971).
196. Holt, D. G. L., et al. Facile Synthesis of Complexes of Vanadium(II) and the Crystal and Molecular Structures of Hexa-aquavanadium(II) Trifluoromethylsulphonate. *Inorg. Chim. Acta*, **169**, 201 (1990).
197. Nelson, et al. Solvent-Enhanced Magnetic Ordering Temperature for Mixed-Valent Chromium Hexacyanovanadate(II), $Cr^{II}_{0.5}Cr^{III}[V^{II}(CN)_6] \cdot zMeCN$, Magnetic Materials. *Inorg. Chem.*, **45**, 8922 (2006).
198. Heintz, E. A. Observations on Potassium Hexacyanotitanate (III). *Nature*, **197**, 690 (1963).
199. Entley, W. R., Treadway, C. R., Wilson, S. R., and Girolami, G. S. The Hexacyanotitanate Ion: Synthesis and Crystal Structure of $[NEt_4]_3[Ti^{III}(CN)_6] \cdot 4MeCN$. *J. Am. Chem. Soc.*, **119**, 6251 (1997).
200. Penneman, R. A., et al. An Infrared Study of Pentacyano-, Hexacyano-, and Chloropentacyanonickelate(II) in Aqueous Solution. *J. Chem. Soc.*, 2266 (1963).
201. Dostal, A., Schröder, U., and Scholz, F. Electrochemistry of Chromium(II) Hexacyanochromate(III) and Electrochemically Induced Isomerization of Solid Iron(II) Hexacyanochromate(III) Mechanically Immobilized on the Surface of a Graphite Electrode. *Inorg. Chem.*, **34**, 1711 (1995).
202. Eftekhari, A. A high-voltage solid-state secondary cell based on chromium hexacyanometallates. *J. Power Sources*, **117**, 249 (2003).
203. Eftekhari, A. Fabrication of all-solid-state thin-film secondary cells using hexacyanometalate-based electrode materials. *J. Power Sources*, **132**, 291 (2004).
204. Adamson, A. W., Welker, J. P., and Wright, W. B. Exchange Studies with Complex Ions. II. The Kinetics of the Exchange of Radiocyanide Ion with Potassium Hexacyanomanganate(III) in Aqueous Solution. *J. Am. Chem. Soc.*, **73**, 4786 (1951).

205. López-Cueto, G., and Ubide, C. Fast disproportionation of hexacyanomanganate(III) in acidic solution. Formation of hexacyanomanganate(IV) and kinetics of its decomposition. *Can. J. Chem.*, **64**, 2301 (1986).
206. Reguera, E., Bertrán, J. F., and Nuñez, L. Study of the Linkage Isomerization Process in Hexacyanometallates. *Polyhedron*, **13**, 1619 (1994).
207. Bagkar, N., et al. Crystalline thin films of transition metal hexacyanochromates grown under Langmuir monolayer. *Thin Solid Films*, **513**, 325 (2006).

